Application of *Ab-initio* Calculations to Modeling of Nanoscale Diffusion and Activation in Silicon

Milan Diebel

A dissertation submitted in partial fulfillment of
the requirements for the degree of

Doctor of Philosophy

University of Washington

2004

Program Authorized to Offer Degree: Physics

University of Washington

Graduate School

This is to certify that I have examined this copy of a doctoral dissertation by

Milan Diebel

and have found that it is complete and satisfactory in all respects,
and that any and all revisions required by the final
examining committee have been made.

Chair of Supervisory Committee:

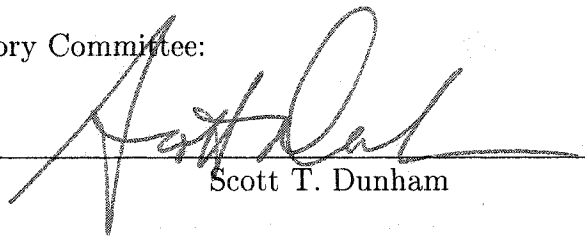

Scott T. Dunham

Reading Committee:

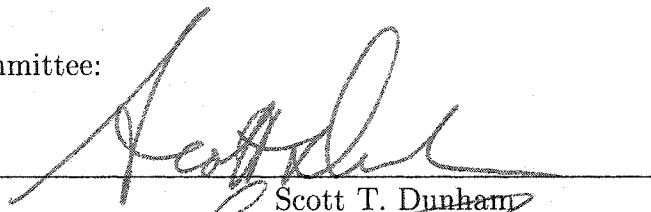

Scott T. Dunham

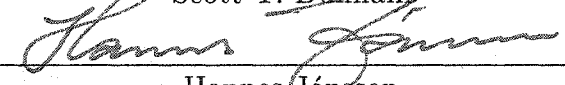

Hannes Jónsson

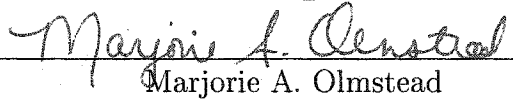

Marjorie A. Olmstead

Date: 8/19/04

In presenting this dissertation in partial fulfillment of the requirements for the doctoral degree at the University of Washington, I agree that the Library shall make its copies freely available for inspection. I further agree that extensive copying of this dissertation is allowable only for scholarly purposes, consistent with "fair use" as prescribed in the U.S. Copyright Law. Requests for copying or reproduction of this dissertation may be referred to Bell and Howell Information and Learning, 300 North Zeeb Road, Ann Arbor, MI 48106-1346, or to the author.

Signature 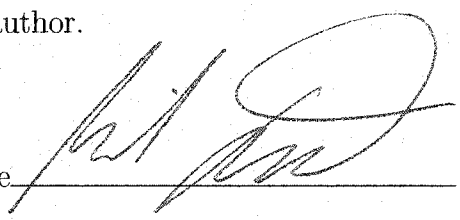

Date 08/19/04

University of Washington

Abstract

Application of *Ab-initio* Calculations to Modeling of Nanoscale Diffusion and Activation in Silicon

by Milan Diebel

Chair of Supervisory Committee:

Professor Scott T. Dunham
Electrical Engineering

As ULSI devices enter the nanoscale, ultra-shallow and highly electrically active junctions become necessary. New materials and 3D device structures as well as new process technologies are under exploration to meet the requirements of future devices. A detailed understanding of the atomistic mechanisms of point-defect/dopant interactions which govern diffusion and activation behavior is required to overcome the challenges in building these devices. This dissertation describes how *ab-initio* calculations can be used to develop physical models of diffusion and activation in silicon. A hierarchy of approaches (*ab-initio*, kinetic lattice Monte Carlo, continuum) is used to bridge the gaps in time scale and system size between atomistic calculations and nanoscale devices. This modeling approach is demonstrated by investigating two very different challenges in process technology: F co-implantation and stress effects on dopant diffusion/activation.

In the first application, *ab-initio* calculations are used to understand anomalous F diffusion behavior. A set of strongly bound fluorine vacancy complexes (F_nV_m) were found. The decoration of vacancies/dangling silicon bonds by fluorine leads to fluo-

rine accumulating in vacancy rich regions, which explains the fluorine redistribution behavior reported experimentally. The revealed interactions of F with point-defects explain the benefits of F co-implantation for B and P activation and diffusion. Based on the insight gained, a simplified F diffusion model at the continuum level (50-100 nm scale) is extracted that accounts for co-implantation effects on B and P for various implant energies and doses.

The second application addresses the effect of stress on point-defect/dopant equilibrium concentration, diffusion, and activation. A methodology is developed to extract detailed stress effects from *ab-initio* calculations. The approach is used to extract induced strains and elasticity tensors for various defects and impurities in order to predict the impact of arbitrary stress tensors (i.e., not just hydrostatic case). The results from first-principles calculations are used in lattice Monte Carlo simulations to quantify stress-driven anisotropies in I and B diffusion. The result is a prediction of strongly anisotropic diffusion of B (as well as I) under biaxial strain. Following the same methodology, a stress dependent B solubility model was developed which predicts large enhancements of B solubility under compressive stress conditions.

TABLE OF CONTENTS

LIST OF FIGURES

LIST OF TABLES

GLOSSARY

BIC: Boron interstitial cluster.

BZ: Brillouin zone.

CMOS: Complementary metal oxide semiconductor.

DFT: Density functional theory.

DOS: Density of states.

EOR: End of range.

GGA: Generalized gradient approximation.

ITRS: International technology roadmap for semiconductors.

KLMC: Kinetic lattice Monte Carlo.

LDA: Local density approximation.

MBE: Molecular beam epitaxy

MC: Monte Carlo.

MD: Molecular dynamics.

NEB: Nudged elastic band.

NMOS: Negative-channel metal oxide semiconductor.

QMD: Quantum molecular dynamics.

RTA: Rapid thermal anneal.

SIMS: Secondary ion mass spectroscopy.

SOI: Silicon-on-insulator.

TCAD: Technology computer aided design.

TED: Transient enhanced diffusion.

PMOS: Positive-channel metal oxide semiconductor.

PW91: Perdew-Wang GGA functional.

QM: Quantum mechanics.

ULSI: Ultra large scale integration.

VASP: Vienna *ab-initio* simulation package.

VLSI: Very large scale integration.

XTEM: Cross-sectional transmission electron microscopy.

ACKNOWLEDGMENTS

First of all, I like to acknowledge the guidance and support of my research advisor Scott Dunham. He taught me everything I know about VLSI technology. His amazing insight is truly inspirational. The combination of freedom and constant accessibility was the perfect environment to make this dissertation possible and to learn how research is done. I could not have asked for a better advisor. Next, I like to thank the members of my reading committee, Hannes Jónsson and Marjorie Olmstead, for carefully reading the manuscript and giving me very valuable feedback. Also many thanks to the remaining members of my graduate committee: John Rehr, Steve Sharpe, Ron Merrill, and Daniel Gamelin. I would especially like to thank Daniel Gamelin for agreeing last minute to become the graduate school representative at my final examination.

A large fraction of the research presented in this dissertation was conducted during two internships (summer 2002 and 2003) at Texas Instruments in Dallas, TX. I am very grateful to my manager Chuck Machala for giving me the opportunity to work there. It was an extremely fruitful experience for me, particularly due to the interactions with Srini Chakravarthi. He was a constant source of new ideas and taught me how to explore the unknown. Thanks to him, I will remember both summers at Texas Instruments as a very exciting time. I also very much appreciate his careful reading of the manuscript and valuable feedback which shaped the final version of this dissertation. During my time at Texas Instruments I had also very productive interactions with P. R. Chidambaram ("Chidi") and Ivar Reimanis (Colorado School of Mines). In summary, the intern program at Texas Instruments was outstanding.

Special thanks to Graeme Henkelman, who helped me to get up to speed in the art of DFT calculations. He was always a great resource whenever I needed some additional insight. During the last couple months of my dissertation work, Andri Arnaldsson helped me to finish up the last remaining calculations. He is the person who looked out for "sleeping" computational resources to complete some of the projects. Thank you so much!

Finally, I like to acknowledge the Semiconductor Research Corporation (SRC) for funding this research and Intel for donating a computing cluster which was used for most of the calculations in this dissertation.

On the personal side, there are numerous people I need to show my appreciation for providing such a nurturing environment. First of all, I need to thank Cynthia Lin for making me pursuing my Ph.D. in the United States. Without her, I would have never gone on this journey which turned out to be the best decision of my life. I am very grateful.

The atmosphere in my research group was always extremely cheerful thanks to Chihak Ahn, Tom Christiansen, Terry Chong, Rui Deng, Pavel Fastenko, Jason Guo, Juan Huang, Shiho Iwanaga, Kjersti Kleven, Puneet Kohli, Leo Lam, Vijay Mani, Heidi Meyer, Ohseob Kwon, Zudian Qin, Kyle Retterer, Frank Schumacher, Chen-Luen Shih, Yeshwant Subramanian, Jean Wang, Fumin Yang, and Joo Chul Yoon. Michael Kummer and Adrienne Wat did an outstanding job in processing the countless travel and reimbursement forms.

Many thanks to my fellow countryman and regular lunch and boarding buddy Daniel Arndt. Sorry for giving you always such a hard time.

During my time in Dallas, I made a lot of friends and would like to thank every single one of them for the good times we had during both summers. I would especially like to mention Arthur Musa, Mei Jung Cheng, Carlo Zapata, Melisa Arzuaga, Tram

Dao, Yesenia Aguayo, Sigi St. Helene, Srini Chakravarthi, and Rashmi Narain. You all made this time unforgettable.

In the physics department, I am grateful to Chen-Shan Chin and Tom Luu, and my former officemates Kai Miller, Eric Lin, and Jutta Stegmaier for all the good times. It was a pleasure to get to know you.

A good network of friends is required to overcome the ups and downs of a five year Ph.D. Many thanks to all my Seattle friends: Jin Young Bae, Tom and Sophia Chang, Chao Chen, Sharon Chen, Wei-Yi Chu, Kimi Hiranaka, Denny Lee and Lisa Yang, Eric and Rachel Lin, Ingrid Lin, JJ and Christine Sato, and Jerry and April Yu. I will never forget the countless games nights, BBQs, and dinner parties. You were my family here in Seattle. I am especially grateful to Connie Yu for not only being such a great friend, but also for reading the final manuscript and hunting down the last typos and grammar slips.

Last, but not least, I need to thank my loving parents, Hildegard and Hans-Peter, and my brother Erfan back in Germany for their constant support and encouragement during my whole life. Without them I would have never been able to accomplished this task. They truly deserve the dedication of this dissertation.

Ihr seid die beste Familie, die ich mir wünschen kann.

DEDICATION

To my parents,

Hildegard and Hans-Peter,

and my brother,

Erfan.

Chapter 1

INTRODUCTION

Silicon technology has sustained an ongoing revolution during the almost 50 years since Jack Kilby (2000 Nobel Prize in Physics) built the first integrated circuit. During the summer of 1958, Jack Kilby was working at Texas Instruments in Dallas, and with borrowed and improvised equipment he conceived and built the first electronic circuit in which all of the components, both active and passive, were fabricated in a single piece of semiconductor material half the size of a paper clip. The successful laboratory demonstration of that first simple microchip on September 12th, 1958 made history [21]. The success story of VLSI technology is nicely illustrated by looking at the number of transistors per chip as a function of time, which is shown in Fig. 1.1. In 1965, Gordon Moore postulated that the number of transistors per chip would double every 18 months [1]. Figure 1.1 shows Moore's actual data (green line) as well as the development of memory (red line) and microprocessor chips (orange line) during the last 40 years. Moore's prediction still holds today; in fact, the original empirical observation is now referred to as Moore's law. The *International Technology Roadmap for Semiconductors* (ITRS) [16] lists the specifications of future devices which are required to meet this aggressive scaling law.

In 2000, the size of a single device reached the sub-100 nm regime. Hence, instead of talking about microchips, state-of-the-art devices are better referred to as nanochips. In fact, VLSI technology is among the first profitable mass-production applications of nanotechnology. Figure 1.2 shows a transistor of Intel's 90 nm gener-

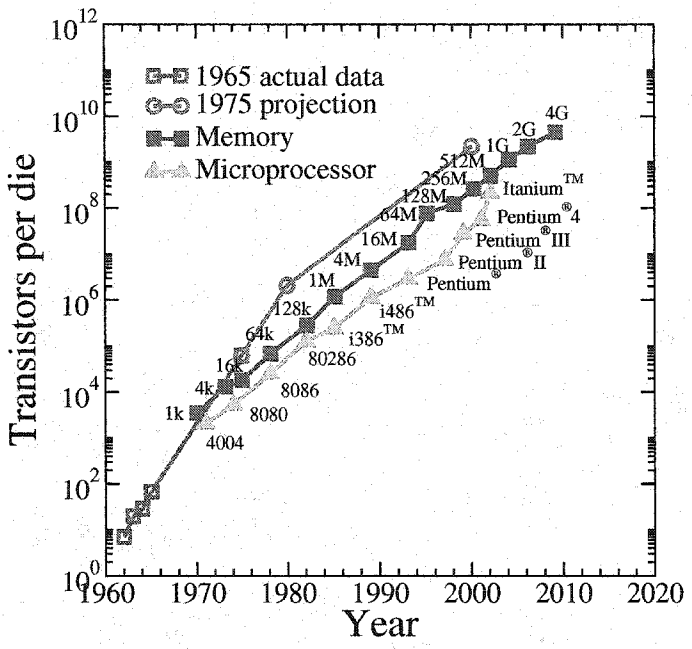

Figure 1.1: Illustration of Moore's law [1] based on the development of memory chips and Intel's well known microprocessor families [2]. Shown is the number of transistors per die (chip) as a function of time.

ation. The channel length of this device is only 50 nm. Table 1.1 lists some of the characteristic parameters of current CMOS devices and the predictions of the ITRS for coming years. In order to fulfill the challenges set by the ITRS, future devices will require the development of many new technologies. New materials like SiGe, high-K oxides or metal gates will be introduced. Also new geometries/device structures will be required. Currently silicon-on-insulator (SOI) technologies are already in use. The demand for multi-gate structures is just a matter of time. In the past, many choices for new technologies were explored predominantly by experiments. Nowadays the cost for such experiments is increasing dramatically, which demands very accurate process and device modeling in order to identify the key experiments. This requires the utilization of all available modeling techniques and their use in a complementary way. Technology computer aided design (TCAD) will play a crucial role in meeting

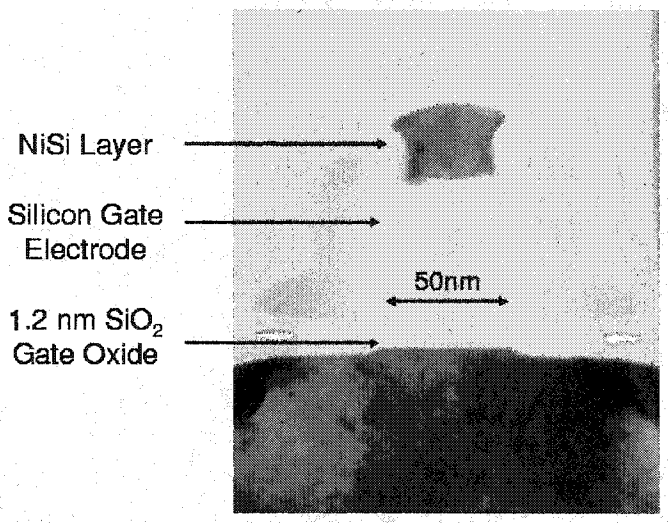

Figure 1.2: 90 nm generation NMOS device produced by Intel (50 nm channel length) using strained silicon technology [2].

Table 1.1: Summary of some of the characteristic device parameters for current and future CMOS devices published in the 2003 *International Technology Roadmap for Semiconductors* [16].

Year of production	2004	2007	2010	2013	2016
Technology node	90 nm	65 nm	45 nm	32 nm	22 nm
DRAM 1/2 pitch [nm]	90	65	45	32	22
MPU printed gate length [nm]	53	35	25	18	13
MPU physical gate length [nm]	37	25	18	13	9
S/D extension depth [nm]	20.4	13.8	7.2	10.4	7.2
Equivalent oxide thickness [nm]	1.2	0.9	0.7	0.6	0.5

the future goals set by the ITRS.

This dissertation shows how *ab-initio* techniques can be used to address a range of critical problems in current VLSI technology. We study the fundamental interactions

of impurities and intrinsic point-defects at the quantum level using density functional theory (DFT). The goal is to connect atomistic processes to macroscopic behavior, such as dopant diffusion and activation. In particular, we investigated using *ab-initio* methods two very different questions in VLSI technology: F co-implantation and stress effects on dopant diffusion/activation. This dissertation makes important contributions to the understanding of the underlying physical mechanism of these phenomena.

By determining formation and migration energies for various fluorine (F) complexes, we found a unique reaction mechanism which explains the anomalous F behavior. This is the first *ab-initio* work of this kind, as previous theoretical studies were limited to F migration without including the interaction of F with intrinsic point-defects [22, 23]. The mechanism found is the key to understanding the anomalous F behavior and effects of F on boron (B) and phosphorus (P) diffusion and activation. In addition, we developed a new methodology to address stress effects on dopant diffusion and activation from first-principles. This new method is capable of determining stress effects under arbitrary conditions. This enables the determination of anisotropies associated with more complex strain states. Our work is a generalization of previous work [24, 25, 26, 27, 28, 29], since we used a unique way to determine the general induced strain and elasticity tensors. We applied this methodology to study the effects of stress on point-defect/dopant diffusion and activation.

Chapter 2 gives a general overview of currently available modeling techniques. In addition, it is shown how the different modeling approaches form a modeling hierarchy in terms of the time and distance scales they operate at. Density functional theory (DFT), the *ab-initio* method in this work, plays a special role in this modeling hierarchy since it provides the foundation and thus contributes to all levels in the hierarchy. In the subsequent chapters, we utilize this fact and apply an *ab-initio* driven modeling approach to study selected problems in VLSI technology: the effect of fluorine (F) co-implantation (Chapters 3 and 4) and stress effects on point-defect

and dopant diffusion and activation (Chapters 5, 6, and 7) in silicon.

It has been shown experimentally that F co-implantation has beneficial effects on boron (B) and phosphorus (P) diffusion and activation. However, these effects are strongly dependent on the implant conditions. In addition, F exhibits anomalous diffusion behavior. In Chapter 3, we report the result of *ab-initio* calculations which explain the anomalous F behavior. We found strongly bound fluorine/vacancy complexes. Based on these results an extended multi-cluster model is developed to model the F behavior at the continuum level. In Chapter 4, the previous model is analyzed and reduced to a simplified version to model the co-implantation effects of F on boron and phosphorus diffusion.

Chapters 5, 6, and 7 address a very different open question in VLSI technology: stress effects on point-defect and dopant equilibrium concentration, diffusion and activation. Stress effects become more important in VLSI technology as steep doping gradients and hetero-interfaces induce stress gradients and reduced dimensions make any variation in diffusivity critical. On top of this, stress is induced purposefully to enhance carrier mobility. Figure 1.2 shows an NMOS device produced by Intel (90 nm generation), which utilizes stress effects to improve device performance. After developing a methodology to treat stress effects from first-principles (Chapter 5), *ab-initio* techniques are used to extract induced strains and elasticity tensors for various defects and impurities in order to predict the impact of arbitrary stress tensors. The results from first-principles calculations are used to describe analytically the effect of stress on point-defect and dopant diffusion, while kinetic lattice Monte Carlo simulations are used to quantify the full diffusivity tensor of interstitial (I) and B (Chapter 6). In Chapter 7, the effects of stress on B activation are investigated. Following the methodology in Chapter 5, a stress dependent B solubility model is developed. Finally, Chapter 8 summarizes the conclusions of the dissertation and suggest areas for future follow-on work.

In addition, there are six supporting chapters in the Appendices. Appendix A re-

views the concepts of local equilibrium of defects/impurities in solids which are used throughout this dissertation. Appendix B shows the structures of various interstitial configurations which are located at high symmetry points of the silicon lattice. In Appendices C and D, the density of states (DOS) of various fluorine/vacancy complexes are listed and details of the analysis of uncharged vs. charged super-cell calculations are discussed. Appendix E summarizes general analytic stress/strain relations, which are used in the Chapters 5, 6, and 7. Appendix F lists the transition vectors used in the analysis of stress effects on point-defect and dopant diffusion in Chapter 6. Finally, Appendix G addresses technical details and convergence issues of the DFT calculations with respect to the extracted parameters used in the Chapters 5, 6, and 7.

Chapter 2

MODELING TECHNIQUES

2.1 Modeling Hierarchy

The main goal in front-end process modeling [17] is prediction of the final doping profiles and their activation levels. Once these are known, Poisson's equation coupled with the carrier transport equations determines the device behavior [30, 31]. In the past, due to the size of the devices of interest, 1D doping profiles were sufficient to predict the device behavior reasonably well. However as ULSI technology reaches the nanoscale, accurate 2D and 3D doping profiles become necessary. In order to predict these profiles correctly and to use front-end process simulations in making the most beneficial process choices, a detailed understanding of the underlying physical mechanisms which control dopant diffusion and activation is required. In the past, front-end process modeling focused primarily on continuum simulations. The notion of point-defect mediated diffusion (see Section 2.2) is the key to modeling diffusion and activation at the macroscopic level. Section 2.3 summarizes the basic concepts of dopant diffusion and activation at the continuum level. However, this approach suffers from the fact that it usually involves many parameters, which need to be determined by fitting models to experimental data. Historically, many continuum models were just effective models without a strong foundation in terms of their physical mechanisms. While following Moore's law, parameters had to be refitted to new experimental data once a new technology generation with reduced device size was developed.

Since macroscopic phenomena like dopant diffusion and activation are directly related to atomistic processes (e.g., dopant diffusion in a solid is believed to be point-

defect mediated [30, 32, 17] (see Section 2.2)), *ab-initio* techniques can be used to determine the physical reaction mechanisms and parameters of the macroscopic processes. Ideally it is desired to treat a complete device at the atomistic level and simulate its behavior from first-principles. However this is currently still a hopeless task due to the involved time and distance scales. Currently available computational resources are not sufficient to treat such systems. However, it turns out that this problem can be overcome in a different way, since there are other techniques to bridge the gap in time and distance scales. Figure 2.1 shows the modeling hierarchy, which illustrates schematically some of the currently available techniques. On the most fundamental level there are *ab-initio* calculations. The *ab-initio* method used in this dissertation is density functional theory (DFT). A brief overview of DFT is given in Section 2.5. On the other end of the hierarchy there is continuum modeling. Section 2.3 reviews this approach. Molecular dynamics (MD) and kinetic lattice Monte Carlo (KLMC) (see Section 2.4) bridge the gap between the atomistic and continuum level. The basic idea is to utilize the whole modeling hierarchy by determining reaction mechanisms and/or parameters of less fundamental models from more fundamental theories. The arrows in Fig. 2.1 illustrate this approach. Since *ab-initio* calculations are most fundamental, they contribute to all levels in the modeling hierarchy.

Table 2.1 gives an overview of the potential of the different techniques with respect to currently available computational resources. Listed are system size (number of atoms and dimension) and corresponding physical time, which can be simulated currently within one day of CPU time. The number of atoms range from 100 in a 1 nm DFT super-cell to 10^8 in a continuum model for a 100 nm device. The simulated time scales range from psec in the case of quantum molecular dynamics (QMD) using DFT to msec/sec at the continuum level, where real process steps are simulated (e.g., RTA anneals).

In order to bridge the gap in time and distances scales, QMD can be approximated by standard classical MD. In molecular dynamics (MD) the time evolution

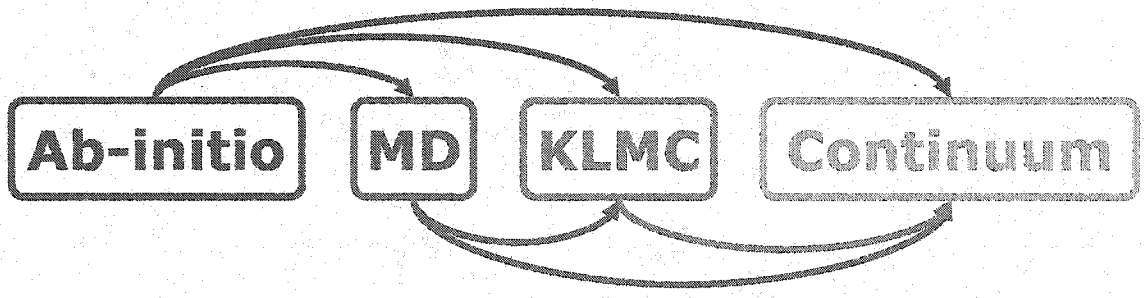

Figure 2.1: The modeling hierarchy shown above illustrates the different modeling techniques that address problems at very different time and distance scales (see Table 2.1). More fundamental methods are used to determine parameters of less fundamental theories (indicated by arrows). *Ab-initio* techniques set the foundation of this hierarchy. At the macroscopic level there are continuum simulations. Molecular dynamics (MD) and kinetic lattice Monte Carlo (KLMC) help bridge the gap between the atomistic and continuum level.

Table 2.1: Time and distance scales for various modeling techniques currently accessible within one day of CPU time (Pentium 4). The modeling techniques included make up the modeling hierarchy shown in Fig. 2.1.

Technique	DFT	MD	KLMC	Continuum
Interaction	QM	empirical potentials	migration barriers	reaction kinetics
Number of atoms	100	10^4	10^6	10^8
Length scale	1 nm	10 nm	25 nm	100 nm
Time scale	$\approx$ psec	$\approx$ nsec	$\approx$ msec	$\approx$ sec

of a system of atoms is determined based on the classical trajectory of the individual atoms according to chosen inter-atomic potential functions. This treatment assumes that the electron density responds instantaneously to ionic movements and thus the electronic degrees of freedom can be separated from the ionic degrees of freedom (Born-Oppenheimer approximation). These potential functions are based on

ab-initio calculations in QMD or empirical potentials for standard MD (e.g., in the simplest case Lennard-Jones type pairwise interaction potentials). For silicon systems the more complicated empirical potentials developed by Stillinger-Weber [33] and Tersoff [34] have proven to describe some physical systems reasonably accurately. These potentials also account for multi-body interactions. Since lattice vibrations, which determine the time evolution scale in standard MD simulations, are on the order of psec, only nsecs can be simulated with state-of-the-art computers. However there are various techniques to speed up time evolution in MD simulations: kinetic Monte Carlo (KMC) [35, 36], hyperdynamics [37], parallel replica method [38], temperature accelerated dynamics (TAD) [39], and dimer-KMC [40, 41] just to mention a few. The basic idea in all these techniques is to take advantage of the natural separation of time scales: vibration vs. transition times. At room temperature, atomic systems typically undergo 10^{10} lattice vibrations before changing their spatial atomic configuration significantly. This is exactly the reason why currently standard MD simulations are limited to nsecs. The latter transitions can be described by transition state theory (TST). They are "rare events" in comparison to the lattice vibrations. The acceleration methods try to speed up the MD simulation by estimating the time of the next transition using different approaches.

KLMC is a special type of KMC. Lattice vibrations are completely ignored and only used to provide a general time scale. In KLMC the system is restricted to a finite number of well characterized transitions on a lattice. This is sufficient to treat diffusion in a crystalline material like Si, but does not allow the treatment of amorphous materials. Section 2.4 summarizes the basic ideas of the KLMC technique.

In the near future, MD simulations will become particularly important, since there is great need to model processes like low energy ion-implantation and epitaxial regrowth with parameter free physical models. Anneal times have reached time scales where technologically important physical processes happen during the epitaxial regrowth. One example is the accurate description of implant damage, which has direct

impact on dynamic processes like transient enhanced diffusion (TED) [42, 17] and dopant activation. Modeling ion-implantation and epitaxial regrowth involves the treatment of amorphous materials. Currently *ab-initio* techniques are computationally too intensive due to the high number of degrees of freedom of such systems; MD is the only current technique available.

In this dissertation we will show how this hierarchy of techniques can be used to describe macroscopic phenomena at the continuum level, based on *ab-initio* calculations and KLMC simulations. Physical problems need to be modeled by utilizing all techniques of the modeling hierarchy with particular focus on their individual modeling strengths. The modeling hierarchy needs to be understood as one modeling tool and not only as individual techniques.

In the following sections, the concepts of the different modeling techniques are summarized and it is shown how they contribute to the modeling hierarchy. Since point-defect mediated diffusion is an atomistic process which links all the techniques together, it is reviewed first in the next section. Then starting at the macroscopic end of the modeling hierarchy, the different techniques are summarized. Continuum modeling in Section 2.3, followed by the kinetic lattice Monte Carlo (KLMC) technique in Section 2.4, and finally density functional theory (DFT) in Section 2.5.

2.2 Point-defect mediated diffusion

At finite temperature, intrinsic point-defects are present in any crystalline material, since this reduces the energy of the crystal due to the associated entropy of mixing [30]. These point-defects are the key to understanding diffusion of impurities in a solid. The simplest point-defects are vacancies (vacant lattice site) and interstitials (additional atom in interstitial lattice site). While most impurities located at lattice sites are considered immobile, these become mobile by interacting with intrinsic point-defects. The impurity and the point-defect form a mobile impurity/point-defect pair.

Since there are two types of basic point-defects, there are also two different migration mechanisms.

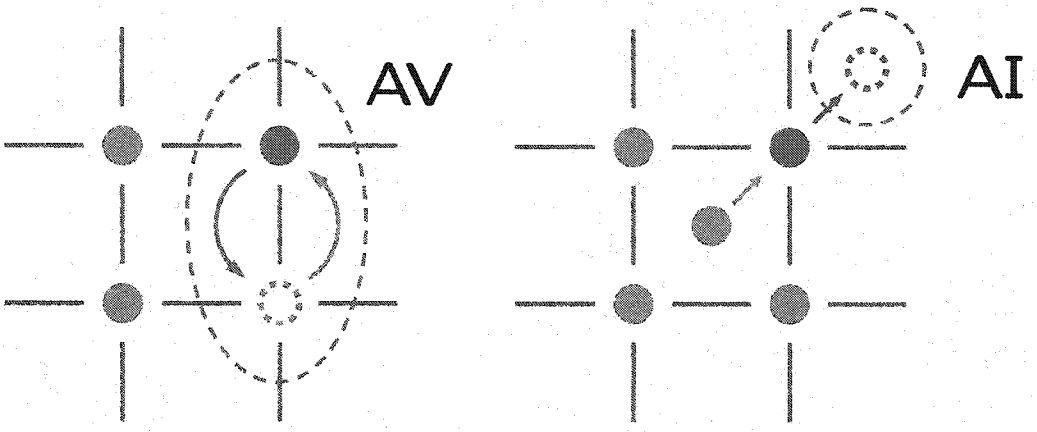

Figure 2.2: Left: Vacancy-assisted diffusion. Right: Interstitial-assisted diffusion.

Figure 2.2 shows the processes for vacancy-assisted (left) and interstitial-assisted diffusion (right) in a simple 2D square lattice. In the case of vacancy-assisted diffusion, the impurity atom A (blue solid circle) jumps from its original position into the vacant site V (green dashed circle). The mobile species is called an AV pair. For further diffusion, either an additional vacancy needs to be present or the original vacancy needs to approach the defect atom from a different direction by passing through a second nearest neighbor (NN) site (3rd NN in case of Si or diamond structure). In the case of interstitial-assisted migration, there are several different mechanisms. The primary reason for this is the existence of many interstitial configurations (e.g., <100> split interstitial (I_{split}), interstitial in tetrahedral location I_{tet}, interstitial in hexagonal site I_{hex}). The spatial configurations of these point-defects are shown in Appendix B. The so called "kick-out" mechanism shown in Fig. 2.2 (right) best illustrates the idea of interstitial-assisted diffusion. A mobile interstitial atom kicks out the substitutional impurity atom A into an interstitial lattice site. This interstitial impurity atom AI is now mobile and migrates through the solid, until it "kicks out" a Si atom from its

lattice site.

The transition barriers associated with the different transitions can be calculated using *ab-initio* methods (see Section 2.5). The diffusivity is directly related to the migration barrier E_m:

$$D = D_0 \exp\left(-\frac{E_m}{kT}\right). \tag{2.1}$$

Since there are two migration mechanisms, in principle an impurity can utilize both of these mechanisms to diffuse. In fact, some impurities diffuse using both migration methods, others predominantly use just interstitial or vacancy-assisted migration. Table 2.2 lists the experimental observations for various dopants. f_I and

Table 2.2: Migration method of Si and other common dopants in silicon [17, 18]. f_I and $f_\mathrm{V} = (1 - f_\mathrm{I})$ are the fractions of interstitial and vacancy-assisted diffusion respectively for intrinsic material at equilibrium. f_I and f_V show only a weak temperature dependence.

Impurity	f_I	f_V
Si	0.6	0.4
B	0.99	0.01
P	0.98	0.02
As	0.4	0.6
Sb	0.02	0.98

$f_\mathrm{V} = (1 - f_\mathrm{I})$ are the fractions of interstitial and vacancy-assisted diffusion respectively. The fact that diffusion of impurities requires point-defects has interesting consequences on non-equilibrium diffusion. As an example, ion-implantation introduces additional interstitials. The interstitial concentration C_I increases in comparison to the equilibrium interstitial concentrations C_I^* ($C_\mathrm{I} > C_\mathrm{I}^*$). This leads to an enhanced diffusivity for interstitial diffusers like B. Energetically, the formation of a BI pair is favored in the presence of additional interstitials. Equation 2.2 summarizes this fact

mathematically. The effective diffusivity of a species A is expressed as a function of the point-defect concentrations C_{I} and C_{V}:

$$D_{\mathrm{A}}^{eff} = D_{\mathrm{A}}^{*}\left(f_{\mathrm{I}}\frac{C_{\mathrm{I}}}{C_{\mathrm{I}}^{*}} + f_{\mathrm{V}}\frac{C_{\mathrm{V}}}{C_{\mathrm{V}}^{*}}\right), \tag{2.2}$$

where D_{A}^{*} is the equilibrium diffusivity of species A. C_{I}^{*} and C_{V}^{*} are the equilibrium point-defect concentrations of I and V respectively. C_{I} and C_{V} label the present point-defect concentration of I and V respectively.

The next section explains, how the idea of point-defect mediated diffusion can be applied to modeling dopant diffusion and activation at the continuum level.

2.3 Continuum modeling

Amongst the most important phenomena in front-end process modeling are dopant diffusion and activation [17]. Out-of-equilibrium dopant diffusion (e.g., following ion-implantation) can no longer be described by simple Fickian diffusion [32]. Point-defects are key to understanding dopant diffusion and activation in a crystalline material. The previous section focused on summarizing the basic ideas of point-defect mediated diffusion by looking at the atomic processes involved. Based on these ideas Sections 2.3.1 and 2.3.2 illustrate how dopant diffusion and activation are modeled at the continuum level.

2.3.1 Dopant diffusion

Based on the atomistic processes described in the previous section, diffusion can be modeled at the continuum level. For illustration purposes, we consider boron diffusion. Table 2.2 shows that B is essentially a pure interstitial diffuser, which reduces the number of equations used to describe the diffusion process. It is straightforward to extend the approach to other impurities with different point-defect interactions.

In the following, we develop a very simplified B diffusion model, which includes only B, BI, I, and V. In reality, B interacts strongly with larger point-defect clusters;

however, for illustration purposes it is convenient to consider only a few species. Section 2.3.2 addresses the clustering behavior of B into B_nI_m clusters and the associated deactivation process.

Equation 2.3 lists the possible reactions of all species with each other. I, V, and BI are considered mobile, whereas B is immobile. The first equation describes the formation of a mobile BI pair, whereas the second the dissolution of a BI pair with a V. The third reaction accounts for I-V recombination:

$$\begin{aligned} \mathrm{B} + \mathrm{I} &\Leftrightarrow \mathrm{BI}, \\ \mathrm{BI} + \mathrm{V} &\Leftrightarrow \mathrm{B}, \\ \mathrm{I} + \mathrm{V} &\Leftrightarrow \emptyset. \end{aligned} \tag{2.3}$$

In equilibrium, the law of mass action relates the concentrations of the initial species of a reaction to the concentrations of the final complexes. The products of the concentrations of the initial and final species are proportional to each other:

$$\begin{aligned} C_{\mathrm{B}}C_{\mathrm{I}} &= K_{eq}(T)C_{\mathrm{BI}}, \\ C_{\mathrm{BI}}C_{\mathrm{V}} &= \tilde{K}_{eq}(T)C_{\mathrm{B}}, \end{aligned} \tag{2.4}$$

where $K_{eq}(T)$ and $\tilde{K}_{eq}(T)$ are proportionality constants, which are only a function of temperature. These constants are determined by the difference in formation energies of the individual complexes. Appendix A discusses how the formation energy of a complex determines its equilibrium concentration and thus determines $K_{eq}(T)$ and $\tilde{K}_{eq}(T)$ using Eq. 2.4.

The relations in Eq. 2.4 only apply in equilibrium; however, we are interested in the diffusion of B in out-of-equilibrium conditions. A reaction rate R_i is associated with each of the above reactions. In equilibrium this rate vanishes ($R_i = 0$). The reaction rate R_1 for $\mathrm{B} + \mathrm{I} \Leftrightarrow \mathrm{BI}$ can be written as:

$$\begin{aligned} R_1 &= k_f C_{\mathrm{B}}C_{\mathrm{I}} - k_r C_{\mathrm{BI}}, \\ &= k_f (C_{\mathrm{B}}C_{\mathrm{I}} - \frac{k_r}{k_f} C_{\mathrm{BI}}), \\ &= 4\pi a D_{\mathrm{I}} (C_{\mathrm{B}}C_{\mathrm{I}} - K_{eq}C_{\mathrm{BI}}). \end{aligned} \tag{2.5}$$

Similar to the law of mass action, the forward and reverse reaction rates are proportional to the product of the concentrations of the reacting species, with k_f and k_r the respective proportionality constants. In equilibrium R_1 has to vanish, thus $k_r/k_f = K_{eq}$. Since k_f and k_r are just constants, this relation also holds out-of-equilibrium. Assuming diffusion limited reactions, k_f can be parameterized as $k_f = 4\pi a D_{\mathrm{I}}$, where D_{I} is the diffusivity of I and a is the effective capture radius. Similarly, the reaction rates for the remaining two reactions in Eq. 2.3 can be determined:

$$\begin{aligned} R_2 &= 4\pi a \left(D_{\mathrm{BI}} + D_{\mathrm{V}}\right)\left(C_{\mathrm{BI}} C_{\mathrm{V}} - \tilde{K}_{eq} C_{\mathrm{B}}\right), \\ R_3 &= 4\pi a (D_{\mathrm{I}} + D_{\mathrm{V}})(C_{\mathrm{I}} C_{\mathrm{V}} - C_{\mathrm{I}}^* C_{\mathrm{V}}^*), \end{aligned} \tag{2.6}$$

where D_{BI}, D_{I}, and D_{V} are the diffusivities of BI, I, and V. C_{I}^* and C_{V}^* are the intrinsic I and V equilibrium concentrations.

The time evolution of every single species is described by the generalized continuum equation:

$$\frac{\partial C}{\partial t} + \vec{\nabla} \cdot \vec{J} = \sum_n R_n, \tag{2.7}$$

where $\vec{J} = -D\vec{\nabla}C$ is the diffusion flux of a mobile species and $\sum_n R_n$ is the sum of reaction rates with other complexes. Combining these equations leads to a set of partial differential equations describing the diffusion of B for arbitrary I and V concentrations:

$$\begin{aligned} \frac{\partial C_{\mathrm{B}}}{\partial t} &= -R_1 + R_2, \\ \frac{\partial C_{\mathrm{BI}}}{\partial t} &= \vec{\nabla} \cdot (D_{\mathrm{BI}} \vec{\nabla} C_{\mathrm{BI}}) + R_1 - R_2, \\ \frac{\partial C_{\mathrm{I}}}{\partial t} &= \vec{\nabla} \cdot (D_{\mathrm{I}} \vec{\nabla} C_{\mathrm{I}}) - R_1 - R_3, \\ \frac{\partial C_{\mathrm{V}}}{\partial t} &= \vec{\nabla} \cdot (D_{\mathrm{V}} \vec{\nabla} C_{\mathrm{V}}) - R_2 - R_3. \end{aligned} \tag{2.8}$$

The parameters of this model are K_{eq}, $\tilde{K}_{eq}$, D_{I}, D_{V}, D_{BI}, and a, which can be determined from *ab-initio* calculations or fit to experimental data. Once the initial spatial concentrations and boundary conditions of the different species are known, the time

evolution can be computed. Commercial TCAD process simulators like TSUPREM4 [43] or ISE-FLOOPS [44] solve such sets of differential equations.

2.3.2 Dopant activation

Dopant activation/deactivation is closely related to clustering of dopants with point-defects. As an example, group III or V dopants located at substitutional lattice sites accept or donate one electron to the Si crystal. Thus every dopant atom ideally contributes one electron or hole to the conduction. However, since dopant atoms usually interact with point-defects forming e.g., charge neutral dopant/defect clusters, not every dopant atom can be considered electrically active. In the case of B, B_nI_m clusters reduce the fraction of electrically active B and therefore are responsible for deactivation. In order to model this dynamic process, the formation and dissolution of such clusters need to be considered. Besides the effect on the electrical properties of the material, B_nI_m clusters also alter the diffusion behavior of B, since the B_nI_m clusters are considered immobile for $n, m > 1$.

Equation 2.9 lists schematically the additional B_nI_m cluster formation and dissolution reactions:

$$\begin{aligned} B_nI_m &+ BI \Leftrightarrow B_{n+1}I_{m+1}, \\ B_nI_m &+ I \Leftrightarrow B_nI_{m+1}, \\ B_nI_m &+ V \Leftrightarrow B_nI_{m-1}. \end{aligned} \tag{2.9}$$

In addition, larger extended point-defect clusters have a strong impact on the B activation process. Equation 2.10 lists the interaction cascade of I_n and V_n clusters:

$$\begin{aligned} I_n &+ I \Leftrightarrow I_{n+1}, \\ I_n &+ V \Leftrightarrow I_{n-1}, \\ V_n &+ V \Leftrightarrow V_{n+1}, \\ V_n &+ I \Leftrightarrow V_{n-1}. \end{aligned} \tag{2.10}$$

Once the formation energies of the individual dopant/point-defect clusters are known, following the approach of the previous section, an extended set of partial

differential equations describing the activation/deactivation process can be derived. Often the parameters of such extended models are determined using an inverse modeling approach, however *ab-initio* calculations can also be used to identify the energetically favorable reactions by determining the formation energies and transition barriers of the involved reactions. This is a particularly powerful approach, since it leads to more physically accurate models which can be used to predict new situations for which there is not experimental data.

2.4 Kinetic lattice Monte Carlo

This section summarizes the basic idea behind the kinetic lattice Monte Carlo technique. More details can be found in the Refs. [45, 32].

To overcome the limitations in terms of physical simulation time in standard MD simulations, lattice vibrations are completely ignored in kinetic Monte Carlo simulations (KMC) [35, 36]. All transitions are modeled via transition state theory (TST) and the time evolution of an atomic system is determined via a set of predetermined states and transitions. The time scale associated with the lattice vibrations (attempt frequency) is only used to convert system time into real physical time. Lattice vibrations are responsible for the equilibration process in between transitions. This process is assumed to happen on a timescale short compared to the time between transitions. This is a valid assumption as long as all transition states are separated from the ground state configurations by several kT.

Kinetic lattice Monte Carlo (KLMC) is a special variation of kinetic Monte Carlo (KMC). Instead of describing the system states in the continuum, a lattice is used to define system states. This is a valid assumption in a crystalline solid, but breaks down for amorphous materials. The definition of states on a crystal lattice is very simple, since the crystal itself discretizes the atomic configurations.

Figure 2.3 (left) shows schematically such a lattice. Here, for simplicity we only

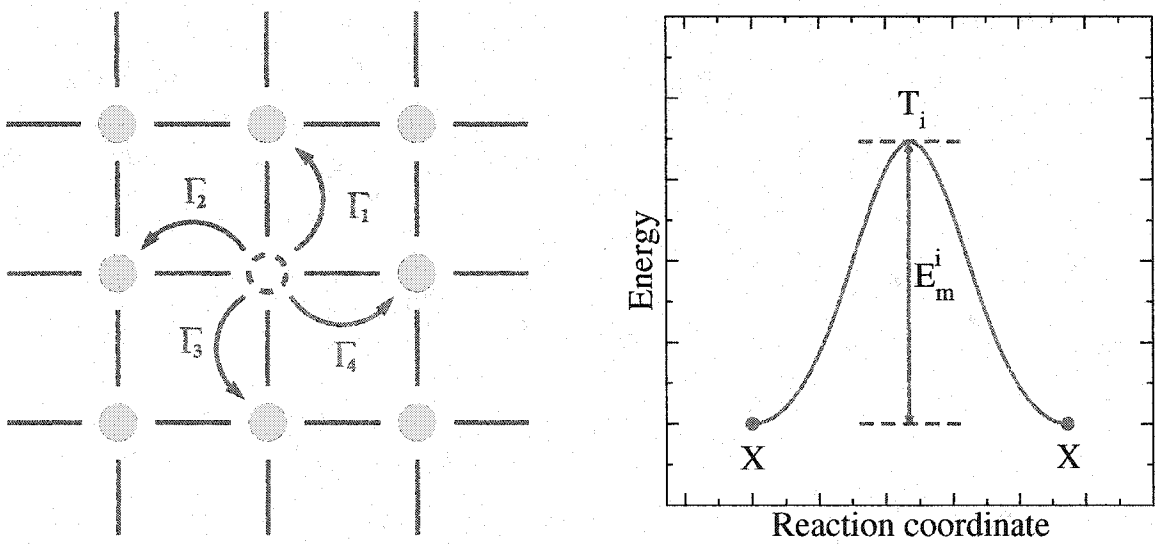

Figure 2.3: Left: KLMC lattice for a defect/impurity atom X (blue dashed atom) in a crystal. The defect can only occupy lattice sites and the transition rates for transition in the individual directions are given by Γ_1-Γ_4. These rates determine the transition probabilities and therefore the time evolution of the system. Right: Transition barrier E_m^i for transition i. T_i is the transition state.

consider the time evolution of a single defect/impurity atom (blue dashed circle). The defect/impurity atom can reside on each lattice site. The reaction rates in the different directions are Γ_1-Γ_4. To migrate from one lattice site to the next, the defect/impurity needs to overcome a transition barrier (see Fig. 2.3 (right)). In harmonic transition state theory (hTST), the transition rate is directly related to the migration barrier E_m^i by:

$$\Gamma_i = \Gamma_0 \exp\left(-\frac{E_m^i}{kT}\right), \tag{2.11}$$

where Γ_0 is proportional to the lattice vibration frequency [32]. *Ab-initio* techniques can be used to determine the migration energies E_m^i and rates [46]. The transition rates completely determine the time evolution of the system. Assuming uncorrelated events (the equilibration process between transitions assures this), the transition rates

determine the jump probabilities p_i in the different directions:

$$p_i = \frac{\Gamma_i}{\sum_{j=1}^{4} \Gamma_j}. \tag{2.12}$$

Once these probabilities are known, the time evolution of the system can be simulated using the standard Monte Carlo approach. The defect/impurity atom performs a random walk through the solid. To keep track of the actual physical system time, the time for each migration process Δt can be calculated using the individual transition rates: $\Delta t = 1/\Gamma$, where

$$\frac{1}{\Gamma} = \sum_i \frac{1}{\Gamma_i}. \tag{2.13}$$

Diffusion can be also viewed as a stochastic process; early work by Einstein relates the macroscopic diffusivity tensor $\mathbf{D}$ to the average displacement vector $\Delta\vec{x}$ of a random walk [32]:

$$D_{ij} = \frac{1}{2t}\langle \Delta x_i \Delta x_j \rangle, \tag{2.14}$$

where t is the time of a N-step random walk ($t = \sum_{i=1}^{N} \Delta t_i$) and Δx_i is a component of the displacement vector $\Delta\vec{x}$. Using KLMC, the diffusivity of a defect/impurity can be determined. This approach is used in Chapter 6 to study the effect of stress on interstitial diffusion. So far we only considered the migration of a single defect/impurity atom. However this approach can be extended straightforwardly to include more complex multi-atom clusters and multiple defects/impurities. To predict the time evolution of such complex states, all possible states and transitions rates need to be provided.

KLMC can be used in various ways. Fundamental questions like effect of stress on dopant diffusion (see Chapter 6) can be studied, in addition to prediction of 2D and 3D doping profiles, including, for example, the effect of dopant fluctuations [45].

2.5 Density functional theory

In the following section, the basic ideas of density functional theory (DFT) are summarized, and then it is shown how DFT calculations are used to address diffusion and

activation phenomena in semiconductors.

2.5.1 Theoretical overview

Calculations of ground state and excited state properties have been one of the major goals of condensed matter physics. Solving an N-electron problem is extremely difficult. Even numerical approaches are limited to small atomic or molecular systems, due to complexity of the calculations. The computational effort depends exponentially on the number of electrons. Besides the additional difficulties associated with the Coulombic interactions of the electrons [47], the high dimensionality of the N-electron wave function $\psi(\vec{r_1}, \ldots, \vec{r_N})$ makes a brute force approach impossible. The basic idea of density functional theory (DFT) is very similar to the Hartree-Fock (HF) approximation. In HF, instead of solving the exact N-electron Schrödinger equation, one solves a set of one-electron Schrödinger equations with an effective potential that approximates the interactions with the other $N-1$ electrons. This effective one-electron potential is derived by approximating the N-particle wave function by a Slater determinant of single electron orbitals. Applying a variational functional leads to the Hartree-Fock equations, which can be solved self-consistently. In DFT, instead of solving the original problem associated with the N-particle Hamiltonian:

$$\hat{H} = \hat{T} + \hat{V}_{ee} + \sum_{i=1}^{N} V_{ext}(\vec{r_i}), \tag{2.15}$$

an equivalent problem, which just depends on the electron density:

$$n(\vec{r}) \equiv \langle\psi|\psi^{\dagger}(\vec{r})\psi(\vec{r})|\psi\rangle \tag{2.16}$$

instead of the N-particle wave function $\psi(\vec{r_1}, \ldots, \vec{r_N})$ is solved. $\hat{T}$ and $\hat{V}_{ee}$ are the operators of the kinetic and electron-electron interaction energy respectively. V_{ext} is some external potential (e.g., the ionic potential in a solid). The justification of this approach is the Hohenberg-Kohn theorem [48]. Hohenberg and Kohn showed that

there exists a variational functional $E[n(\vec{r})]$ for the ground state energy of the N-electron problem, where the electron density $n(\vec{r})$ is the varied quantity. In principle, this theorem makes DFT an exact theory for the ground state without any approximation. The theorem further states the general form of the functional $E[n(\vec{r})]$:

$$E_{V_{ext}}[n] \equiv \int d^3r\, V_{ext}(\vec{r})n(\vec{r}) + F[n] \geq E_{GS}, \tag{2.17}$$

where

$$F[n] = \min_{\{\psi\}\to n} \langle\psi|\hat{T} + \hat{V}_{ee}|\psi\rangle. \tag{2.18}$$

The functional $F[n]$ describes an interacting N-electron gas. Once $F[n]$ is known, $E_{V_{ext}}[n]$ follows directly for any arbitrary external potential $V_{ext}(\vec{r})$ using Eq. 2.17. The minimum in Eq. 2.18 is taken over all N-electron wave functions ψ, which lead to the same electron density n. E_{GS} is the ground state energy of the system with $E[n_{GS}] = E_{GS}$. Equation 2.18 shows the definition of $F[n]$ by Levy [49], who further generalized the original work by Hohenberg and Kohn.

This theorem created a lot of excitement, since it promotes DFT to an exact theory once the universal functional $F[n]$ is found. Unfortunately the Hohenberg-Kohn theorem does not provide the exact functional form of $F[n]$. The search for this functional $F[n]$ has been restricted to educated guesses and so far it has not been found.

Currently, the most widely used functional was suggested by Kohn and Sham [50]. It predicts very accurately many ground state properties:

$$E_{KS}[\phi_1, ..., \phi_N] = \underbrace{\sum_{i=1}^{N} \int d^3r \frac{\hbar^2}{2m} |\vec{\nabla}\phi_i|^2}_{T} + \underbrace{\frac{e^2}{2} \int\int d^3r d^3r' \frac{n(\vec{r})n(\vec{r}')}{|\vec{r} - \vec{r}'|}}_{E_{direct}} \tag{2.19}$$

$$+E_{xc}[n] + \underbrace{\int d^3r V_{ext}(\vec{r})n(\vec{r})}_{E_{ext}}, \tag{2.20}$$

where

$$n(\vec{r}) = \sum_{i=1}^{N} |\phi_i(\vec{r})|^2. \tag{2.21}$$

In contrast to early versions of DFT, e.g. the Thomas-Fermi model, which suffers from the inadequate description of the kinetic energy operator, Kohn and Sham overcame this problem by reintroducing single electron orbitals ϕ_i to describe the kinetic energy operator. The physical meaning of these orbitals and single particle energies is unclear. Key to the Kohn-Sham functional is the exchange-correlation functional $E_{xc}[n]$, which accounts for the Fermionic behavior of electrons (effects due to the Pauli exclusion principle and anti-symmetry of the wave function). The Kohn-Sham equations are derived by applying a variational functional in respect to n and ϕ_i on Eq. 2.20. Similar to the Hartree-Fock approach, the resulting equations, which depend on n and ϕ_i, can be solved self-consistently by using the relation between the electron density n and the single electron orbitals ϕ_i shown in Eq. 2.21.

Considerable effort has been spent on finding improved exchange-correlation functionals $E_{xc}[n]$. In local density approximation (LDA), $E_{xc}[n]$ is expressed by the exchange functional of a homogeneous non-interacting electron gas $E_{xc}[n] \propto \int d^3r\, n^{4/3}(\vec{r})$. LDA can be extended to also account for spin effects by separating the electron density n into spin-up $n_\uparrow$ and spin-down $n_\downarrow$ electron densities. This version of LDA is referred as local spin density approximation (LSD). Another variation is the generalized gradient approximation (GGA). To account for local weak gradients in the electron density, the exchange-correlation functional $E_{xc}[n]$ is parameterized by n and $|\nabla n|$: $E_{xc}[n] = \int d^3r\, f(n, |\nabla n|)$. There are different versions of GGA, which differ in the parameterizing function $f(n, |\nabla n|)$ [51, 19]. In this dissertation, we use the widely used GGA functional PW91 [51]. In contrast to metallic materials which have a fairly uniform electron density, semiconductors exhibit large local gradients in the electron density within the unit cell due to covalent bonds. This suggests that GGA functionals are the better choice in comparison to LDA. Besides LDA and GGA there are other flavors of DFT. For example, a very popular functional in quantum chemistry is B3LYP.

Table 2.3 compares the experimental atomization energies of various molecules

Table 2.3: Comparison of the experimental atomization energy of various molecules with the theoretical predictions of different techniques (Hartree-Fock, LDA, GGA) [19].

	Li_2	C_2H_2	20 simple molecules (mean absolute error)
Experiment	1.04 eV	17.56 eV	–
Theoretical errors:			
Hartree-Fock	−0.91 eV	−4.81 eV	3.09 eV
LDA	−0.04 eV	2.39 eV	1.36 eV
GGA (PW91)	−0.17 eV	0.43 eV	0.35 eV

with Hartree-Fock, LDA, and GGA calculations. Both LDA and GGA show strong improvement in the predictive power over Hartree-Fock. Comparing LDA with GGA predictions suggests GGA to be more accurate. In general, DFT gives high quality predictions for differences in total energy (e.g., atomization energies). Nevertheless, there are well known problems. For example, LDA and GGA underpredict the Si band gap or, even worse, predict Ge to be a metal rather a semiconductor. Since the Kohn-Sham theory tries to capture correlation effects without explicitly building them into the wave function, phenomena which require explicit treatment of correlation effects like superconductivity in bulk matter or Van der Waals interactions between molecules, cannot be treated reliably [52].

George Bertsch states: "DFT is not at all systematic, and in the end its only justification is the quality of its predictions. However, it is rightly described as an *ab-initio* framework, giving theories whose parameters are determined *a priori* by general considerations" [52]. More complete reviews on general many-body physics and DFT can be found in the Refs. [53, 54, 52, 47].

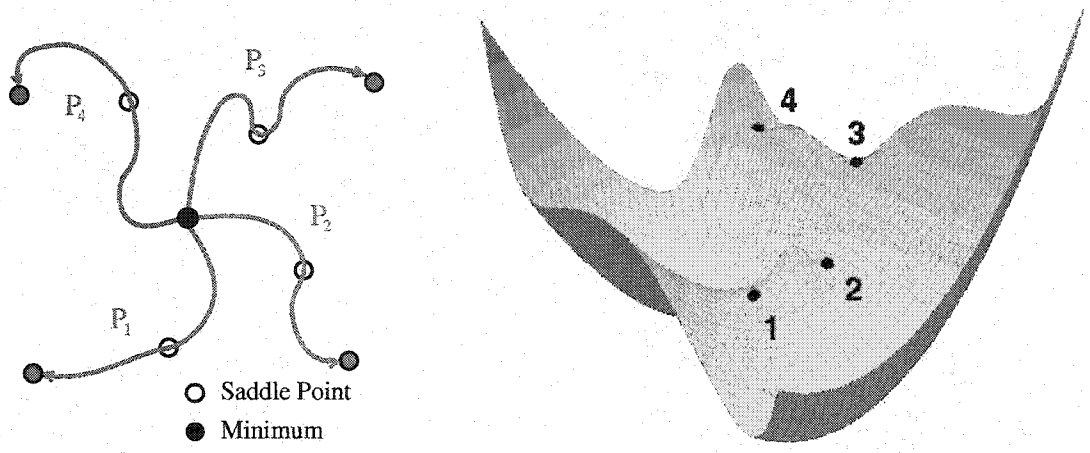

Figure 2.4: Left: Schematic plot of the transition paths between local minima. $P1$-$P4$ correspond to paths on the $3N$ dimensional energy surface shown on the right. Right: Schematic plot of the energy surface of a system of N atoms ($3N$ spatial degrees of freedom). To determine transition barriers the saddle points 1-4 need to be determined.

2.5.2 Applications of DFT

In this dissertation, we use DFT to study diffusion and activation in silicon. Both phenomena are related to calculating formation and migration energies and entropies of impurities and intrinsic defects including their complexes in a solid. Assuming the Born-Oppenheimer approximation, which allows the separation of the electronic and ionic degrees of freedom, the ground state energies of arbitrary ionic configurations can be determined.

Figure 2.4 (right) shows schematically the energy surface corresponding to the ionic degrees of freedom of a system with N atoms ($3N$ spatial degrees of freedom). Each point on this energy surface corresponds to a specific atomic configuration. As mentioned in Sections 2.3 and 2.4, to study diffusion and activation at the different levels in the modeling hierarchy, we are interested in finding the minimum energy configurations of certain atomic topologies as well as the transition paths and migration barriers between these individual low energy atomic configurations (see Fig. 2.4

(left)). To determine the migration barriers, the energies of the saddle points shown in Fig. 2.4 (right) need to be determined.

Due to the high dimensionality of the problem (there are $3N$ degrees of freedom), special techniques need to be used to find these saddle points. In this dissertation we extensively used the nudged elastic band (NEB) method [10, 11, 12]. In this approach, the initial and final ionic configuration need to be specified. The transition path is guessed by linear interpolation and improved successively by calculation of the gradient of the energy surface (ionic forces). Other approaches, like the dimer method [55], do not require the specification of the final transition state. This technique is very powerful for exploring energy surfaces such as that shown in Fig. 2.4 and finding new transition paths and minimum energy configurations.

More details on these techniques can be found in the respective references.

2.6 Summary

In this chapter, an overview of various modeling techniques was given. Each of these techniques targets a special time and distance scale with a particular modeling strength. Considering the fact that all methods are part of a global modeling hierarchy, it is extremely important to utilize all of them to complement each other in order to overcome the challenges of future solid state processes. The modeling hierarchy needs to be understood as one modeling tool and not only as individual techniques.

In this work, we will use DFT to calculate minimum energy configurations and the transition energies between them. These determine the transition rates used in KLMC (see Section 2.4) and provide reaction rates and diffusivities at the continuum level (see Section 2.3). In the following chapters we show that DFT calculations are an excellent tool to explore reaction mechanisms to develop physical continuum models and predict experimentally difficult to determine parameters.

Chapter 3

FLUORINE DIFFUSION IN SILICON

Implanted fluorine has been observed to behave unusually in silicon, manifesting apparent uphill diffusion [3] and reducing diffusion and enhancing activation of boron [56, 57, 58, 59, 60]. To investigate fluorine behavior, we calculated the energy of fluorine defect structures in the framework of density functional theory (DFT). We identified the ground state configuration and diffusion migration barrier of a single fluorine atom in silicon and found a set of energetically favorable fluorine vacancy complexes (F_nV_m). The decoration of vacancies/dangling silicon bonds by fluorine suggests that fluorine accumulates in vacancy rich regions, which explains the fluorine redistribution behavior reported experimentally.

3.1 Anomalous F diffusion

As ULSI devices enter the nanoscale, ultra-shallow and highly electrically active junctions become necessary. The current method of choice to introduce dopants into silicon is ion-implantation. During the implant process, the crystal structure of the host material (silicon) gets severely damaged. Subsequent high temperature anneals are required to heal the damage as well as activate the introduced dopants. During such anneals, transient enhanced diffusion (TED) of dopants is observed. Reduction in TED and enhanced dopant activation are of crucial importance for the formation of ultra-shallow junctions in future silicon process technology. Experimentally, fluorine (F) has been shown to have beneficial effects, reducing TED for boron (B) and phosphorus (P) [56, 57, 58, 59, 60] and enhancing boron activation [56, 57]. How-

ever, to utilize these benefits effectively, a fundamental understanding of the complex F behavior is necessary, particularly since F shows anomalous diffusion [3]. In this chapter, we present *ab-initio* calculations conducted within the framework of density functional theory (DFT), which find energetically favorable fluorine defect structures. These structures suggest a distinct redistribution behavior of F and also explain the beneficial effects of F on B and P TED reduction and enhanced dopant activation.

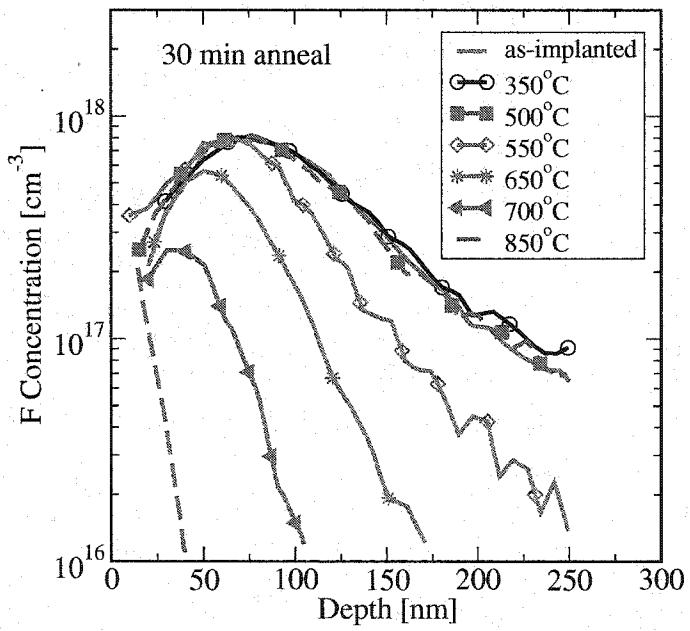

Figure 3.1: Fluorine SIMS profiles for a $10^{13}\,\mathrm{cm}^{-2}$ 30 keV F^+ implant (sub-amorphizing) after a 30 min anneal at various temperatures reported by Jeng *et al.* [3].

Figure 3.1 shows data reported by Jeng *et al.* [3]. In their experiment, a sub-amorphizing dose of $10^{13}\,\mathrm{cm}^{-2}$ F^+ was implanted at 30 keV and annealed for 30 min at various temperatures. The anomalous fluorine redistribution behavior consists of two key features. First at temperatures below 550 °C, no noticeable F diffusion takes place, while at higher temperatures, rapid F diffusion is reported. This behavior suggests the formation of strongly bound F complexes, since *ab-initio* calculations

Table 3.1: Formation energies of single F configurations in reference to a F^+ interstitial in the bond-centered location with the Fermi level at the top of the valence band. Figure 3.4 shows the structure of the FV complex. Its formation energy is preferred by 0.59 eV over the symmetric substitutional configuration. E_F is the energy of the Fermi level, whereas E_V is the energy of the top of the valence band.

Structure	E_f [eV]
F^+_{bc}	$0.00 + (E_F - E_V)$
F^-_{tet}	$0.71 - (E_F - E_V)$
F^-_{hex}	$1.32 - (E_F - E_V)$
FV^+	$1.59 + (E_F - E_V)$
F^+_{sub}	$2.18 + (E_F - E_V)$

give a migration barrier of only 0.7-1.3 eV [22, 23], which indicates that single F atoms should be highly mobile well below 550 °C. The second part of the anomalous behavior is the shapes of the annealed profiles. Instead of broadening, the annealed profiles sharpen and shift toward the surface.

3.2 Ab-initio calculations to understand F behavior

To investigate fluorine behavior in silicon, the energies for various configurations were calculated using the DFT code VASP [61, 62] with the PW91 GGA functional [51] and ultrasoft Vanderbilt-type pseudo-potentials [63, 64]. All calculations were performed in a nominally 64 atom super-cell with periodic boundary conditions and 2^3 Monkhorst-Pack **k**-point sampling. A large energy cutoff of 320 eV was required due to the electronic properties of F. The structures were fully relaxed to a maximal force of less than 0.005 eV/Å per atom. The calculations were performed using the experimental Si lattice constant of $b = 5.43$ Å.

Figure 3.2 and Table 3.1 show the formation energy of various single F configura-

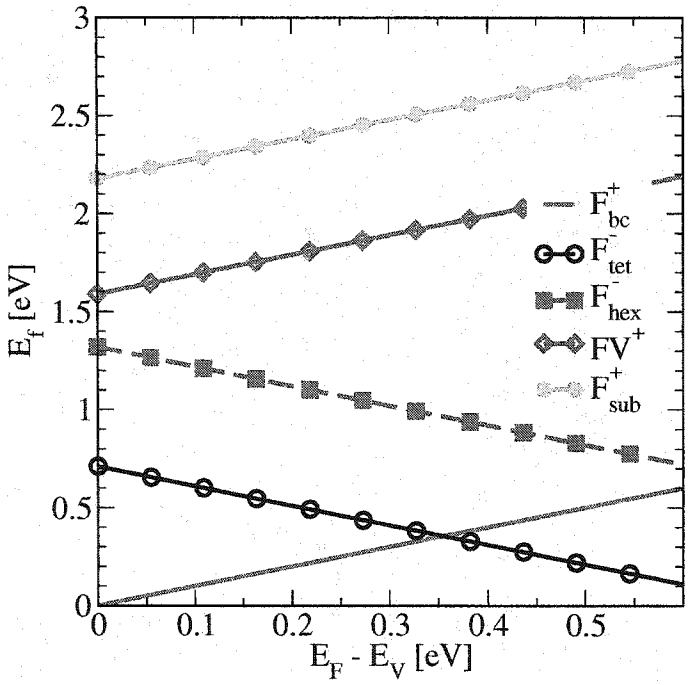

Figure 3.2: Fermi level dependence of various single F complexes. Our calculations show that there are no gap states for the shown complexes in the lower half of the band gap, which indicates that the listed charge states are the lowest energy states of a particular configuration for Fermi levels below midgap. For Fermi levels in the upper half of the band gap the formation energy and charge state depend on the exact location of the gap states, which can be expected to be subject to a correction that is some fraction of the DFT band gap error. All formation energies are in reference to F^+_{bc} with the Fermi level at the valence band edge and perfect Si. Table 3.1 lists the analytic results.

tions as a function of the Fermi level. The spatial configurations of these F complexes are shown in Appendix B. The analysis of the density of states (DOS) shows that none of the listed F complexes have states in the lower half of the Si band gap (see Appendix C). Therefore we conclude that a single F atom prefers to reside in a bond-centered (F^+_{bc}) interstitial site for $E_F \leq E_V + 0.36\,eV$. For higher Fermi levels the tetrahedral (F^-_{tet}) interstitial configuration is the ground state. The calculation of the formation energies of the other F complexes under such conditions is compli-

cated, since it involves the knowledge of the exact location of the gap states which are coupled to known drawback of DFT, a too small band gap.

In our analysis we used the DOS of charged and uncharged super-cell calculations to identify the gap states and the charge of a particular configuration as a function of the Fermi level. We verified our method of using uncharged super-cell results to predict formation energies of charged super-cells by comparing with actual charged super-cell calculations for all structures reported in Fig. 3.2 as well as F_3V (see Appendix D). In the case of F_{bc}^{+} the predicted value differs by only 0.003 eV. The error for F_{tet}^{-} is 0.07 eV, which is the largest difference found. These results suggest that in the case of the F_nV_m structures of interest, uncharged super-cell calculations can be used to identify gap states and the charge and energy of a particular configuration as a function of the Fermi level. The values reported in Fig. 3.2 are based on the actual charged super-cell calculations for accuracy. In a 64 atom super-cell with 2^3 Monkhorst-Pack **k**-point sampling, the valence band is taken at $\pi/(4b)(1,1,1)$ in the BZ, which has an energy of $\Delta E = 0.2845$ eV lower than the valence band maximum at the Γ point. The reported energies for negatively charged F configurations have been corrected accordingly. Figure 3.3 illustrates this fact. More details can be found in Appendix D.

The same reference structures were found by Taguchi *et al.* [23]. Previous DFT calculations show interstitial F to be highly mobile ($E^m_{F_{bc}} \leq 1.3$ eV [23], $E^m_{F_{tet}} = 0.7$ eV [22]). We also determined the migration path between different F configurations using the nudged elastic band (NEB) method [10]. In p-type material we found the lowest migration path to be $F_{bc}^{+} \rightarrow F_{tet}^{+} \rightarrow F_{bc}^{+}$, where F_{tet}^{+} is an intermediate metastable state of the two-step transition. The associated transition state F_{trans} is also positively charged. In contrast, for n-type material F_{tet}^{-} is the lowest single F energy configuration with a simple one-step migration path. The transition state is almost identical to F_{hex}^{-}. The migration energy between bond-centered sites is $E^m_{F_{bc}^{+}} = 1.38$ eV, whereas the migration barrier for $E^m_{F_{tet}^{-}}$ is 0.60 eV. These results agree

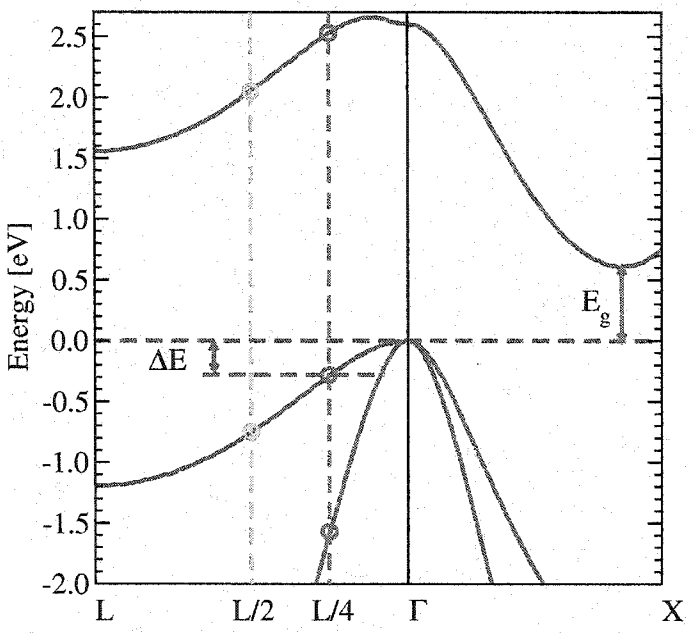

Figure 3.3: DFT result of the silicon band structure near the valence band maximum and conduction band minimum for a two atom cell. $L = \pi/b\,(1,1,1)$, $\Gamma = 2\pi/b\,(0,0,0)$, and $X = 2\pi/b\,(1,0,0)$ with $b = 5.43\,\text{Å}$ are the high symmetry points of the first Brillouin zone. The green (dashed) line indicates the valence band edge, whereas the blue arrow marks the silicon band gap. The orange dashed line indicates the **k**-points used in a 2^3 Monkhorst-Pack **k**-point sampling calculation with a cubic super-cell of size b (8 Si atom super-cell), whereas the blue dashed line indicates a super-cell of size $2b$ (64 Si atom super-cell). The above band structure was determined using DFT with a GGA functional. The energy difference between Γ and L of the top valence band is 1.19 eV, which agrees very well with various other theoretical (1.05-1.28 eV) and experimental (1.2 ± 0.2 eV) results [4]. DFT predicts the valence band structure of silicon very reliably, however due to well known underestimation of the band gap, predicting the energies of conduction band states is problematic.

well with previous work [23, 22]. In contrast to Taguchi *et al.* and Van de Walle *et al.*, who did not calculate the energy of the transition states to find the migration barriers for the different F diffusion paths, but only estimated the barriers by comparing different metastable F structures including their charge states, in our work, we used the nudged elastic band method to actually calculate the energy and structure of the

transition states. Therefore our results are a confirmation of the educated guesses by Taguchi *et al.* and Van de Walle *et al.*. For midgap Fermi levels, F diffusion will be dominated by F^{-}_{tet} due to both a lower formation and migration energy.

In addition to fluorine structures, interstitial (I) and vacancy (V) ground state energies were calculated as references. The calculated formation energies of neutral I (<110> split) and V are 3.78 eV and 3.38 eV respectively, consistent with previous work [46].

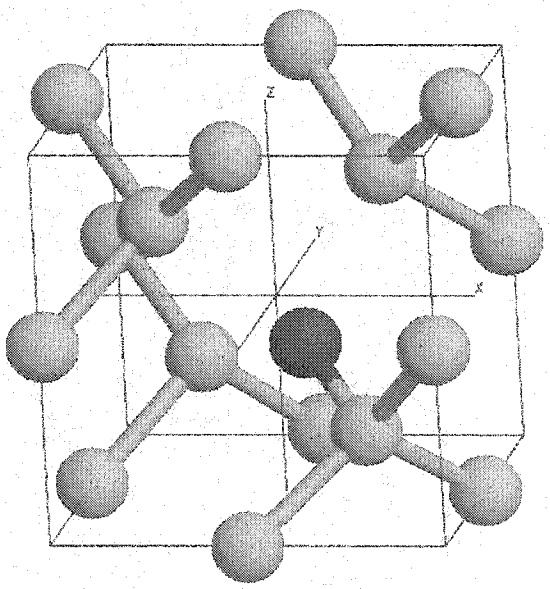

Figure 3.4: 3D view of a neutral single FV complex. The fluorine atom has moved toward one silicon atom out of the substitutional site. The Si–F bond length is 1.68 Å (71 % of the Si–Si bond length). The silicon atoms are drawn in amber (light), while the fluorine atom is presented in blue (dark).

We found F_nV_m structures to have a rather high binding energy, suggesting decoration of vacancies by fluorine. The passivation of Si dangling bonds by fluorine is known from surface studies [65]. For substitutional F, the F is shifted away from the

Table 3.2: Binding energies of F_nV_m configurations for $E_F = E_V + 0.45\,eV$ (intrinsic Fermi level at 650 °C [5]). For midgap Fermi level, the dominant clusters are charge neutral. The decreasing binding energy of the F_nV structures is attributed to the increasing crowding of the F atoms. This phenomenon is illustrated in Fig. 3.5. The total binding energies (third column) are calculated with respect to lowest energy interstitial fluorine configuration for the mentioned Fermi level (F^-_{tet}) and single vacancies (V^0). The binding energies in the second column are the energy change upon adding the final F to the structure. The fourth column lists the total formation energy, which includes the formation energy of the necessary vacancies.

Structure	E_b last F [eV]	E_b^{tot} [eV]	E_f [eV]
V	—	—	+3.38
FV	−1.95	−1.95	+1.43
F_2V	−1.80	−3.75	−0.37
F_3V	−1.51	−5.26	−1.88
F_4V	−0.10	−5.36	−1.98
V_2	—	−1.45	+5.31
FV_2	−2.31	−3.77	+3.00
F_2V_2	−2.43	−6.20	+0.57
F_3V_2	−1.78	−7.98	−1.21
F_4V_2	−1.76	−9.74	−2.98
F_5V_2	−1.59	−11.33	−4.57
F_6V_2	−1.13	−12.46	−5.69

lattice site toward one of the neighboring Si atoms (see Fig. 3.4), which indicates that this structure is more accurately considered an F interstitial decorating a vacancy (FV). In Table 3.2, the formation and binding energies for different F_nV_m configurations are listed. Here the reference point for the total binding energy is negatively charged tetrahedral fluorine (F^-_{tet}) and single neutral vacancies. The Fermi level was assumed to be the intrinsic Fermi level at 650 °C ($E_F = E_V + 0.45\,eV$ [5]).

The formation energy of FV was used to estimate the errors arising from the finite energy cutoff, cell-size, and **k**-point sampling. Increasing the cutoff to 450 eV resulted in a change in formation energy on the order of 0.02 eV. Changing the cell-size to a 216 atom super-cell while leaving the cutoff and **k**-point sampling unchanged led to a change in energy of 0.13 eV. We also increased the **k**-point sampling from 2^3 to 4^3 using the 64 atom super-cell with a 500 eV cutoff. The resulting change in formation energy was 0.025 eV.

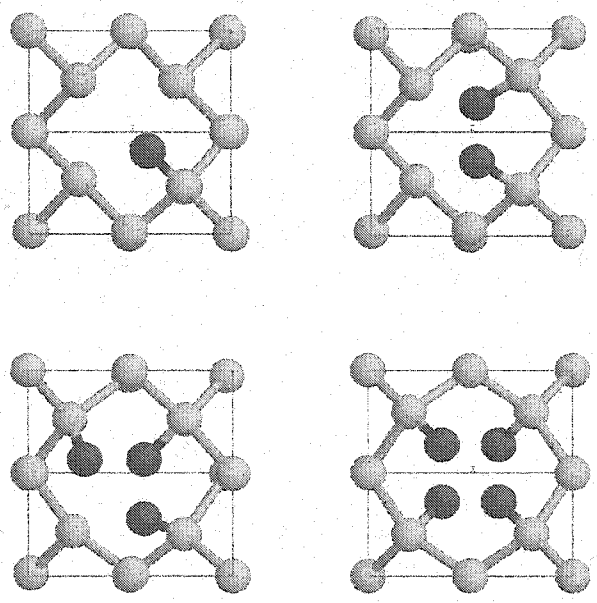

Figure 3.5: View down the $\langle 100 \rangle$ direction (see Fig. 3.4) of the four neutral F_nV structures. An increasing distortion of the surrounding silicon lattice is observed when adding more fluorine atoms. This is due to the repulsion of the F atoms, which becomes particularly apparent by comparing FV with the other clusters. Simultaneously the Si–F bond length is reduced from 1.68 Å in FV to 1.57 Å in F_4V.

For two or more F atoms, F_nV_m structures are favored over the interstitial configuration. For F_nV structures, the binding energy gained by adding additional fluorine

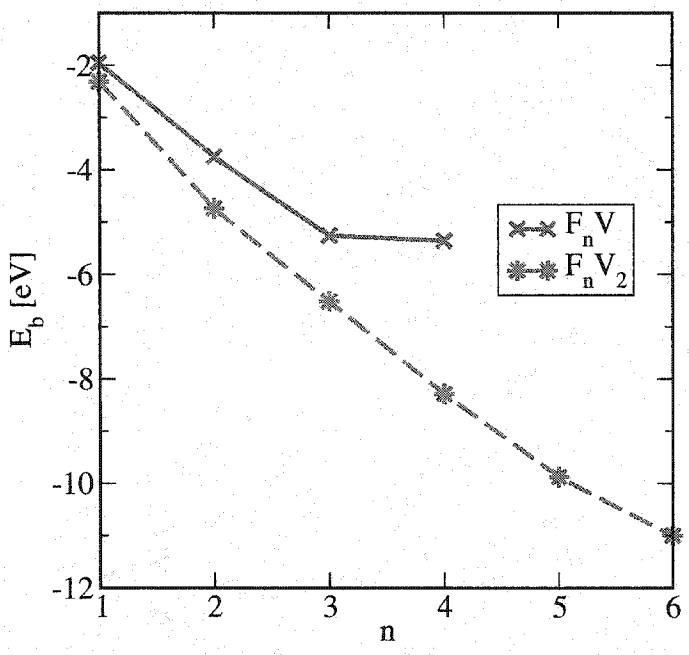

Figure 3.6: Binding energies of F_nV and F_nV_2 configurations for $E_F = E_V + 0.45\,eV$ (intrinsic Fermi level at 650 °C [5]) in reference to V and V_2 respectively. Table 3.2 lists the numerical values.

atoms decreases. This behavior is due to the increasing space requirements of the decorating fluorine atoms. This becomes particularly apparent by comparing F_2V with F_3V in Fig. 3.5. Three fluorine atoms in F_3V are pushed away from each other and a distortion of the surrounding silicon lattice is noticeable. The rather large drop in marginal binding energy between F_3V and F_4V from 1.51 eV to 0.10 eV (see Fig. 3.6) can be explained with the same argument, since F_4V shows an increasing distortion of the lattice and reduction of the Si–F bond length (see Fig. 3.5).

We also investigated F_nV_2 structures, which show a similar reduction in binding energy with n, but no sharp drop-off, since more space is available to accommodate F atoms at all six dangling bonds. In Fig. 3.7, the estimated equilibrium concentrations at 650 °C of F structures versus total F concentration are shown (changes in formation entropy are neglected). In the presence of non-equilibrium point-defect

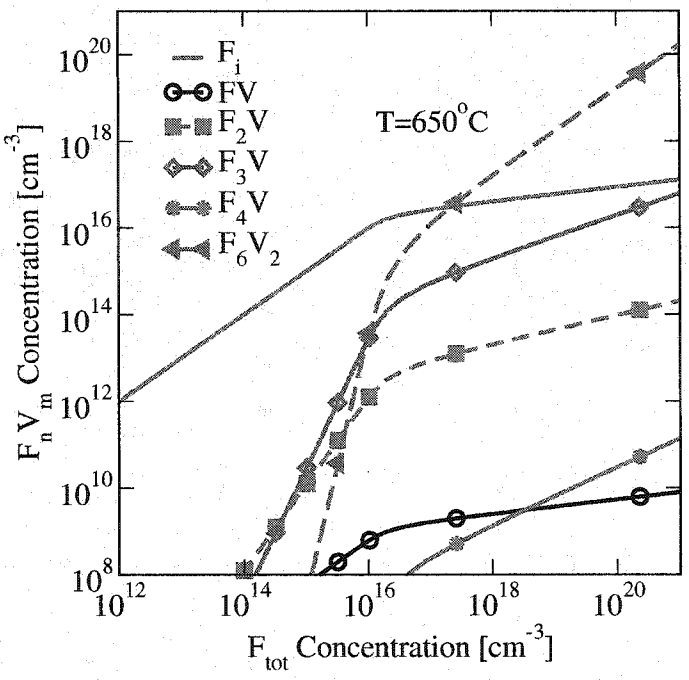

Figure 3.7: Equilibrium concentration of various F_nV_m structures vs. total F concentration at 650 °C. The Fermi level is assumed to be at midgap (0.45 eV above the valence band edge [5]). For low $C_{F_{tot}}$ the dominant species is F_i due to the entropy of mixing. At high $C_{F_{tot}}$ the major F contribution comes from F_6V_2 clusters. The vacancy formation energy is included in these calculations.

concentrations, the local equilibrium F_nV_m concentrations need to be multiplied by $(C_V/C_V^*)^m$. Thus, in the presence of excess vacancies during the initial stages of implant annealing, almost all fluorine will reside in F_nV_m structures. The evolution of F_nV_m clusters is particularly important during implant anneals due to the high point-defect concentrations.

The saturated F_6V_2 structure shows another interesting property: it is almost stable in the presence of interstitials. Table 3.3 lists the energy change associated with I reactions with F_nV_m structures. Migration and/or reaction barriers, which might further stabilize F_nV_m structures, are not included. Due to the strong binding of the fluorine atoms with the silicon atoms surrounding vacancies, we believe these

Table 3.3: Stability of the F_nV_m cluster in the presence of I. ΔE is defined as $E_f^{F_nV_m} + E_f^{I} - E_f^{rhs}$. Our calculations find that the fully saturated F_6V_2 structure is almost stable even at high I concentrations. This calculation does not include possible migration/reaction barriers, which further stabilize F_nV_m structures.

$F_nV + I \Leftrightarrow n\ F_i$	ΔE [eV]
$n = 1$	+5.21
$n = 2$	+3.41
$n = 3$	+1.90
$n = 4$	+1.80
$F_nV_2 + I \Leftrightarrow F_4V + (n-4)\ F_i$	ΔE [eV]
$n = 4$	+2.78
$n = 5$	+1.19
$n = 6$	+0.07

defects to be immobile.

All F_nV_m calculations were performed with uncharged super-cells. The dependences of the formation energies on the Fermi level were extracted from the DOS (see Appendix C). For midgap Fermi levels, the dominant clusters (F_nV and F_6V_2) are all uncharged. Table 3.2 lists the formation energies under those conditions. The analysis for incompletely F decorated F_nV_2 clusters is very complicated since they have many gap states, which are introduced by the divacancy V_2.

We also investigated pairing of F_i with I and F_i. DFT predicts interstitial F_2 to be unbound, as the fluorine prefers to remain in an interstitial site rather than forming an F_2 bound state. F_i binds to I with an energy of 0.46 eV. This number was deduced by comparing FI to F_i and I separated within the same super-cell.

A recent study by Pi *et al.* [66] using positron-annihilation, SIMS, and XTEM concludes (in agreement with our calculations) that F forms F_nV_m complexes by dec-

orating the dangling bonds of vacancy clusters. They also observe that F retards I-V recombination, which is a direct conclusion of our calculations. Pi *et al.* analyzed the initial stages of F redistribution and attributed the observed behavior to a F vacancy diffusion mechanism with an activation energy of 2.19 eV. Based on our *ab-initio* calculations, we predict a similar activation energy for fluorine migration. However, we attribute the redistribution of F to release and diffusion of F interstitials rather than diffusion of FV complexes. The binding energy for the last F atom added to a F_6V_2 cluster is -1.13 eV, which can be combined with the calculated F_i migration barrier of 0.60 eV to give a predicted activation energy for F migration of 1.73 eV.

3.3 Continuum modeling of F diffusion

We used the results of the previously discussed *ab-initio* calculations, which suggest a distinct diffusion mechanism involving F_nV_m clusters, to model fluorine diffusion in the continuum limit. In the Si phase we implemented fluorine decoration of V and V_2. All energetically favorable reactions are treated as diffusion limited and we considered only I, V, and F_i to be mobile in the Si phase. The associated formation and dissociation reactions are:

$$\begin{aligned} F_nV_m + F_i &\Leftrightarrow F_{n+1}V_m, \\ F_i + I &\Leftrightarrow FI, \\ F_nV + I &\Leftrightarrow n\,F_i, \\ F_nV_2 + I &\Leftrightarrow F_4V + (n-4)\,F_i, \\ FI + V &\Leftrightarrow F_i. \end{aligned} \tag{3.1}$$

In addition, extended defect models, including I_n and V_n clusters up to size $n = 10$ plus {311} defects, are used [6]. The extended defect models are crucial for the correct temperature behavior. To match the experimental set up, a thin oxide surface layer of $d = 20$ Å is included in the simulation. Figure 3.8 shows the schematic

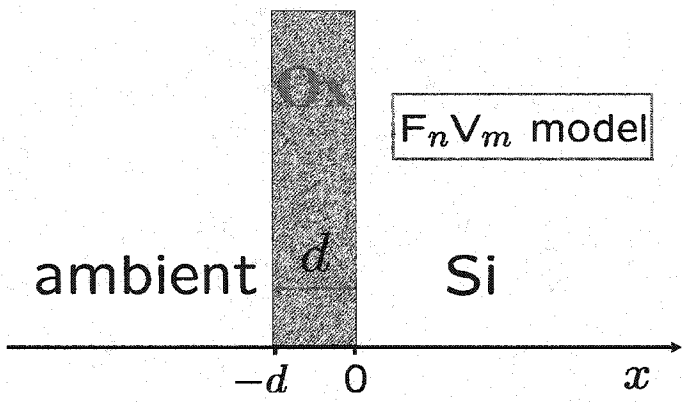

Figure 3.8: Schematic layout of the different regions considered in the simulation to model the anomalous F diffusion reported by Jeng *et al.* [3].

layout of the different regions considered. In the graph the ambient phase is only added for completeness, since the ambient/SiO_2 interface is modeled as a perfect sink for F. In the SiO_2 phase only F is considered and modeled with a simple diffusion model. The F concentration $C_{\mathrm{F}}^{\mathrm{SiO_2}}$ at the Si/SiO_2 interface is determined by the experimental reported F segregation coefficient $m_{\mathrm{Si/SiO_2}} = C_{\mathrm{F}}^{\mathrm{SiO_2}}/C_{\mathrm{F}_i}^{\mathrm{Si}}$ [20]. The model parameters besides the formation energies of the F_nV_m cluster, which were reported in the previous section, are shown in Table 3.4.

Figure 3.9 shows the simulation results compared to the experimental data. Qualitatively the correct F behavior is observed, however the simulations show a somewhat stronger temperature dependence than observed experimentally. At 550 °C, no significant movement is predicted, while at 850 °C, F is entirely removed from silicon. A possible reason for the shortcomings at 550 °C might be the fact that the model does not include mobile I_2, which are predicted by *ab-initio* calculations [67]. We expect I_2 to change the profiles especially in the I-rich tail regions, where mobile I_2 will annihilate V_n clusters, reducing F decoration. The discrepancy at higher T may be due to the fact that we only include V and V_2 decoration. The *ab-initio* calculations suggest that a complete model need to include also the decoration of larger

Table 3.4: The diffusivities and the segregation coefficient are assumed to have Arrhenius dependences (e.g. $D = D_0 \exp(-E_m/kT)$). The values for the fluorine diffusivity in Si are based on *ab-initio* calculations assuming a purely interstitial migration mechanism. The fluorine diffusivity in SiO_2 was chosen to match the experimental results [3]. The segregation coefficient of fluorine at the Si/SiO_2 interface is extracted from experimental measurements [20]. We assumed $m_0 = 1$ since we do not have a basis to predict a significant entropy difference for (interstitial) fluorine in the two phases.

F diffusivity	D_0 [cm^2/s]	E_m [eV]
D_{Si}	0.040	0.9
D_{SiO_2}	0.025	2.7
F segregation	m_0	E_{seg} [eV]
m_{Si/SiO_2}	1	0.95

V_n clusters, since large binding energies are anticipated. Larger more stable F_nV_m clusters can be expected to remain in the V-rich region near the surface. The F signal near the surface might be also due to knock-ons from F segregation to the Si/SiO_2 interface on oxide film. The presented model is highly sensitive to the initial F implant damage and since predicting the latter one is extremely complicated due to the lack of a direct way to measure implant damage, we believe that the uncertainty in the initial damage profiles is a significant additional source of error for the quantitative mismatch between experimental measurement and simulation. We used the Monte Carlo implant simulator UT-Marlowe 6.0 and kinetic damage accumulation model to predict the initial damage.

3.4 Summary and conclusion

In conclusion, *ab-initio* calculations predict strongly bound F_nV_m clusters. No other comparably stable structures were identified; the binding energy found for FI clusters is significantly smaller. This DFT data can be used to identify the diffusion mecha-

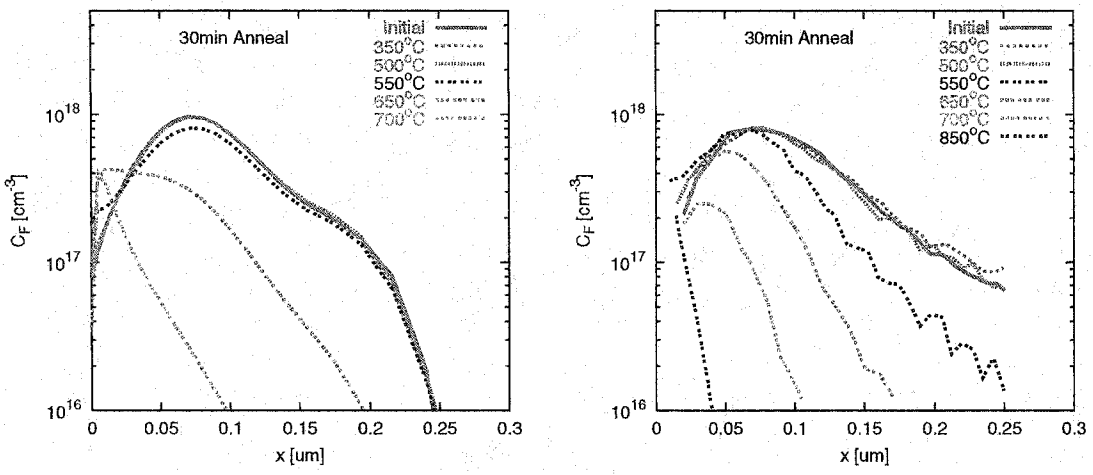

Figure 3.9: Comparison of simulation (left) with experimental data [3] (right) for $10^{13}\,\mathrm{cm}^{-2}$ 30 keV F^+ implant annealed for 30 min at various temperatures. The simulation includes F_nV, F_nV_2, and FI clusters in addition to an extended defect model [6]. The initial defect/fluorine profiles were obtained with Monte Carlo implant simulator UT-Marlowe 6.0 and kinetic damage accumulation model.

nism and explain the anomalous fluorine behavior reported by Jeng *et al.* [3]. Fast diffusing F_i decorate V_n forming immobile F_nV_m clusters. At higher temperatures, these clusters are annihilated by I. Figure 3.10 shows the as-implanted F and point-defect profiles. F decoration of V leads to F dissolving from deeper regions (I excess) and accumulation near surface (V excess).

Due to the strong affinity of F for V, in pre-amorphized samples we expect incorporation of F_nV_m clusters during regrowth. The consequences for boron diffusion in such an environment would be TED reduction and activation for amorphizing conditions due to excess V. However, in the case of non-amorphizing implants we expect an increased I concentration due to the formation of F_nV_m clusters, which leads to an enhancement of TED. These predictions for amorphizing conditions are supported by experimental data [56, 58, 59] as discussed in Chapter 4.

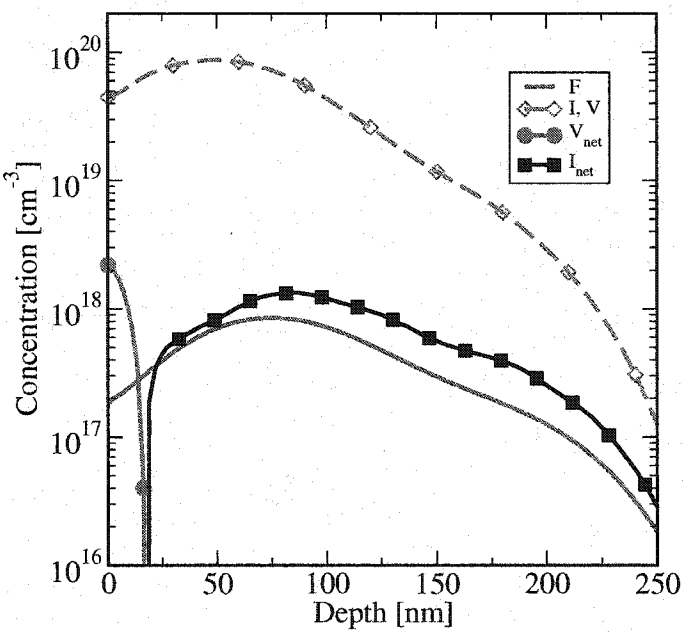

Figure 3.10: As-implanted fluorine and defect profiles of a $10^{13}\,\mathrm{cm}^{-2}$ 30 keV F implant using MC implant simulator UT-Marlowe [7].

Chapter 4

FLUORINE CO-IMPLANTATION EFFECTS ON DOPANT REDISTRIBUTION

In the previous chapter the anomalous fluorine diffusion behavior was explained based on *ab-initio* calculations. Using an extensive multi-cluster model, the fluorine redistribution behavior was modeled successfully. Technologically, F is not of interest to ULSI technology as a dopant due to its low solubility and high diffusivity. However, F has been shown to have beneficial properties as a co-implant. Depending on the process conditions, there is experimental evidence that F reduces B and P transient enhanced diffusion (TED) [56, 57, 58, 59, 60], as well as enhances B activation [56, 57]. However, to utilize these benefits effectively, a fundamental understanding of the F dopant interaction is necessary, particularly since not only has implanted F been observed to behave unusually in silicon, manifesting an apparent uphill diffusion [3], but also, depending on the implant conditions, F has been shown to enhance rather than retard B diffusion under some conditions (see Fig. 4.8). This chapter focuses on the effects of co-implanted F on dopant redistribution. The previously discussed F diffusion model is used to develop a comprehensive model to analyze and explain the effects of co-implanted F on B and P redistribution under various implant conditions. Of particular interest is understanding the difference between sub-amorphizing and amorphizing conditions on the effects of co-implanted fluorine on boron and phosphorus.

4.1 *Simplified fluorine model*

Theoretically, F can affect B and P diffusion in at least two distinct ways. A direct interaction could explain the reported F effects if there is a large binding energy between dopant and F atoms. The second possibility is an indirect interaction. If F interacts strongly with point-defects, it alters the local point-defect concentrations, changing the point-defect mediated diffusion behavior of B and P. *Ab-initio* calculations find only about 1 eV binding for dopant-fluorine complexes (B-F and P-F), which is insufficient to significantly influence diffusion behavior [68]. In contrast, strongly bound fluorine vacancy clusters (F_nV_m) are identified (see Chapter 3). This suggests that the effects of F on B and P are primarily due to fluorine point-defect interactions. In this case, it is expected that once the anomalous F diffusion is understood, the same model should also explain the effects on B and P.

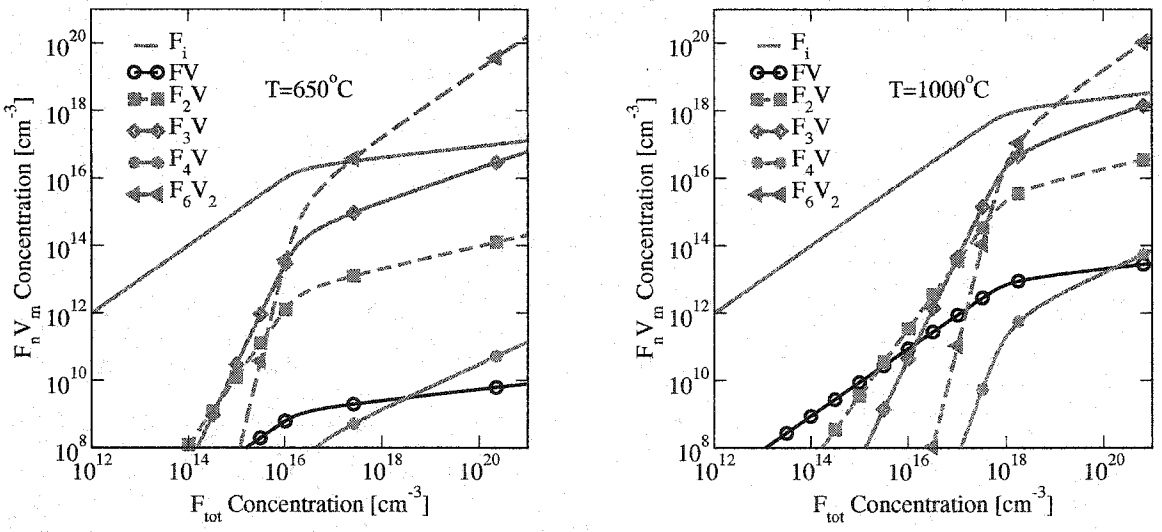

Figure 4.1: Predicted F_nV_m concentration vs. total F concentration in local equilibrium at 650 °C (left) and 1000 °C (right).

In the previous chapter, a multi-cluster continuum model was developed that considered formation of various F_nV_m cluster configurations based on *ab-initio* calcula-

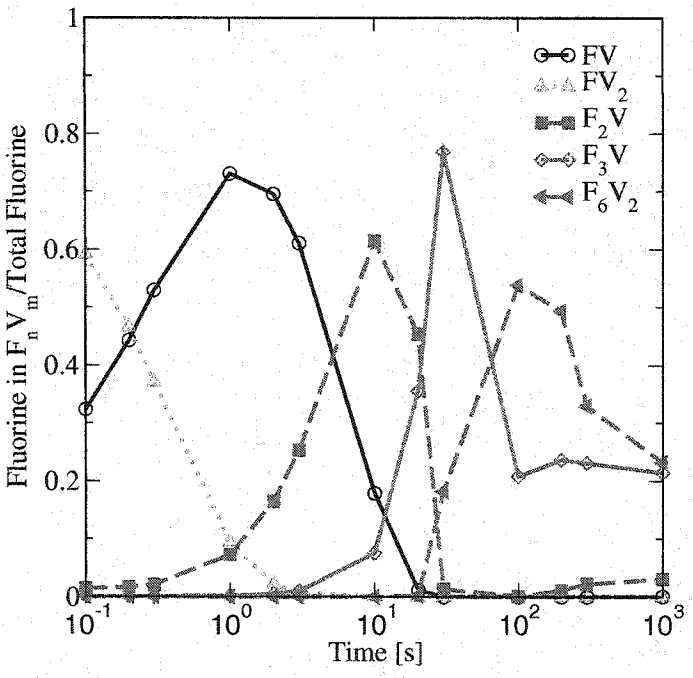

Figure 4.2: Simulated fluorine dose (depth integrated concentration) versus time during a 30 min anneal at 650 °C after a $10^{13}\,\mathrm{cm}^{-2}$ 30 keV F^+ implant. The model used is described in detail in Chapter 3. Only the most significant F_nV_m clusters are shown here. The time evolution can be split into two phases; phase 1: formation of F_3V and F_6V_2, phase 2: dissolution of F_3V and F_6V_2.

tions. The model, which considered a large set of F_nV_m clusters and their associated reaction pathways, successfully explained the anomalous fluorine diffusion behavior in silicon. In this chapter, we further analyze this model to derive a simpler form of the fluorine model.

Figure 4.1 shows the local equilibrium concentrations of different F_nV_m as a function of total F concentration at 650 °C and 1000 °C. The dominant clusters are F_3V and F_6V_2. For total F concentrations above $10^{16}\,\mathrm{cm}^{-3}$ (650 °C) and $10^{18}\,\mathrm{cm}^{-3}$ (1000 °C) respectively the dominant clusters are F_3V and F_6V_2. Figure 4.2 illustrates the time evolution of the dominant F_nV_m clusters using the multi-cluster model during a 30 min anneal at 650 °C under sub-amorphous conditions. This time evolution

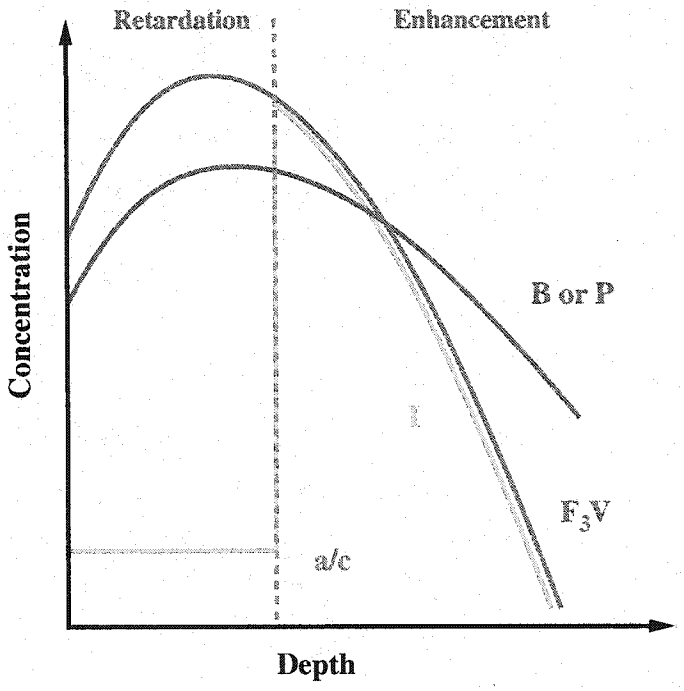

Figure 4.3: This diagram illustrates the mechanism by which F impacts B and P diffusion. The depth of the amorphous-crystalline interface (dashed green line) and the implant depth of fluorine are the key parameters. In the non-amorphized regions, B and P diffusion get enhanced due to excess interstitials I, while in amorphized regions, diffusion is retarded due to grown-in F_3V.

can be split into two phases: formation of F_3V and F_6V_2, and dissolution of F_3V and F_6V_2. Since the first phase is very brief (20 s at 650 °C, 0.5 ms at 1000 °C), we can focus only on the dissolution of the clusters. Since both clusters have the same F:V ratio, they have similar effects on point-defect concentration. Thus we utilize a simplified model, which includes only a single cluster, F_3V. The fluorine effects are modeled via a single cluster dissolution reaction:

$$F_3V + I \Leftrightarrow 3F_i. \tag{4.1}$$

In the model, the complete F dose is initialized as F_3V (3 interstitial F atoms decorating a vacancy). That effectively introduces +2/3 I for every F atom (three

I minus one V divided by three F). Since we expect implanted F to be interstitial fluorine F_i (+1 I model), we correct by adding the missing +1/3 I separately. This treatment is also applicable in the amorphous region, where we assume that F_nV_m clusters are grown in during the regrowth process since this minimizes the free energy of the regrown region.

Figure 4.3 illustrates the interaction mechanism of F on B and P via local point-defect concentration modifications. The diagram shows schematically F, dopant, and interstitial profiles after regrowth. In the amorphous region (left of a/c interface), vacancies (V) are grown in as F_3V clusters, which leads to TED reduction of B and P. In regions which are not amorphized, F enhances dopant diffusion due to the excess +1/3 I. This treatment enables the model to predict the fluorine effect on B and P in cases where the dopant concentration is divided by the amorphous-crystalline interface. The depth of the amorphous-crystalline interface and the implant depth of fluorine become the key parameters to understand the effect of fluorine on B and P.

The F behavior in SiO_2 (screen oxides) and at the Si/SiO_2 interfaces is treated like in the previous chapter via simple diffusion and segregation.

4.2 Application of simplified F model

The model introduced in the previous section was implemented and compared to experimental data for a range of conditions. In the next section, it is shown that the simple model reproduces the experimentally observed anomalous F diffusion behavior. Afterwards the impact of F on P and B is compared for two different experimental conditions: high energy/high dose implants (source/drain conditions) and high energy/low dose implants (halo conditions). The results are shown in Sections 4.2.2 and 4.2.3 for P and B respectively.

4.2.1 Anomalous F behavior

Figure 4.4 shows the profiles of 20 keV 3×10^{15} cm^{-2} F as-implanted and after a 1050 °C spike anneal [17] in the absence of other dopants. The implantation was performed through a 10 nm screen oxide. The model predicts correctly the characteristic anomalous fluorine diffusion behavior. The SIMS data suggests the amorphous-crystalline (a/c) interface to be at 36 nm, visible through the F accumulation at the end-of-range (EOR), whereas the simulation data indicates an a/c depth of 55 nm. In all subsequent graphs the simulation value of the a/c depth is indicated for profile prediction. The trapping of F in the pre-amorphized region strongly supports the assumption of formation of F_nV_m clusters in the amorphized region during regrowth.

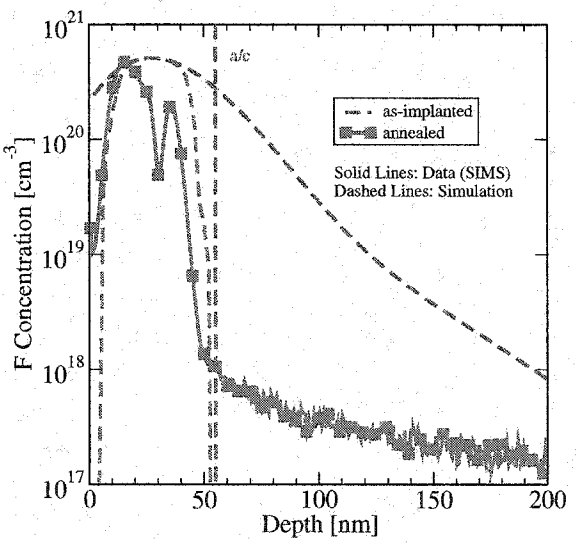

Figure 4.4: Measured and predicted concentration profiles of 20 keV 3×10^{15} cm^{-2} F before and after a 1050 °C spike anneal in the absence of other dopants. The SIMS data was provided by Texas Instruments Inc. [8].

4.2.2 F effects on P

Figures 4.5 and 4.6 show the effect of F on P diffusion. In Fig. 4.5 (source/drain condition) an arsenic pre-amorphized sample was implanted with $4 \times 10^{15}\,\mathrm{cm}^{-2}$ P. The effect of F is investigated via $2 \times 10^{15}\,\mathrm{cm}^{-2}$ F implants at 10 keV and 30 keV and a 1050 °C spike anneal. In all cases, most of the P dose is located within the pre-amorphized region. The a/c interface from MC simulations is at 55 nm for no F and 10 keV F implant. The P diffusion retardation effect due to co-implanted F is correctly predicted by the model (line with open circles). For the 30 keV F implant, the a/c interface moves to 90 nm. The model predicts an increased retardation effect due to the deeper pre-amorphized region, which is confirmed by the experimental data (line with filled squares). Under all conditions, the simulation data matches the SIMS data well. F retards the P diffusion since most of the P dose is initially located within the pre-amorphized region.

Figure 4.6 shows SIMS data of a Sb/BF_2 pre-amorphized sample including a 40 keV $9 \times 10^{13}\,\mathrm{cm}^{-2}$ P implant (halo condition). The effect of F is investigated via a 20 keV $10^{15}\,\mathrm{cm}^{-2}$ F implant followed by 950 °C and 1050 °C spike anneals. The a/c interface is located at 55 nm. The SIMS data shows a retardation of the P diffusion in the presence of F. This behavior is again matched well by the model. The retardation effect takes place primarily in the sub-amorphous region, but since the a/c interface is close to the tail of the P profile this is anticipated by the model. The experimental data as well as the simulation results show a shift in the peak location of the P profile due to coupling with the shallow B profile ($x_j \approx 30\,\mathrm{nm}$). In the presence of F, the P peak movement toward the surface is retarded.

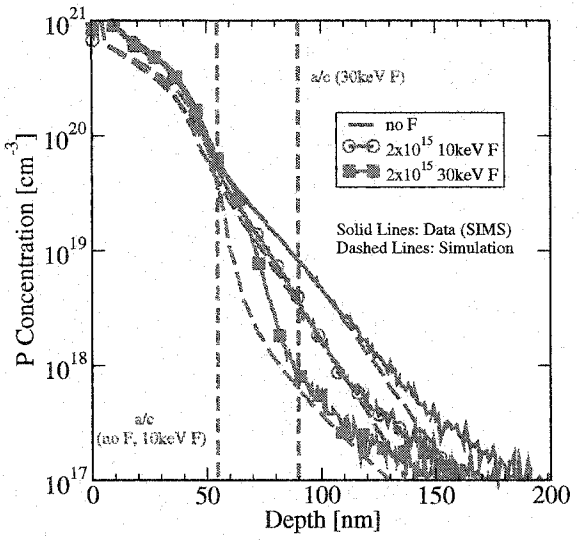

Figure 4.5: Arsenic pre-amorphized sample with a $4 \times 10^{15}\,\mathrm{cm}^{-2}$ P implant. The effect of F is investigated via $2 \times 10^{15}\,\mathrm{cm}^{-2}$ F implants at 10 keV and 30 keV and a 1050 °C spike anneal. The SIMS data was provided by Texas Instruments Inc. [8].

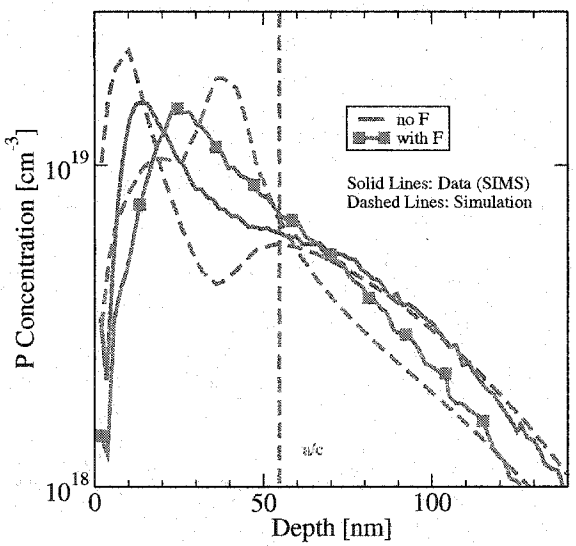

Figure 4.6: Sb/BF_2 pre-amorphized sample including a 40 keV $9 \times 10^{13}\,\mathrm{cm}^{-2}$ P implant. The effect of F is investigated via a 20 keV $10^{15}\,\mathrm{cm}^{-2}$ F implant followed by 950 °C and 1050 °C spike anneals. The SIMS data was provided by Texas Instruments Inc. [8].

4.2.3 F effects on B

Figures 4.7 and 4.8 show B data under similar implant conditions to Figs. 4.5 and 4.6 for P. In the Fig. 4.7 a dose of $3 \times 10^{15}\,\mathrm{cm}^{-2}$ B is implanted (source/drain condition) and the effect of F is investigated via a 10 keV $2 \times 10^{15}\,\mathrm{cm}^{-2}$ F implant and a 1050 °C spike anneal. The a/c interface is located at 60 nm. The B profile is slightly retarded in the presence of F as predicted by the simulation.

Figure 4.8 shows a shallow As pre-amorphized sample including a 10 keV $6 \times 10^{13}\,\mathrm{cm}^{-2}$ B implant (halo condition). The effect of F is investigated via a 10 keV $10^{15}\,\mathrm{cm}^{-2}$ F implant followed by 950 °C and 1050 °C spike anneals. The a/c interface is located at 28 nm. The SIMS data shows an enhancement of the B diffusion in the tail region of the profile in the presence of F, which is matched well by the simulated data. Since there is only shallow pre-amorphization, this behavior is anticipated by the underlying model.

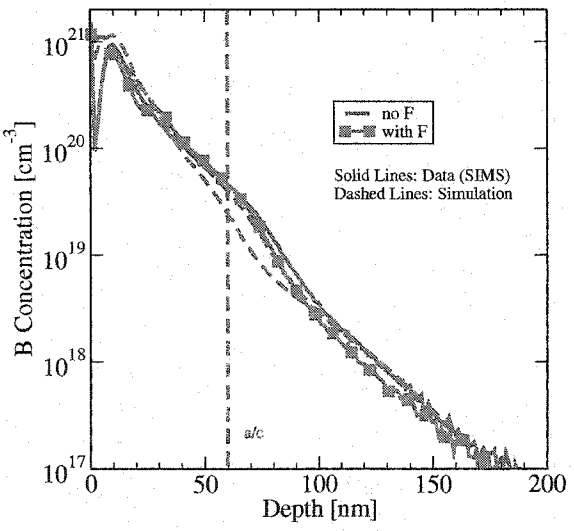

Figure 4.7: A dose of $3 \times 10^{15}\,\mathrm{cm}^{-2}$ B is implanted and the effect of F is investigated via a 10 keV $2 \times 10^{15}\,\mathrm{cm}^{-2}$ F implant and a 1050 °C spike anneal. The SIMS data was provided by Texas Instruments Inc. [8].

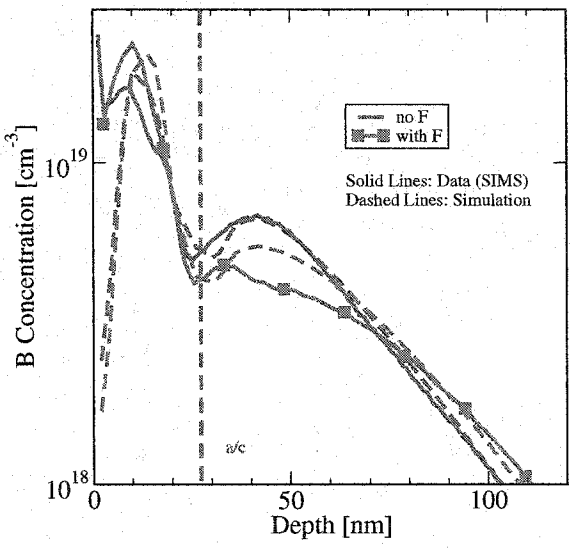

Figure 4.8: Shallow arsenic pre-amorphized sample including a 10 keV 6×10^{13} cm^{-2} B implant. The effect of F is investigated via a 10 keV 10^{15} cm^{-2} F implant followed by 950 °C and 1050 °C spike anneals. The SIMS data was provided by Texas Instruments Inc. [8].

4.3 Summary and conclusion

In summary, a simple model that incorporates the essential physics from *ab-initio* calculations was developed. This model predicts the effect of fluorine on boron and phosphorus diffusion under a range of experimental conditions. The behavior is predicted correctly in all cases, but there is a trend to overestimate the retardation effect seen in experimental data. This may be due to simulated a/c interface depths being deeper than the actual values as suggested by Fig. 4.4.

This analysis predicts the F effect on B and P to be entirely due to interactions of F with point-defects. Fluorine alters the local point-defect concentration due to the formation and dissolution of energetically favored F_nV_m clusters and therefore indirectly impacts the point-defect mediated diffusion behavior of B and P. The depth of the amorphous-crystalline interface and the implant depth of fluorine are the key pa-

rameters to understand the effects on dopant redistribution. Under sub-amorphizing conditions, B and P diffusion are enhanced due to increased I concentrations, in contrast to amorphized regions where the model predicts retarded diffusion due to the additional vacancies grown in originally as F_3V.

Chapter 5

STRESS EFFECT ON POINT-DEFECT EQUILIBRIUM

In current ULSI technology, stress effects become more important as steep doping gradients and hetero-interfaces induce stress gradients and reduced dimensions make any variation in diffusivity critical. On top of this, stress is sometimes induced purposefully to enhance carrier mobility [69, 70, 71]. Since experiments are difficult, and in the case of boron diffusion lead to contradictory results [72], we utilize *ab-initio* calculations to predict stress effects on the formation and migration of point-defects, which control dopant diffusion as well as dopant activation. In contrast to previous work, our analysis extends beyond simple hydrostatic activation volumes [25, 27] to enable prediction of anisotropies associated with more complex stress states (e.g., differences between in-plane and perpendicular diffusion under biaxial strain). We determined both strain tensors as well as changes in elastic constants due to defects and migration saddle points (see Chapter 6).

First, a general methodology to treat stress/strain effects on formation and migration energies using *ab-initio* methods is introduced and tested by calculating the elastic properties of defect-free silicon. Afterwards the same methodology is applied to various point-defect configurations to predict the changes in equilibrium point-defect concentration C_I^* and C_V^* for arbitrary stress/strain states. As mentioned above, C_I^* and C_V^* are critical parameters for phenomena like boron transient enhanced diffusion (TED) and boron activation. In the following chapter the methodology is extended to also treat the effects of stress on point-defect and dopant diffusion.

5.1 Methodology

The objective of this section is to develop a consistent framework for treating stress effects on formation and migration energies of defects in Si. In the linear elastic limit, the elastic constants $C_{\alpha\beta}$ of a given material relate a stress/strain state to its energy:

$$E(\epsilon_\alpha) = E_0 + \frac{\Omega}{2}\sum_\alpha \epsilon_\alpha \sigma_\alpha = E_0 + \frac{\Omega}{2}\sum_{\alpha,\beta} \epsilon_\alpha C_{\alpha\beta}\epsilon_\beta, \tag{5.1}$$

where Ω is the volume of a sample of the material and $\sigma_\alpha/\epsilon_\alpha$ denotes a specific stress/strain state. We use the definitions used in Ref. [73] for α and β ($\alpha, \beta \in \{1, \ldots, 6\}$). Strain and stress are related in the elastic regime through Hooke's law: $\sigma_\alpha = \sum_\beta C_{\alpha\beta}\epsilon_\beta$. Thus, once the elastic constants and induced strain for a given equilibrium structure or transition state are known, the change in formation energy E_f and migration energy E_m can be calculated, which leads directly to modified equilibrium concentrations and diffusivities. The remainder of this section focuses on deriving these relations in more detail.

In contrast to experiments, where it is often easier to control a given stress state, theoretically strain is the simpler concept, since it does not involve the knowledge of the elastic constants $C_{\alpha\beta}$ of the material. A strain ϵ is always well defined once a reference lattice constant b_0 is specified:

$$\epsilon = \frac{b - b_0}{b_0}, \tag{5.2}$$

where b is the lattice constant of the strained material. Figure 5.1 shows a cubic 8 Si atom super-cell with the lattice dimensions b_x, b_y, and b_z. By varying the lattice constants from their equilibrium value, arbitrary strain states can be simulated. Using *ab-initio* techniques the energy of such strained super-cells can be computed. By combining the results the equilibrium lattice constants as well as the elastic constants $C_{\alpha\beta}$ of a material can be extracted. Figure 5.2 shows a typical result of such a calculation. Shown is the change of the total energy of a 64 Si atom super-cell as a

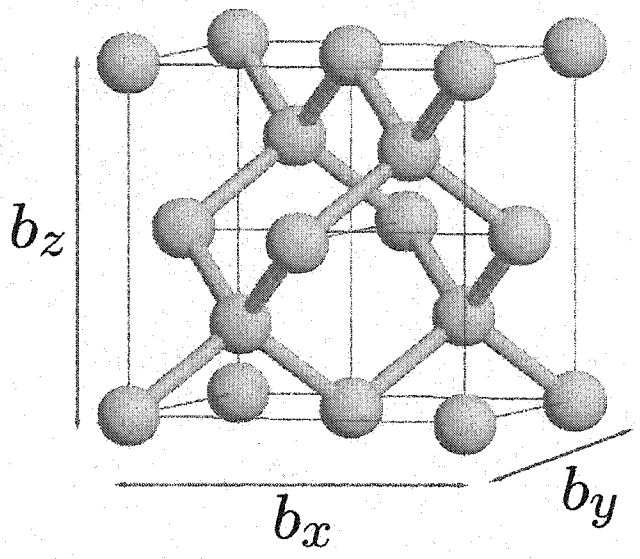

Figure 5.1: Cubic 8 silicon atom super-cell with lattice dimensions b_x, b_y, and b_z as indicated. Arbitrary strain states can be simulated by varying the lattice dimension in the different directions.

function of lattice constant (hydrostatic strain, $b_x = b_y = b_z$). The bulk modulus of Si is directly related to the curvature of the graph (see Appendix E). Also the equilibrium lattice constant can be determined using the shown data, since the structure minimizes its energy at the equilibrium lattice constant.

The primary goal of this analysis is to determine the stress/strain effect on formation and migration energies of defects in a host material (in this case Si). In solid state physics, a macroscopic solid is usually approximated by a finite sized super-cell of volume Ω and periodic boundary conditions to model the effectively infinite crystal structure of the material. If properties of defects are calculated using this approach, the finite super-cell volume implies that the calculation is performed at a finite fixed defect concentration. Usually the defect concentration is expressed as a fraction of the

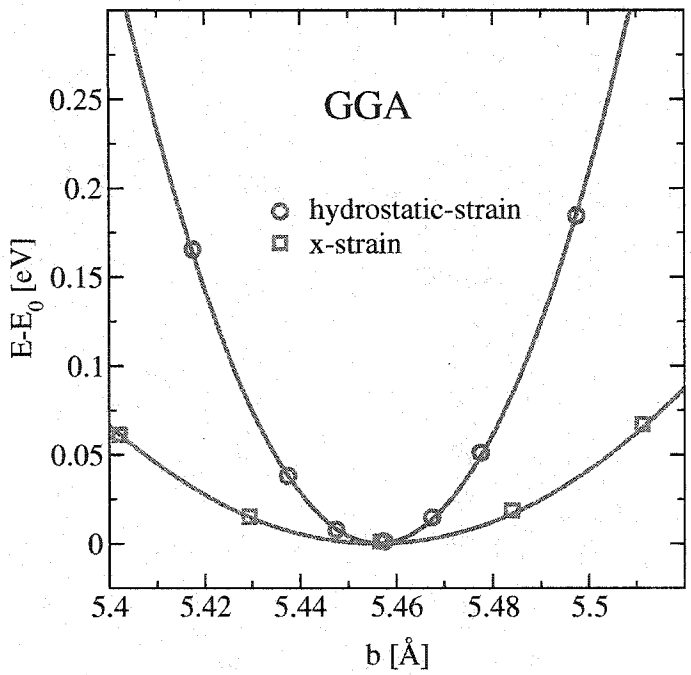

Figure 5.2: Energy vs. lattice constant b for Si under hydrostatic (red line) and uniaxial strain (blue line). The shown uniaxial strain data does not include any compensation effects due to Poisson's ratio. All energies are reported with respect to their minimum energy strain condition (unstrained Si). The data shown corresponds to a 64 Si atom super-cell GGA calculation.

host material density $x = 1/N$, where N is the number of host material lattice sites of the super-cell (in our calculations we used a 64 Si atom super-cell). Assuming linear elasticity, it is convenient to use the following parameterization in order to describe a defect with concentration independent parameters:

$$\begin{aligned} C_{\alpha\beta} &\rightarrow C^{\mathrm{Si}}_{\alpha\beta} + x\Delta C_{\alpha\beta}, \\ \epsilon_{\alpha} &\rightarrow \epsilon^{\mathrm{Si}}_{\alpha} - x\,\Delta\epsilon_{\alpha}. \end{aligned} \tag{5.3}$$

$C^{\mathrm{Si}}_{\alpha\beta}$ are the elastic constants of Si and $\epsilon^{\mathrm{Si}}_{\alpha}$ is the strain applied to the host material Si. $\Delta\epsilon_{\alpha}$ and $\Delta C_{\alpha\beta}$ are the induced strain and modification of the elastic constants in reference to perfect Si respectively. For convenience the superscript Si in $\epsilon^{\mathrm{Si}}_{\alpha}$ will be

dropped, since we will assume from now on that all strains are reported with respect to relaxed and defect-free Si. Combining Eq. 5.1 and 5.3 leads to:

$$E(\epsilon_\alpha) = E_0 + \frac{\Omega}{2}\sum_{\alpha,\beta}(\epsilon_\alpha - x\Delta\epsilon_\alpha)(C^{\mathrm{Si}}_{\alpha\beta} + x\Delta C_{\alpha\beta})(\epsilon_\beta - x\Delta\epsilon_\beta). \tag{5.4}$$

By straining a given defect structure in various directions (e.g., hydrostatic, x, y, z) and fitting the results of the different strain conditions comprehensively to the equation-of-state shown in Eq. 5.4, the induced strains $\Delta\epsilon_\alpha$ and modified elastic constants $\Delta C_{\alpha\beta}$ can be determined. Often spatial symmetries of a defect further reduce the free parameters in Eq. 5.4, which enables determination of all parameters with a minimal set of strain calculations. This treatment using an equation-of-state has the advantage that once the free parameters $\Delta\epsilon_\alpha$ and $\Delta C_{\alpha\beta}$ are determined, the effect for arbitrary strain states is determined through Eq. 5.4 and no further calculations are required to determine the total super-cell energy of a given defect. These energies are directly related to the formation energies of defects. For example, the formation energy of an interstitial is defined as:

$$E^{\mathrm{I}}_f = \lim_{N\to\infty} E_{\mathrm{I}}(N+1) - \frac{N+1}{N}E_{\mathrm{Si}}(N), \tag{5.5}$$

this enables the treatment of local stress effects on formation and migration energies in TCAD process simulators. E_{I} and E_{Si} are the total energies of super-cells with $N+1$ and N Si atoms respectively.

So far all types of strain were considered (3 normal and 3 shear strains). Also $C_{\alpha\beta}$ is the full 6×6 elasticity tensor. For simplicity we restrict ourselves to normal strains in the remainder of this dissertation. We have made a limited number of calculations of defect energies in the presence of shear strains and have found effects to be negligible. However conceptually there is no loss in generality, since all following equations can be extended to include shear strains in a straightforward way. $\vec{\epsilon}$ and $\mathbf{C}$ indicate the normal strain component of the strain vectors and elasticity tensor

respectively. Thus Eq. 5.4 becomes:

$$E(\vec{\epsilon}) = E_0 + \frac{\Omega}{2}(\vec{\epsilon} - x\Delta\vec{\epsilon}) \cdot (\mathbf{C}^{\mathrm{Si}} + x\Delta\mathbf{C}) \cdot (\vec{\epsilon} - x\Delta\vec{\epsilon}). \tag{5.6}$$

Appendix E lists the analytical results for energy minima configurations and the associated curvature (2nd derivative) of Eq. 5.6 for various strain conditions. These relations are very helpful to analyze defects with high symmetry. Since we are only interested in the change of formation energies with respect to unstrained Si, $\Delta E_f(\vec{\epsilon}) = E_f(\vec{\epsilon}) - E_f(0)$, Eq. 5.6 can be further simplified to:

$$\Delta E(\vec{\epsilon}) = E(\vec{\epsilon}) - E(0) = -\Omega_0 \Delta\vec{\epsilon} \cdot (\mathbf{C}^{\mathrm{Si}} + \frac{1}{N}\Delta\mathbf{C}) \cdot \vec{\epsilon} + \frac{\Omega_0}{2}\vec{\epsilon} \cdot (N\,\mathbf{C}^{\mathrm{Si}} + \Delta\mathbf{C}) \cdot \vec{\epsilon}. \tag{5.7}$$

This equation becomes extremely useful for calculating the effect of stress/strain on formation energies in the following sections. Ω_0 is the atomic volume of crystalline Si, whereas N is the number of Si lattice sites in a super-cell of volume $\Omega = N\,\Omega_0$. N is related to the defect concentration x as mentioned earlier by $x = 1/N$. In the dilute limit (N large), Eq. 5.7 becomes:

$$\Delta E(\vec{\epsilon}) \approx \underbrace{-\Omega_0 \Delta\vec{\epsilon} \cdot \mathbf{C}^{\mathrm{Si}} \cdot \vec{\epsilon}}_{O(\epsilon)} + \underbrace{\frac{\Omega_0}{2}\vec{\epsilon} \cdot (N\,\mathbf{C}^{\mathrm{Si}} + \Delta\mathbf{C}) \cdot \vec{\epsilon}}_{O(\epsilon^2)}. \tag{5.8}$$

The leading order term in $\vec{\epsilon}$ is proportional to the induced strain $\Delta\vec{\epsilon}$, whereas changes of the elastic tensor $\Delta\mathbf{C}$ enter only into the term quadratic in $\vec{\epsilon}$. This indicates that the dominant effect of strain on formation/migration energies is due to the induced strains for small applied strains. When calculating formation/migration energies the term proportional to N always cancels out.

5.2 Elastic properties of silicon

To test whether density functional theory (DFT) can be used to predict elastic properties of materials using the method described in the previous section, we determined the equilibrium lattice constant and elastic constants of Si using two different DFT

functionals: LDA and GGA. For our calculations we used the density functional theory (DFT) code VASP [61, 62] with ultrasoft Vanderbilt type pseudo-potentials [63, 64]. All calculations were performed in local density approximation (LDA) or generalized gradient approximation (GGA) with a 64 silicon atom super-cell, an energy cutoff of 250 eV, 2^3 Monkhorst-Pack **k**-point sampling, and high precision FFT-grids (see Ref. [9]).

Due to the spatial symmetries of Si the elastic tensor $C^{\mathrm{Si}}_{\alpha\beta}$ can be parameterized by only three independent parameters. Usually these are C_{11}, C_{12}, and C_{44}. The latter one is related to shear strains. Here we focus only on the normal strain portion of the tensor:

$$\mathbf{C}^{\mathrm{Si}} = \begin{pmatrix} C_{11} & C_{12} & C_{12} \\ C_{12} & C_{11} & C_{12} \\ C_{12} & C_{12} & C_{11} \end{pmatrix}. \tag{5.9}$$

We calculated the energy versus strain relation of Si under hydrostatic and uniaxial strain (without compensation due to Poisson's ratio). We extracted the equilibrium lattice constant b_0 and bulk modulus K from the hydrostatic calculation, whereas C_{11} can be extracted from the uniaxial strain calculations (see Appendix E). Using $K = 1/3(C_{11} + 2C_{12})$, C_{12} can be determined once C_{11} and K are known. We also computed the Young's modulus Y and Poisson's ratio ν using their relations to C_{11} and C_{12}: $\nu = C_{12}/(C_{11}+C_{12})$ and $Y = C_{11}-2\nu C_{12} = (C_{11}^2+C_{11}C_{12}-2C_{12}^2)/(C_{11}+C_{12})$.

Figure 5.3 shows the results for the two different DFT functionals (LDA: left, GGA: right). For comparison the experimental values [74] are indicated in the graphs as dashed lines. Table 5.1 summarizes all parameters calculated. For consistency we determined C_{11} and C_{12} by fitting all results to the equation-of-state Eq. 5.6 and computed K, Y, and ν using the relations mentioned earlier. All elastic properties of Si are predicted well by either LDA and GGA. The well know fact that LDA underpredicts the equilibrium lattice constant by 0.7 % as well the over prediction of GGA by 0.6 % is reproduced [74]. Both functionals underpredict C_{11} (LDA: 6 %,

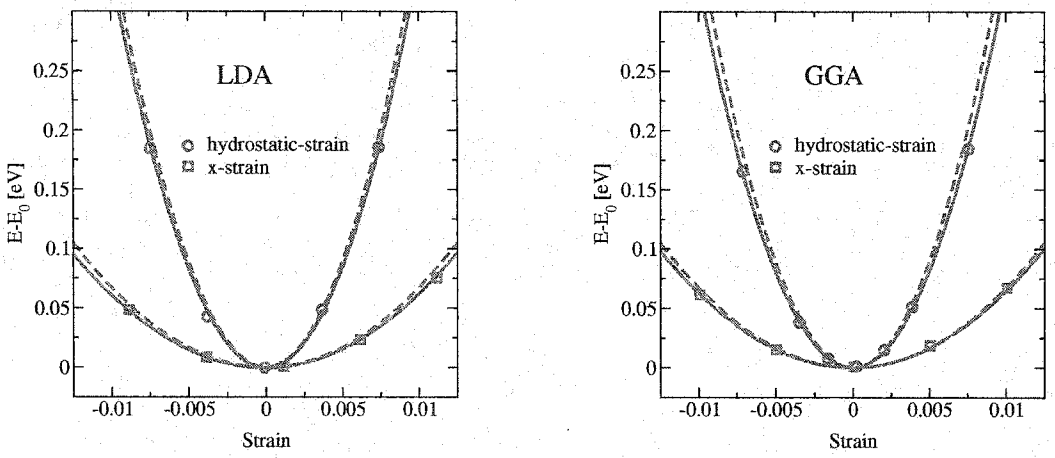

Figure 5.3: Comparison of LDA (left) and GGA (right) calculation of the elastic properties of Si with the experimental parameters. Solid lines indicate the LDA/GGA results, whereas dashed lines correspond to the experimental values. Shown is energy vs. hydrostatic (red lines) and uniaxial strain (blue lines) using a cutoff of 250 eV, 2^3 Monkhorst-Pack **k**-point sampling, and high precision FFT-grids (see Ref. [9]) for both DFT functionals. All energies are reported with respect to their minimum energy strain condition. The data shown corresponds to a 64 atom super-cell calculation. $\epsilon = 0$ response to the LDA/GGA Si lattice constant reported in Table 5.1. All extracted values are listed in Table 5.1.

GGA: 7 %). Overall the predictions of LDA and GGA are almost identical. LDA seems to predict the Si elastic properties slightly better, but since GGA is generally known to give more accurate formation energies [19, 52], we used the GGA functional for the analysis of stress effects on formation and migration energies throughout this work.

5.3 Stress effect on vacancy and interstitial equilibrium

Following the methodology of Section 5.1, we determined the induced strain and elasticity tensor for different point-defect structures (V, I_{split}, I_{hex}, and I_{tet}) by calculating the energy change for strain applied in different directions (e.g., hydrostatic, x, y, z). By combining the results of the different strain conditions, the elasticity constants $C_{\alpha\beta}$

Table 5.1: Comparison of experimental lattice constant b_0, elastic constants C_{ij}, bulk modulus K, Young's modulus Y, and Poisson's ratio ν of Si with LDA and GGA calculations (see Appendix G for details on the convergence level of the reported values).

Method	b_0 [Å]	C_{11} [GPa]	C_{12} [GPa]	K [GPa]	Y [GPa]	ν
Experiment [74]	5.4309	168	65	99	131	0.279
LDA	5.3903	158	65	96	120	0.292
GGA	5.4566	156	55	89	128	0.260

and modified equilibrium lattice dimensions can be extracted. Table 5.3 summarizes the results for the different point-defects. ΔC_{ij} and $\Delta\epsilon_i$ are the change in elasticity and equilibrium lattice constants due to a defect respectively. All calculations are performed in generalized gradient approximation (GGA) with a 64 silicon atom super-cell, an energy cutoff of 250 eV, and 2^3 (interstitial) or 3^3 (vacancy) Monkhorst-Pack **k**-point sampling depending on the structure. $x = 1/64$ since the super-cell used contains 64 Si lattice sites.

Figure 5.4 shows the energy versus hydrostatic strain for pure Si, a <110> split interstitial (I_{split}), and a vacancy (V). The system with a vacancy (V) prefers the lattice constant to be reduced by 0.34 % in comparison to Si. The system with an interstitial (I_{split}) shows the opposite behavior, with the lowest energy configuration a 0.31 % increased lattice constant. This indicates that in the presence of compressive strain the vacancy equilibrium concentration C_{V}^* will increase, whereas the interstitial equilibrium concentration C_{I}^* will decrease. Tensile strains will reverse the effect; increasing C_{I}^* and decreasing C_{V}^*. In order to quantitatively determine these changes, the change in formation energy under strain for the different point-defects need to be calculated. As mentioned earlier, the formation energy of I and V is defined by:

$$E_f^{\mathrm{I,V}}(\vec{\epsilon}) = \lim_{N\to\infty} E_{\mathrm{I,V}}(\vec{\epsilon}) - \frac{N \pm 1}{N} E_{\mathrm{Si}}(\vec{\epsilon}). \tag{5.10}$$

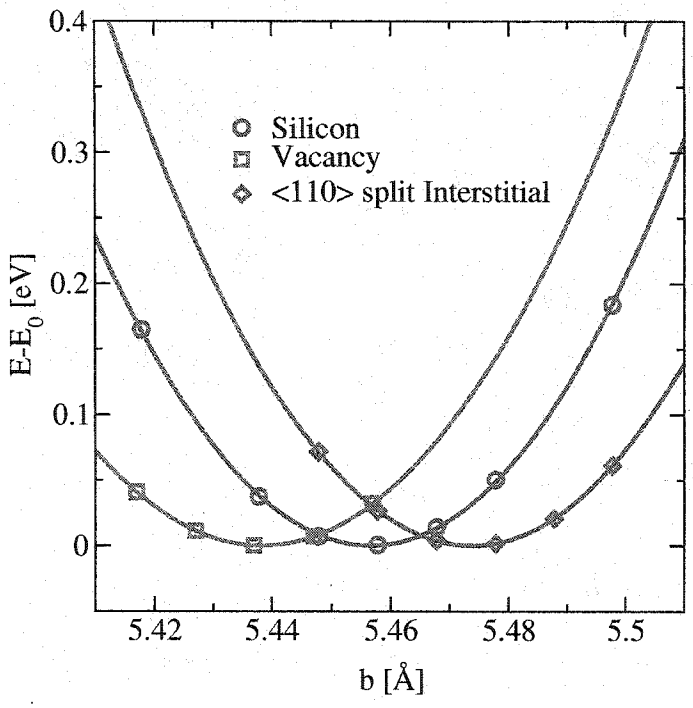

Figure 5.4: Energy vs. unit cell lattice constant b for hydrostatic strain for system with $2 \times 2 \times 2 = 8$ cells (64 Si atoms in defect-free system). The reference energy E_0 is defined as the minimum energy as function of unit cell size for a given configuration.

where $E_{\mathrm{I,V}}$ is the total energy of a super-cell containing an interstitial ($N+1$ Si atoms) or a vacancy ($N-1$ Si atoms) respectively. E_{Si} is the total energy of a N Si atom super-cell. We are interested in the change in formation energy $\Delta E_f^{\mathrm{I,V}}$. Combining Eq. 5.10 with the expression derived in Section 5.1 (Eq. 5.8) and taking the dilute limit ($N \to \infty$) results in:

$$\Delta E_f^{\mathrm{I,V}}(\vec{\epsilon}) = -\Omega_0 \, \Delta\vec{\epsilon}^{\,\mathrm{I,V}} \cdot \mathbf{C}^{\mathrm{Si}} \cdot \vec{\epsilon} + \frac{\Omega_0}{2}\vec{\epsilon} \cdot \left(\Delta\mathbf{C}^{\mathrm{I,V}} \mp \mathbf{C}^{\mathrm{Si}}\right) \cdot \vec{\epsilon}, \tag{5.11}$$

where $\Delta\vec{\epsilon}^{\,\mathrm{I,V}}$ is the induced strain vector, $\vec{\epsilon}$ is the applied strain vector, $\mathbf{C}^{\mathrm{Si}}$ is the elasticity tensor of Si, and Ω_0 is the Si atomic volume. The negative sign corresponds to I, whereas the positive sign is associated with the V case. We assume that the reference state for defects is unaffected by the applied stress/strain. The calculations show that

Table 5.2: Difference in formation energy of the different I configurations determined in unstrained Si in reference to I_{split}. The spatial I configurations are shown in Appendix B.

	ΔE_f [eV]
I_{split}	0.00
I_{hex}	0.09
I_{tet}	0.32

the dominant effect of stress in the case of I and V is to modify the equilibrium lattice dimensions (see Table 5.3). In contrast, the difference in the curvatures ΔC_{ij} have a secondary effect. In the subsequent analysis we only include the linear term in strain, which gives rise to the dominant effect due to the induced strain (difference in lattice dimension due to I or V incorporation).

Once the change in formation energy is known, the change in equilibrium constants follows directly. In the vacancy case, the change in equilibrium constant becomes:

$$\frac{C_{\mathrm{V}}^{*}(\vec{\epsilon})}{C_{\mathrm{V}}^{*}(0)} = \exp\left(\frac{-\Delta E_f^{\mathrm{V}}(\vec{\epsilon})}{kT}\right). \tag{5.12}$$

The analysis for interstitials is slightly more complicated, since there are various high symmetry I configurations. In this analysis, we considered the following three I configurations: <110> split interstitial (I_{split}), interstitial in hexagonal site (I_{hex}), and interstitial in tetrahedral location (I_{tet}). The difference in formation energies of the individual configuration in unstrained Si in reference to I_{split} are listed in Table 5.2. I_{tet} has a significantly higher formation energy of $\Delta E_f = +0.32\,\mathrm{eV}$ and therefore does not contribute significantly to C_{I}^{*}. Also the induced strain for I_{tet} is much smaller in comparison to I_{split} and I_{hex}. However since the induced strains of I_{split} and I_{hex} are of comparable magnitude and also the formation energies differ only by 0.09 eV in unstrained Si (see Table 5.2) both configurations need to be considered

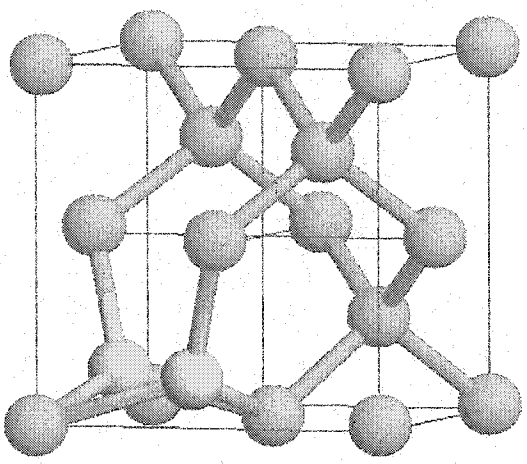

Figure 5.5: The gray atoms illustrate the structure of a [110] split/dumbbell interstitialcy (I_{split}). Note that for this structure, the interstitial is not a single atom, but rather two atoms in place of a single atom.

when calculating C_I^*. Nevertheless the calculation of C_I^* can be further simplified for a different reason. It turns out that the contributions of I_{hex} to C_I^* are also rather small in comparison to I_{split} due to the large configurational entropy factor of I_{split} ($\theta_{I_{split}} = 6$). A <110> split interstitial can take on six possible orientations in a Si diamond lattice ([110],[1$\bar{1}$0],[011],[01$\bar{1}$],[101],[10$\bar{1}$]).

$$\begin{aligned} C_I^* &= C_{I_{split}}^* + C_{I_{hex}}^* + C_{I_{tet}}^* \\ &= 6\,C_s \exp\left(-\frac{E_f^{I_{split}}}{kT}\right) + 2\,C_s \exp\left(-\frac{E_f^{I_{hex}}}{kT}\right) + C_s \exp\left(-\frac{E_f^{I_{tet}}}{kT}\right) \\ &\approx 6\,C_s \exp\left(-\frac{E_f^{I_{split}}}{kT}\right) \end{aligned} \tag{5.13}$$

Due to the spatial symmetry of V, I_{hex}, and I_{tet}, the induced strains are isotropic

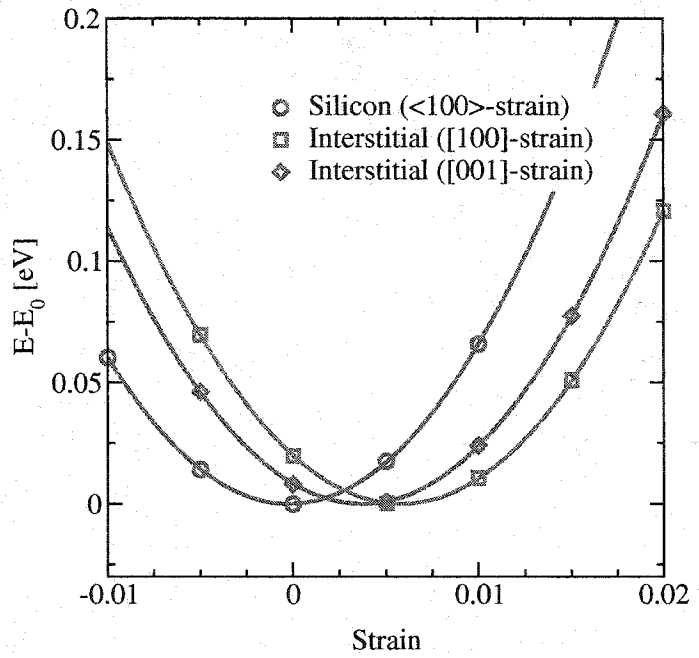

Figure 5.6: Energy vs. uniaxial strain in different directions for Si and I_{split} oriented in the [110] direction. The reference energy E_0 is defined as the minimum energy for a given configuration.

(see Table 5.3). In contrast, since <110> split interstitials (shown in Fig. 5.5) induce the largest strain in the x- and y-directions (Fig. 5.6), uniaxial or biaxial strain can lead to larger changes in the equilibrium point-defect concentration than would be predicted based on the hydrostatic activation volume. Qualitatively this behavior is expected due to the spatial configuration of I_{split}. Since the interstitial lies in the x-y plane, the Si diamond lattice gets more distorted in the x-y plane than in the z-direction.

In the case of biaxial strain:

$$\frac{C_{\mathrm{I}}^{*}(\epsilon)}{C_{\mathrm{I}}^{*}(0)} = \frac{1}{3}\exp\left(\frac{-\Delta E_f^{\mathrm{in}}(\epsilon)}{kT}\right) + \frac{2}{3}\exp\left(\frac{-\Delta E_f^{\mathrm{out}}(\epsilon)}{kT}\right), \tag{5.14}$$

where ΔE_f^{in} is the change in energy for in-plane interstitials (e.g. [110] or $[\bar{1}10]$ orientation for strain in x-y plane), whereas $\Delta E_f^{\mathrm{out}}$ is the change for split interstitials

Table 5.3: $\Delta\epsilon_i$ and ΔC_{ij} for V and different I configurations. Strains are reported in reference to the GGA Si equilibrium lattice parameter of 5.457 Å. ΔC_{ij} are calculated in respect to the GGA C_{ij}^{Si} reported in Table 5.1. The level of convergence of these results is discussed in Appendix G.

	V	I_{split}	I_{hex}	I_{tet}
$\Delta\epsilon_x$	−0.2207	+0.2595	+0.2019	+0.1201
$\Delta\epsilon_y$	−0.2207	+0.2595	+0.2019	+0.1201
$\Delta\epsilon_z$	−0.2207	+0.0469	+0.2019	+0.1201
ΔC_{11} [GPa]	−2221	−629	−688	−1682
ΔC_{22} [GPa]	−2221	−629	−688	−1682
ΔC_{33} [GPa]	−2221	−410	−688	−1682
ΔC_{12} [GPa]	−438	−151	223	799
ΔC_{13} [GPa]	−438	−50	223	799
ΔC_{23} [GPa]	−438	−50	223	799

with out-of-plane components (e.g., [011] orientation). Figure 5.7 shows the stress dependence of the equilibrium interstitial concentration (C_{I}^*) and vacancy concentration (C_{V}^*) under biaxial strain. A strong strain dependence of C_{I}^*, particularly for in-plane [110] interstitials can be seen. Interstitials prefer to be oriented in-plane under tensile strain and out-of-plane under compressive strain. Vacancies show the opposite behavior; compressive strain leads to an enhancement of C_{V}^*, due to a negative induced strain of vacancies.

5.4 Summary and conclusion

In summary, a framework for treating stress effects on formation energies was developed. The predictive power of DFT for elastic properties of materials was tested by calculation of the elastic properties of Si. Both functionals used (LDA and GGA)

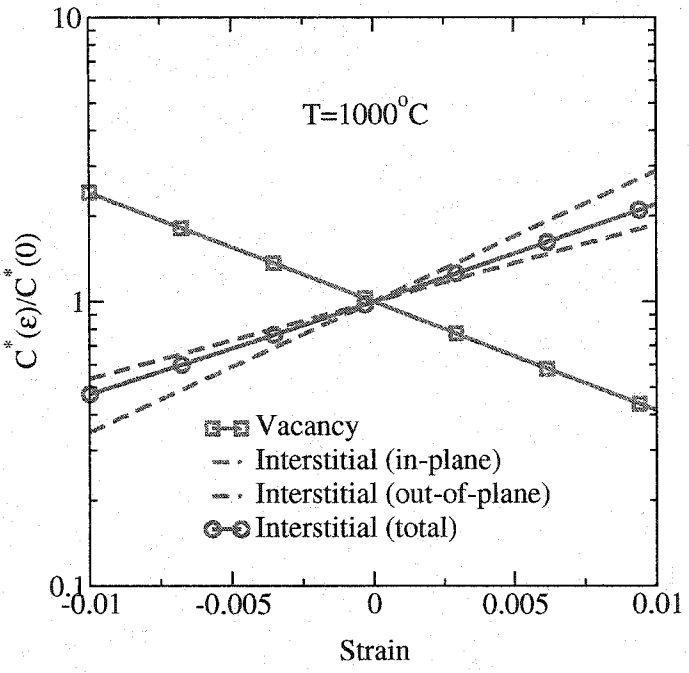

Figure 5.7: Strain dependence of $C_{\mathrm{I}}^{*}(\epsilon)/C_{I}^{*}(0)$ and $C_{\mathrm{V}}^{*}(\epsilon)/C_{\mathrm{V}}^{*}(0)$ in biaxially strained Si at $T = 1000\,^{\circ}\mathrm{C}$. For strain applied in the x-y plane, 1/3 of all <110> interstitials are purely in-plane, while 2/3 have out-of-plane components. The plot shows the contributions from the different I alignments and the resulting total. Vacancies show the opposite effect in comparison to interstitials due to the different sign of the induced strain (see Table 5.3). C_{V}^{*} gets enhanced under compressive strain and is reduced for tensile conditions.

predicted the elastic properties of Si well.

In addition, the introduced methodology was used to investigate the effect of stress on point-defect equilibrium concentrations. C_{V}^{*} becomes enhanced under compressive strains and reduced for tensile strains. C_{I}^{*} shows the opposite behavior.

For example, in the presence of 1 % tensile biaxial strain (e.g., MBE $\mathrm{Si/Si_{0.75}Ge_{0.25}}$ bilayer) at 1000 °C, we predict C_{I}^{*} to be enhanced by a factor of 2.2 and C_{V}^{*} to be reduced by 0.41. Under the equivalent compressive strain condition, C_{V}^{*} is predicted to shown an enhancement by a factor of 2.4, whereas C_{I}^{*} is predicted to be reduced by 0.47.

Chapter 6

STRESS EFFECT ON POINT-DEFECT AND DOPANT DIFFUSION

In the previous chapter, a general methodology for calculating stress effects on formation energies from first-principles and the resulting impact on point-defect equilibrium concentrations C_{I}^{*} and C_{V}^{*} were discussed. Stress effects on point-defects have direct impact on dynamic processes like TED and dopant activation. However besides point-defect energetics, diffusivities need to be known as well to predict the behavior of these dynamic processes. Since experiments are difficult and in the case of boron diffusion even lead to contradictory results [72], we utilize *ab-initio* calculations to predict stress effects on migration of dopants and point-defects. In contrast to previous work, our analysis extends beyond simple hydrostatic activation volumes [25] in order to be able to predict anisotropies associated with more complex stress states (e.g., differences between in-plane and perpendicular diffusion due to biaxial strain). We determine both strain tensors as well as changes in elastic constants due to defects and migration saddle points. In particular the stress effects on I, V, and B diffusivities are determined. In Section 6.4, the results for I and B are combined using a simple TED model to estimate the effect of stress on boron diffusion during TED.

Figure 6.1 shows schematically the energetics of a typical diffusion process for a defect X, where X is the mobile species of an immobile ground state X_s. For X_s to diffuse, first X needs to be formed and then the defect X needs to overcome the transition barrier E_m^{X} by passing through the transition state T. To simplify the analysis we assume that the defect X has been formed already. The transition rate Γ

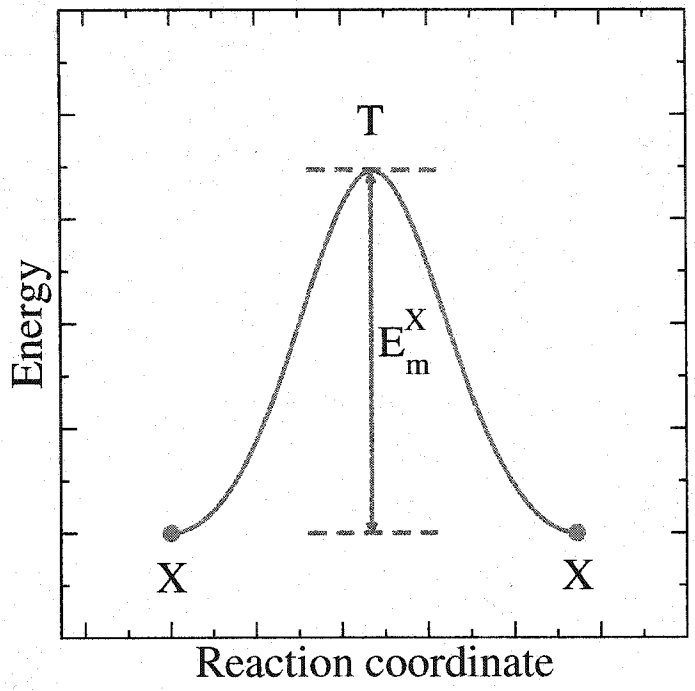

Figure 6.1: Schematic plot of the energetics of a typical diffusion process of species X. The transition rate Γ to overcome the barrier is $\Gamma = \Gamma_0 \exp(-E_m^{\mathrm{X}}/kT)$. T indicates the transition state, which is defined by the lowest energy migration saddle-point between the initial and final X configuration. E_m is the migration barrier, whereas Γ_0 is the attempt frequency including all entropy differences between X and T.

for X to overcome the migration barrier can be calculated in transition state theory [32]. Assuming harmonic approximation, Γ has the following form:

$$\Gamma = \Gamma_0 \exp\left(-\frac{E_m^{\mathrm{X}}}{kT}\right), \tag{6.1}$$

where Γ_0 is the attempt frequency including all entropy differences between X and T. The migration energy is defined in reference to the formation energy of the defect state X. The formation energy of T therefore is given by $E_f^{\mathrm{T}} = E_f^{\mathrm{X}} + E_m^{\mathrm{X}}$. The transition rate Γ and diffusivity D are directly linked by viewing the diffusion process as a random walk process at the atomic level (see Chapter 2). In one dimension, the

following relation holds [32]:

$$\langle \Delta x^2 \rangle = 2Dt, \tag{6.2}$$

where $\langle \Delta x^2 \rangle$ is the square of the average displacement of X during a random walk for a time t (average hop distance). In combination with Eq. 6.1 this relation leads directly to:

$$D = \frac{1}{2t} \langle \Delta x^2 \rangle = \frac{1}{2} \Gamma \langle \Delta x^2 \rangle = D_0 \exp\left(-\frac{E_m^{\mathrm{X}}}{kT}\right), \tag{6.3}$$

where $\Gamma = 1/t$ and $D_0 \equiv \frac{1}{2} \Gamma_0 \langle \Delta x^2 \rangle$. The diffusivity of species X is therefore directly linked to the migration barrier E_m^{X}. Under stress this migration barrier changes and therefore directly influences the diffusivity.

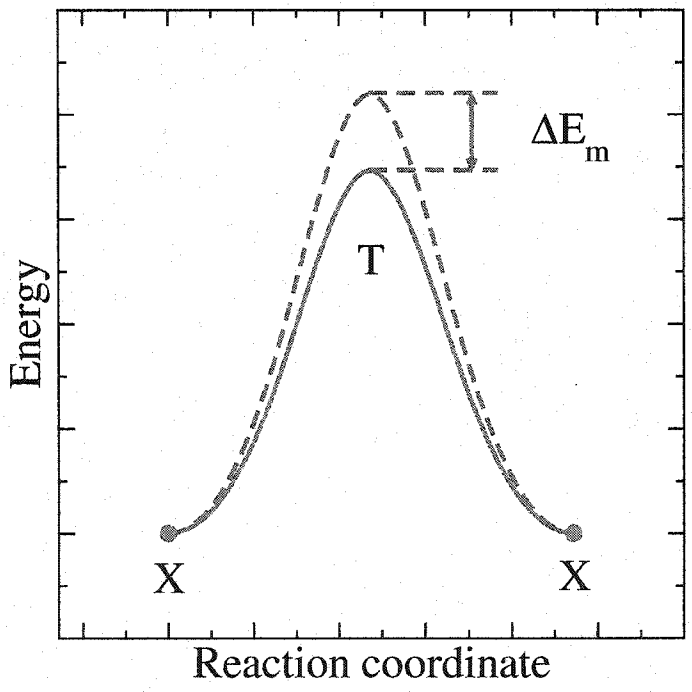

Figure 6.2: Stress effect on migration kinetics of defect X. ΔE_m is the change in migration barrier due to an applied stress. The blue solid line indicates the migration barrier in absence of stress, whereas the red dashed line shows an increase in the migration barrier by ΔE_m^{X}. The migration barrier is reported with respect to the energy of the complex X. This is important since the formation energy of the complex X can be also stress dependent.

Figure 6.2 illustrates this effect. The blue solid line indicates the barrier without stress, whereas the red dashed line shows the new barrier including the stress effect. Under stress the transition rate is reduced by a factor of $\exp(-\Delta E_m^{\mathrm{X}}/kT)$. However, not only is the migration barrier E_m^{X} a function of stress, but the formation energy of the defect X is as well. Hence, a more suitable quantity is $C_{\mathrm{X}}^* D$. This product depends only on the formation energy of the transition state E_f^{T}. This is also the experimentally observed diffusivity, since it includes the formation of the defect X as discussed earlier. Typically formation energies are reported in respect to the lowest energy configuration of a species X, which is usually the immobile species X_s.

$$C_{\mathrm{X}}^* D = \theta_{\mathrm{X}} C_s \exp\left(-\frac{E_f^{\mathrm{X}}}{kT}\right) D_0 \exp\left(-\frac{E_m^{\mathrm{X}}}{kT}\right) = \theta_{\mathrm{X}} C_s D_0 \exp\left(-\frac{E_f^{\mathrm{T}}}{kT}\right). \tag{6.4}$$

where we used $C_{\mathrm{X}}^* = \theta_{\mathrm{X}} C_s \exp\left(-\frac{E_f^{\mathrm{X}}}{kT}\right)$ (see Appendix A).

Equation 6.4 shows that E_f^{T} alone determines the stress dependence of the diffusivity as long as the entropy contributions in θ_{X} and D_0 are stress independent. Similar to the treatment in the previous chapter, the formation energy of the transition state under stress can be expressed as:

$$E_f^{\mathrm{T}}(\vec{\epsilon}) = E_f^{\mathrm{T}}(0) + \Delta E_f^{\mathrm{T}}(\vec{\epsilon}), \tag{6.5}$$

where $\vec{\epsilon}$ is the present strain state, $E_f^{\mathrm{T}}(0)$ is the formation energy in unstrained material, and $\Delta E_f^{\mathrm{T}}(\vec{\epsilon})$ is the change in formation energy due to the present strain. The analysis of the effect of stress on diffusion becomes equivalent to the analysis of equilibrium concentrations. The only difference is that here the stress dependence of the transition state needs to be calculated instead of the ground state. In most cases, one is interested in the relative change in diffusivity due to the presence of a certain stress state. Combining Eq. 6.4 and 6.5 and neglecting the stress dependence of the entropy factors leads to:

$$\frac{(C_{\mathrm{X}}^* D)(\vec{\epsilon})}{(C_{\mathrm{X}}^* D)(0)} = \frac{(\theta_{\mathrm{X}} D_0)(\vec{\epsilon})}{(\theta_{\mathrm{X}} D_0)(0)} \exp\left(-\frac{\Delta E_f^{\mathrm{T}}(\vec{\epsilon})}{kT}\right) \approx \exp\left(-\frac{\Delta E_f^{\mathrm{T}}(\vec{\epsilon})}{kT}\right). \tag{6.6}$$

The effect of stress on diffusivity is now reduced to calculating $\Delta E_f^{\mathrm{T}}(\vec{\epsilon})$ following the methodology developed in Chapter 5. In the remainder of this chapter, this is done for I, V, and B. Similar to the analysis in Chapter 5, the induced strains and changes in elastic constants are determined for the various transition states.

6.1 Stress effect on V diffusion

Vacancy diffusion is the simplest diffusion process. Figure 6.3 (left) shows schematically the transition process. A vacancy simply interchanges its location with a nearest neighbor atom. The energetics of the process are shown on the right side of Fig. 6.3. The vacancy migrates along the <111> direction through the vacancy transition state T. The transition state shown was determined using the the nudged elastic band (NEB) method [10, 11, 12].

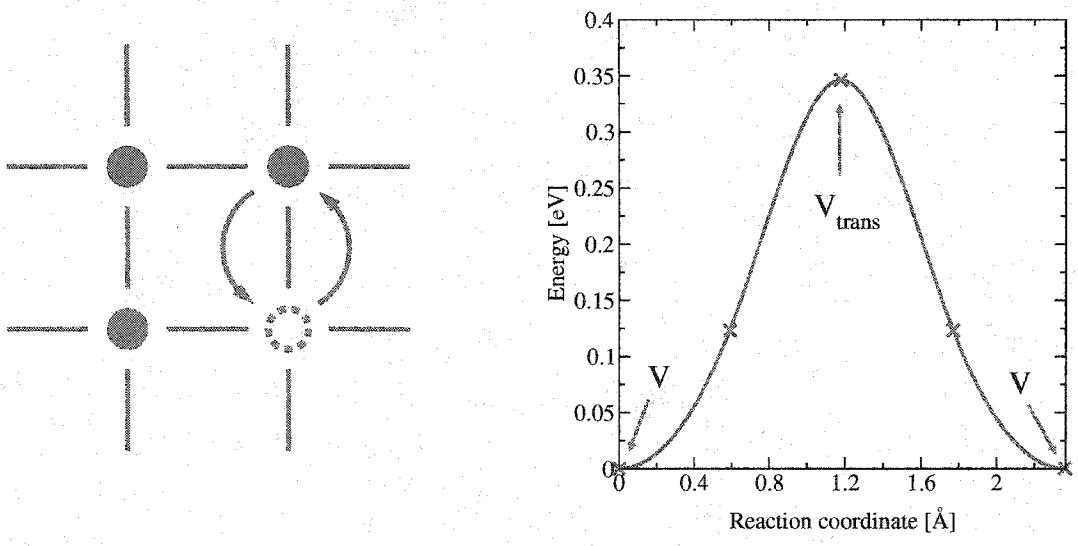

Figure 6.3: Left: Schematic plot of vacancy transition. Green circles indicate Si atoms, whereas the green-dashed circle represents a vacancy. Right: Energetics of vacancy migration process in unstrained Si. The migration barrier and transition state was determined with the NEB method [10, 11, 12].

According to the previous section (see Eq. 6.6), to determine the effect of stress on the vacancy diffusivity it is only necessary to calculate the change in formation energy of the transition state V_{trans} under stress. Analog to Section 5.3, the stress dependence of V_{trans} is given by:

$$\Delta E_f^{V_{trans}}(\vec{\epsilon}) = -\Omega_0 \, \Delta\vec{\epsilon}^{V_{trans}} \cdot \mathbf{C}^{Si} \cdot \vec{\epsilon} + \frac{\Omega_0}{2}\vec{\epsilon} \cdot \left(\Delta\mathbf{C}^{V_{trans}} + \mathbf{C}^{Si}\right) \cdot \vec{\epsilon}, \qquad (6.7)$$

where $\Delta\vec{\epsilon}^{V_{trans}}$ is the induced strain vector, $\vec{\epsilon}$ is the applied strain vector, $\mathbf{C}^{Si}$ is the elasticity tensor for Si, $\Delta\mathbf{C}^{V_{trans}}$ is the change in elasticity tensor due to V_{trans} and Ω_0 is the Si atomic volume. We assume that the reference state for defects is unaffected by the applied stress/strain (e.g., stress free surface). In the following results, we only include the linear term in strain, which gives rise to the dominant effect due to the induced strain.

Figure 6.4 shows the change in formation energy of V_{trans} as a function of hydrostatic strain for a 64 atom super-cell. Due to the high symmetry of the transition state ($x \leftrightarrow y \leftrightarrow z$) the shift of the energy minimum from zero strain is the induced strain for V_{trans} (see Appendix E). The vacancy transition state shows a rather large negative induced strain of $\Delta\epsilon_x = \Delta\epsilon_y = \Delta\epsilon_z = -0.4199$, which translates into a reduction in the diffusion activation energy under compressive strain. Figure 6.5 shows the V diffusivity enhancement as a function of biaxial strain. Due to the negative induced strain, compressive strains lead to an enhancement of diffusivity, whereas tensile strains reduce the diffusivity.

6.2 Stress effect on I diffusion

The lowest energy configuration for an interstitial in unstrained silicon is the split or dumbbell configuration. Two silicon atoms share a single Si lattice site elongated in the <110> direction. Figure 6.6 shows the lowest reported migration path for such an interstitial [46]. In contrast to the previous discussed vacancy diffusion, the migration of such an interstitial involves a two-step process. In the first step the interstitial

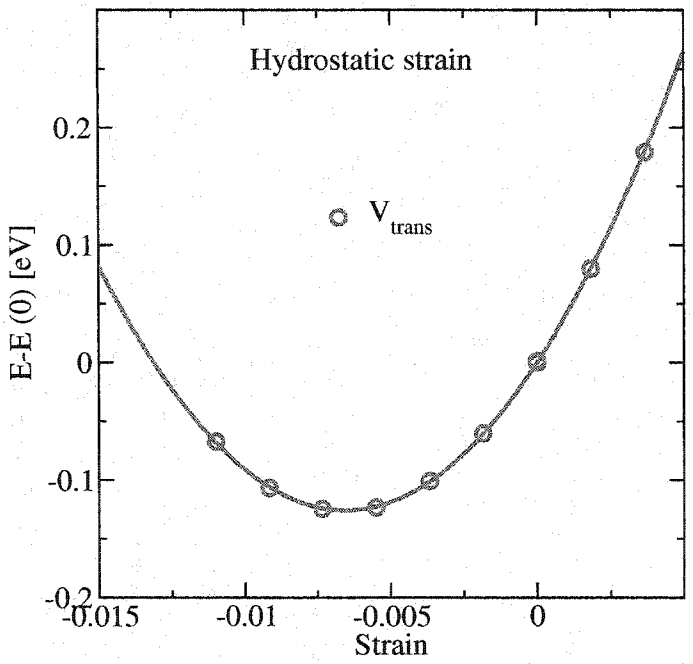

Figure 6.4: Energy vs. hydrostatic strain for system with $2 \times 2 \times 2 = 8$ cells (64 Si atoms in defect-free system). The graph shows the behavior of the vacancy transition state under hydrostatic strain. All energies are reported with respect to the energies in unstrained Si. Strains are reported in reference to the GGA Si equilibrium lattice parameter of 5.457 Å.

migrates along the <311> direction through the transition state T_1 to a hexagonal interstitial configuration. Since the whole transition is symmetric in unstrained Si the second step involves migrating from the hexagonal state through a second transition state T_2 to the final split configuration.

Following the ideas of the previous section, the effect of stress on the formation energies of the transition states T_1 and T_2 need to be determined in order to calculate the stress effect on interstitial diffusion. Figure 6.7 shows schematically the effect of stress on the two-step migration process. In the case of anisotropic stress (e.g., biaxial stress) the two transition states are affected differently, since the transition directions are not necessarily along the same <311> direction and therefore the orientations of

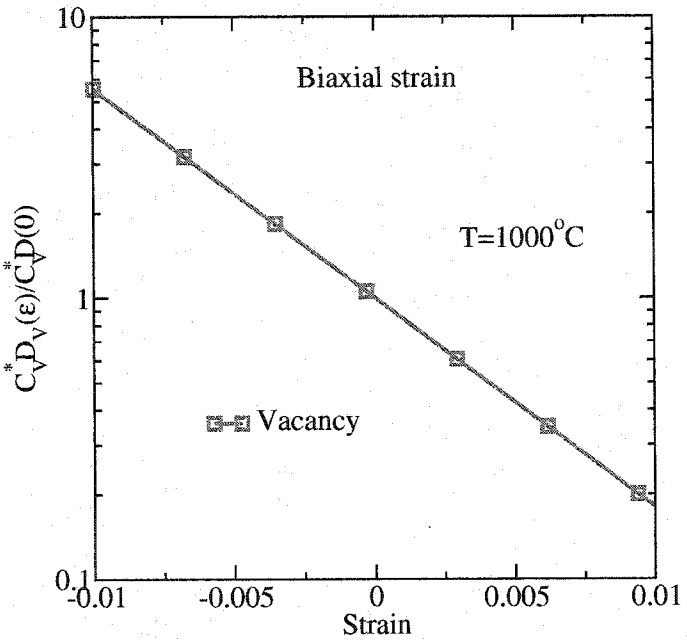

Figure 6.5: Relative V diffusivity change under biaxial strain at $T = 1000°C$. V diffusivity gets enhanced under compressive biaxial strain. $C_V^* D_V(0)$ is the diffusivity of V in unstrained Si.

the transition states are different. T_1 and T_2 have different formation energies under anisotropic strain. This directly affects the transition rates of the two processes, which translates into potential anisotropic diffusion.

The extraction of diffusivities differs from the analysis in the previous sections; however it turns out that the basic idea, calculating the stress dependence of the formation energy of the transition state, remains the same. First the result of the first-principles calculations for the stress dependence of the transition states will be presented, then we use different approaches to extract the interstitial diffusivity from the calculated results.

Due to the symmetry of the migration process it is sufficient to reduce the problem to the transition $I_{split} \rightarrow I_{hex}$, which is shown in Fig. 6.8. Similar to the vacancy analysis we used the NEB method to identify the transition state I_{trans} and calculate

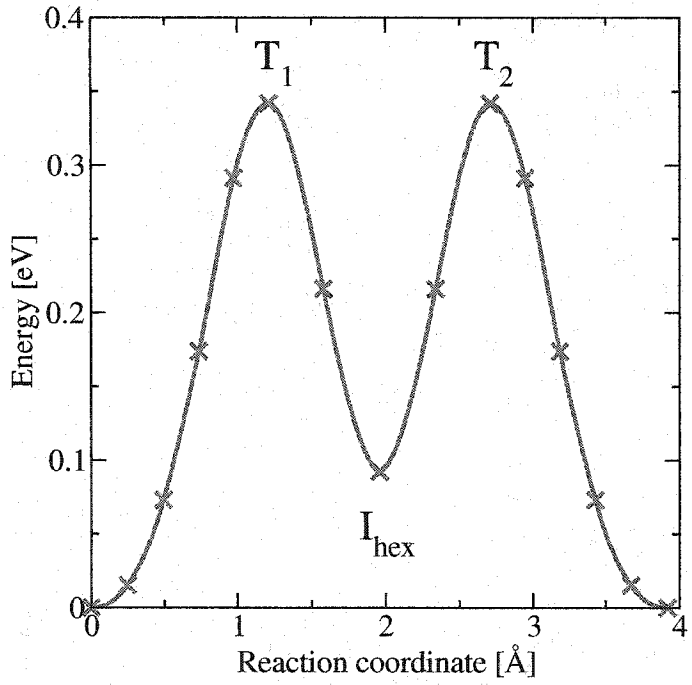

Figure 6.6: $I_{split} \rightarrow I_{hex} \rightarrow I_{split}$ transition calculated using the NEB method [10, 11, 12] in unstrained Si (GGA Si equilibrium lattice parameter $b_0 = 5.457$ Å).

its strain dependence. Figure 6.9 shows a comparison of elastic properties of the V and I transition state with defect-free Si under hydrostatic strain. By just determining the minimum energy lattice constant of V_{trans} and I_{trans} the qualitative effect of stress on diffusivity can be extracted. V_{trans} shows a reduced lattice constant in comparison to Si, which indicates a negative induced strain. The I transition state shows the opposite behavior, a positive induced strain. Negative induced strains lead to enhancement of diffusivity under compressive strain conditions, whereas positive induced strains enhance the diffusivity for tensile strains. Based on the hydrostatic calculation, we expect to see an enhancement of I diffusivity for tensile stress.

Since the I transition state does not have the high symmetry of V_{trans}, additional strain calculations are required to extract the induced strain vector $\Delta\vec{\epsilon}$ of the I transition state. Figure 6.10 shows the results of uniaxial strain calculations of I_{trans}. Strain

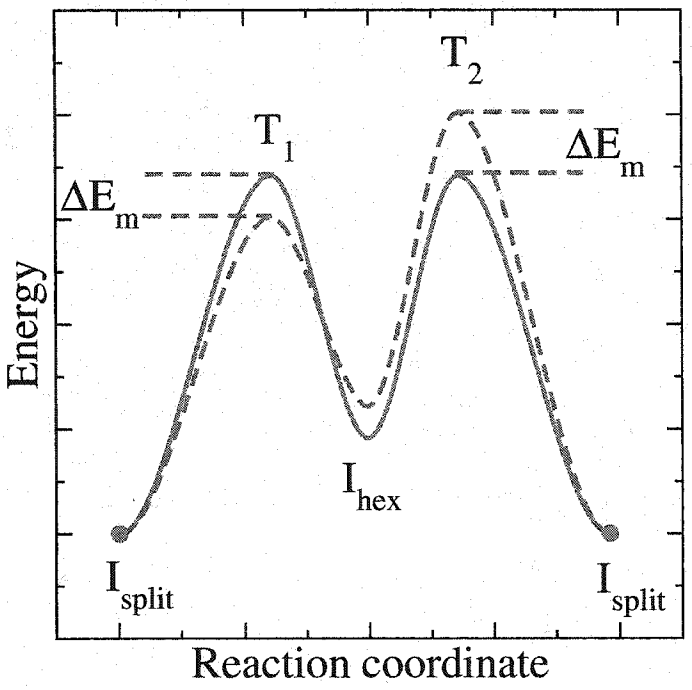

Figure 6.7: Schematic illustration of stress effect on two-step transition. The blue solid line shows the transition path in unstrained Si. When stress/strain is present the transition path gets altered (red dashed line), and for anisotropic strain, the migration barriers of T_1 and T_2 are no longer the same which can result in anisotropic diffusion.

was applied along the three cartesian directions (x,y,z) for a transition with the hop vector $(3,1,1)b/8$ (b is the Si lattice constant). The data shows a very interesting behavior. The induced strains in the x-direction is much larger than the induced strains in the y- and z-directions. This fact translates directly into anisotropic diffusion for anisotropic strain conditions (e.g., uniaxial or biaxial strain). The anisotropy also depends on the hop vector. Equation 6.3 shows that the diffusivity is proportional to the square of the hop distance Δx^2 and the transition rate Γ. The largest induced strain (x-direction) coincides with the largest hop direction (x-direction), which results in a strain effect which is largest in the dominant direction of motion.

Following the methodology of the previous chapter, we fitted the results for various

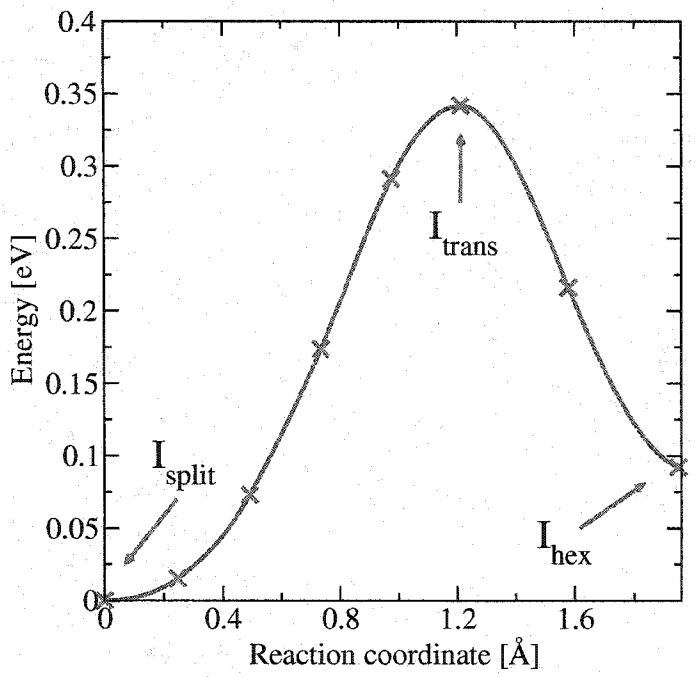

Figure 6.8: $I_{split} \rightarrow I_{hex}$ transition determined using the NEB method in unstrained Si (GGA Si equilibrium lattice parameter $b_0 = 5.457\,\text{Å}$).

strain conditions for I_{trans} to Eq. 5.6 in order to determine the induced strain vector $\Delta\vec{\epsilon}$ and modified elasticity tensor $\Delta\mathbf{C}$. Besides the shown hydrostatic and uniaxial data, we also performed biaxial strain calculations, which were included to determine all free parameters. Table 6.1 lists the extracted induced strains for V_{trans} and I_{trans}, which indicate a strong anisotropy in the I strain interactions. In contrast to the V diffusion, the quantitative prediction of I diffusion under stress (including the anisotropy) is more complicated and will be discussed in the next sections. First an analytic model to describe the stress effect on I diffusivity is developed and then compared to a kinetic lattice Monte Carlo (KLMC) simulation, which includes anisotropic stress effects.

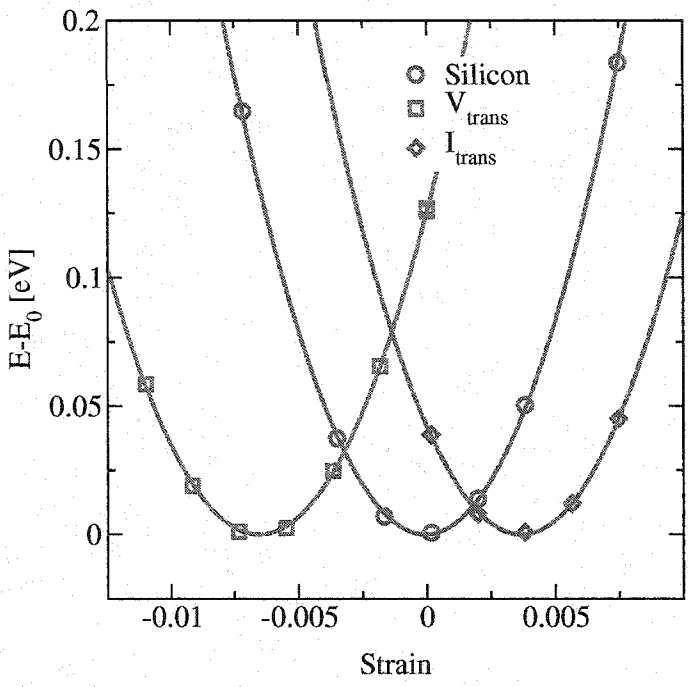

Figure 6.9: Energy vs. hydrostatic strain for system with $2 \times 2 \times 2 = 8$ cells (64 Si atoms in defect-free system). The reference energy E_0 is defined as the minimum energy as a function of unit cell size for a given configuration. The graph shows the behavior of the vacancy and interstitial transition state under hydrostatic strain. The vacancy transition state shows a negative induced strain, which translates into a reduction in the diffusion activation energy under compressive strain, whereas the interstitial transition shows the opposite effect. Strains are reported in reference to the GGA Si equilibrium lattice parameter of 5.457 Å.

6.2.1 Analytic analysis of stress effect on I diffusivity

In order to account quantitatively for strain effects, the two-step transition needs to be considered. The different spatial orientations of the transition states T_1 and T_2 with respect to the applied strain are responsible for the anisotropic diffusion behavior. Figure 6.11 shows the 3D configuration of the 12 hexagonal interstitial sites surrounding a I_{split} site. If the orientation of I_{split} is neglected (this constraint is relaxed in Section 6.2.2), there are 72 possible two-step transitions ($I_{split} \rightarrow I_{hex} \rightarrow I_{split}$) from

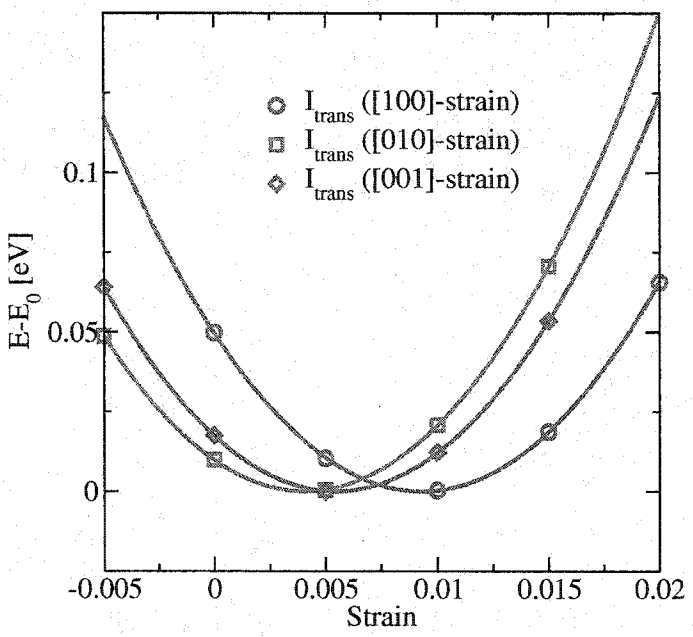

Figure 6.10: Energy vs. uniaxial strain in different directions for the transition state of $I_{split}[110] \rightarrow I_{hex}$ with hop vector $(3,1,1)b/8$, where b is the Si lattice constant. Note that the strain effect is largest in the dominant direction of motion.

Table 6.1: Induced strains for V and I transition state extracted from Figs. 6.9 and 6.10. Strains are reported in reference to the GGA Si equilibrium lattice parameter of 5.457 Å.

		$\Delta\epsilon_\alpha$
V_{trans}	$\Delta\epsilon_x = \Delta\epsilon_y = \Delta\epsilon_z$	-0.4199
I_{trans}	$\Delta\epsilon_x$	0.5421
	$\Delta\epsilon_y$	0.0257
	$\Delta\epsilon_z$	0.1089

a I_{split} site. Figure 6.12 illustrates this schematically.

The orientation of the transition state, and therefore the hop direction, determines

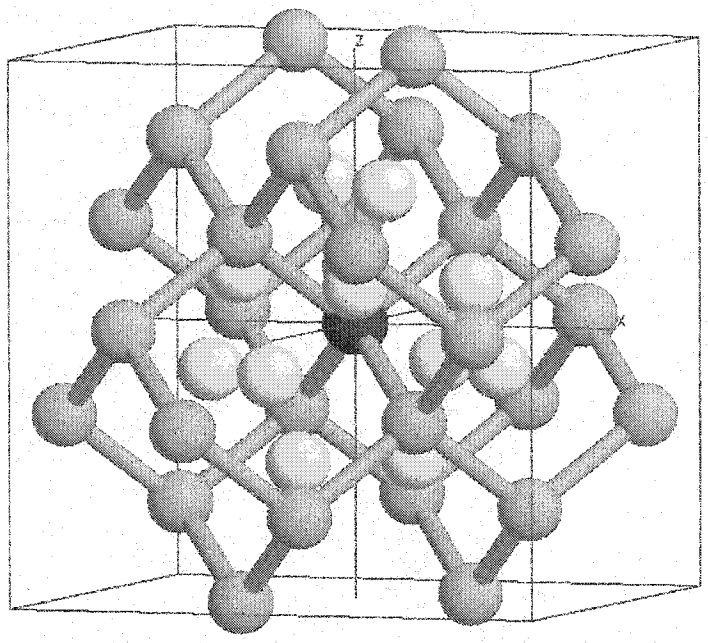

Figure 6.11: I_{split} site (red atom) with its 12 surrounding hexagonal interstitial sites (white atoms). Originating from the I_{split} site shown in red, there are 72 possible two-step transitions ($I_{split} \rightarrow I_{hex} \rightarrow I_{split}$).

the transition rate to each hexagonal site ($I_{split} \rightarrow I_{hex}$):

$$\Gamma_i = \Gamma_0 \exp\left[\frac{-\Delta E_m^i(\vec{\epsilon})}{kT}\right], \tag{6.8}$$

where Γ_0 is the transition rate in unstrained Si and $\Delta E_m^i(\vec{\epsilon})$ is the energy change of the migration barrier due to the present strain. Each hexagonal site is surrounded by six I sites (see Figs. 6.11 and 6.12). The rates Γ_j from the hexagonal site to the final I location determine the probability p_j for each process. Knowing the displacement from the initial I site Δx_{ij}^2 and neglecting correlation between subsequent two-step ($I_{split} \rightarrow T_1 \rightarrow I_{hex}$) hops, the diffusivity in the x-direction can be written as:

$$D_x = \frac{1}{2}\sum_{i=1}^{12}\Gamma_i\left(\sum_{j=1}^{6} p_j \Delta x_{ij}^2\right), \tag{6.9}$$

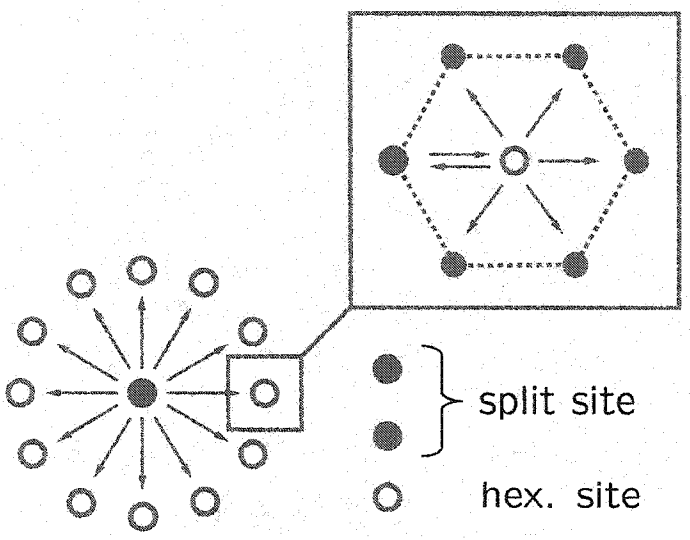

Figure 6.12: Schematic illustration of the two-step process for interstitial migration. Originating from the split site shown in red, there are 72 possible two-step transitions ($I_{split} \rightarrow I_{hex} \rightarrow I_{split}$). 12 different initial $I_{split} \rightarrow I_{hex}$ transitions followed by 6 possible $I_{hex} \rightarrow I_{split}$ transitions for each initial transition.

where Δx_{ij} is the x-component of the displacement vector $\Delta\vec{x}_{ij}$. Appendix F lists the displacement vectors for all 72 transitions. The other components of the diffusivity tensor $\mathbf{D}$ follow equivalently by replacing Δx_{ij}^2 with the corresponding term (e.g. in the case of D_{xy}, Δx_{ij}^2 is replaced by $\Delta x_{ij}\Delta y_{ij}$). p_j is defined by:

$$p_j = \frac{\Gamma_j}{\sum_{n=1}^{6}\Gamma_n}. \tag{6.10}$$

$\Delta E_m^i(\vec{\epsilon})$ is assumed to have the form of Eq. 6.7. To simplify the analysis, the transition state was assumed to be independent of the initial orientation of the interstitial. This implies that for a hop in the <311> direction, the induced strain for I_{trans} in the y- and z-direction should be equal. Therefore the average value from Table 6.1 was used ($\Delta\vec{\epsilon} = (\Delta\epsilon_x, \Delta\bar{\epsilon}_y, \Delta\bar{\epsilon}_y)$). All terms in Eq. 6.9 can be summed and in the case of biaxial strain $\vec{\epsilon} = (\epsilon, \epsilon, -\tilde{\nu}\,\epsilon)$ the analytic result is:

$$\frac{C_I^* D_x(\epsilon)}{C_I^* D_x(0)} = \frac{6}{33}\frac{20\Gamma_1^2 + 12\Gamma_1\Gamma_2 + \Gamma_2^2}{\Gamma_0(4\Gamma_1 + 2\Gamma_2)},$$

$$\begin{aligned}
\frac{C_{\mathrm{I}}^* D_y(\epsilon)}{C_{\mathrm{I}}^* D_y(0)} &= \frac{C_{\mathrm{I}}^* D_x(\epsilon)}{C_{\mathrm{I}}^* D_x(0)}, \\
\frac{C_{\mathrm{I}}^* D_z(\epsilon)}{C_{\mathrm{I}}^* D_z(0)} &= \frac{6}{33} \frac{4\Gamma_1^2 + 20\Gamma_1\Gamma_2 + 9\Gamma_2^2}{\Gamma_0(4\Gamma_1 + 2\Gamma_2)},
\end{aligned} \tag{6.11}$$

where $\Gamma_i = \Gamma_0 \exp(-\Delta E_i(\epsilon)/kT)$ and

$$\begin{aligned}
\Delta E_1(\epsilon) &= -\Omega_0(\Delta\epsilon_x + \Delta\bar{\epsilon}_y)(C_{11}^{\mathrm{Si}} + C_{12}^{\mathrm{Si}} - \tilde{\nu}\, C_{12}^{\mathrm{Si}}), \\
\Delta E_2(\epsilon) &= -\Omega_0(\Delta\bar{\epsilon}_y + \Delta\bar{\epsilon}_y)(C_{11}^{\mathrm{Si}} + C_{12}^{\mathrm{Si}} - \tilde{\nu}\, C_{12}^{\mathrm{Si}}).
\end{aligned} \tag{6.12}$$

$\tilde{\nu} = 2\,C_{12}^{\mathrm{Si}}/C_{11}^{\mathrm{Si}}$ is the biaxial Poisson ratio (see Appendix E). The off-diagonal terms of the diffusivity tensor vanish ($C_{\mathrm{I}}^* D_{xy} = C_{\mathrm{I}}^* D_{xz} = C_{\mathrm{I}}^* D_{yz} = 0$). Equation 6.11 shows an anisotropy between in-plane and out-of-plane diffusion. The final result for interstitial diffusion using above equations is shown in Fig. 6.13. Biaxial tension (as in strained Si on SiGe) leads to significantly higher in-plane diffusion compared to the perpendicular direction, with lateral diffusivity predicted to be approximately 90 % higher than vertical diffusion for 1 % tensile strain at 1000 °C.

6.2.2 KLMC analysis of stress effect on I diffusivity

In the previous section analytic expressions for the stress effect on I diffusion were derived (see Eq. 6.11). In the derivation it was assumed that consecutive transitions are uncorrelated and also the split interstitial orientation was neglected. Both assumptions were necessary to get a simple analytic expression for the diffusivity enhancement under stress.

Figure 6.14 shows a [110] split interstitial and the accessible I_{hex} sites. Only 4 out of the 12 surrounding I_{hex} site are accessible via the low transition barrier shown in Fig. 6.8. In unstrained material, an analytic expression could be derived to account for this fact; however in the presence of anisotropic stress the formation energy of the different I_{split} configurations gets affected differently, which makes the analytic analysis for arbitrary strain states extremely difficult. In order to overcome this problem and to be able to check the validity of the assumptions used in the previous

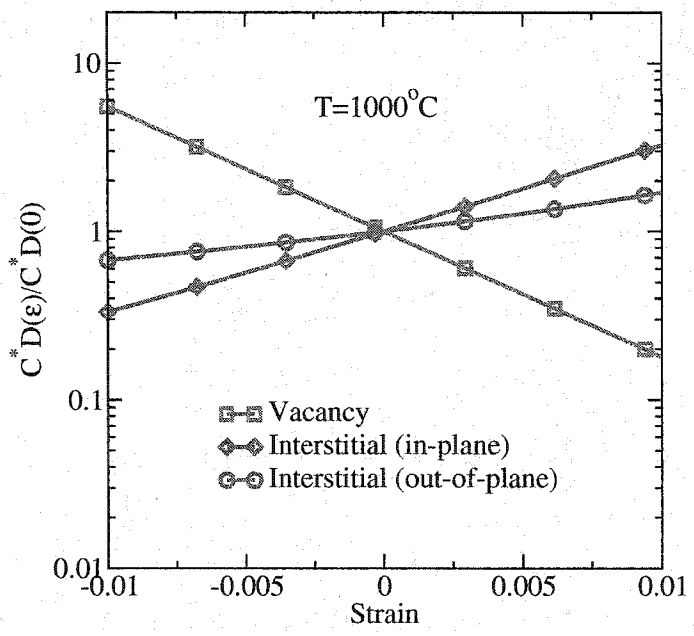

Figure 6.13: Relative I and V diffusivity change under biaxial strain at $T = 1000\,^{\circ}\mathrm{C}$ based on analytic model. V diffusivity gets enhanced under compressive biaxial strain, whereas interstitial diffusion shows the opposite effect. Also interstitials show anisotropic diffusion. The graph shows the in-plane and out-of-plane components for interstitials as a function of biaxial strain ϵ. $C^*D(0)$ is the diffusivity of I or V in unstrained Si.

section, we modeled the stress dependent I diffusion process via kinetic lattice Monte Carlo (KLMC) technique.

The first step was to determine the KLMC network/lattice. Since the Si diamond lattice consists of two fcc sub-lattices, there are 12 different I_{split} configurations (2 different sub-lattice locations with 6 different I_{split} orientations each). Figure 6.15 shows the 12 surrounding hexagonal sites (white atoms) for initial I_{split} configurations (red/green atom) located on the two different Si sub-lattices. Depending on the orientation of I_{split} (not shown in figure), 4 out of the 12 hexagonal sites are accessible through the low energy transition.

Analyzing the spatial configurations of the different hexagonal interstitial sites, one

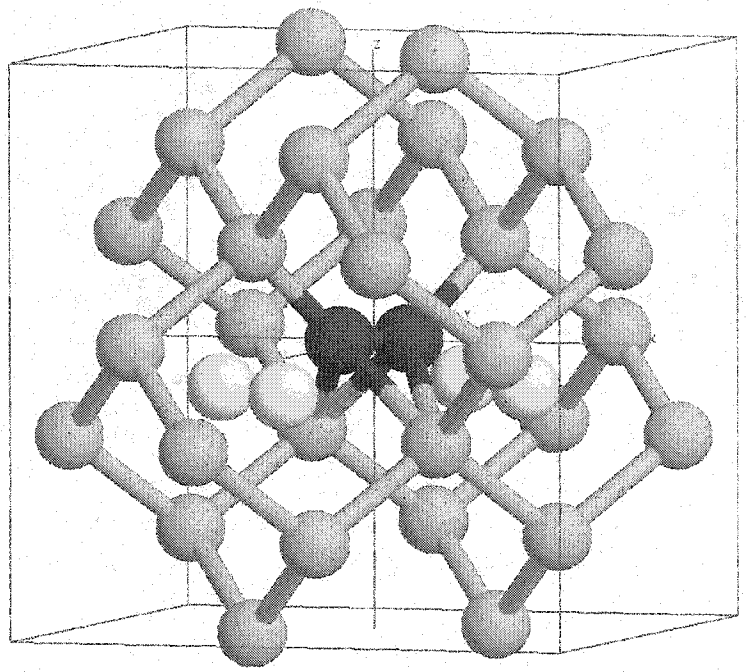

Figure 6.14: [110] split interstitial (red atoms) with the four surrounding I_{hex} sites, which are accessible via the low energy transition reported in Fig. 6.8. The fact that not all 12 surrounding I_{hex} sites are accessible via this low energy path, suggests that there exists a correlation between subsequent transitions.

finds that there are only four unique hexagonal interstitial configurations. Figure 6.16 shows the 4 unique hexagonal configurations surrounding the I_{split} sites for each of the the two fcc sub-lattices. By comparing the hexagonal rings I_{hex} occupies in the individual cases, it is easy to see that there are only 4 unique hexagonal sites in the Si diamond lattice.

Combining all these spatial configurations and allowing only transitions with the appropriate I_{split} orientation to occur (see Fig. 6.14), a I diffusion lattice (KLMC network) is determined. Figure 6.17 shows the schematic layout of the network.

S1-S6 (red symbols) label the split sites on the first fcc sub-lattice, whereas S1-S6 (green symbols) label the different split sites on the second fcc sub-lattice. H1-H4 are

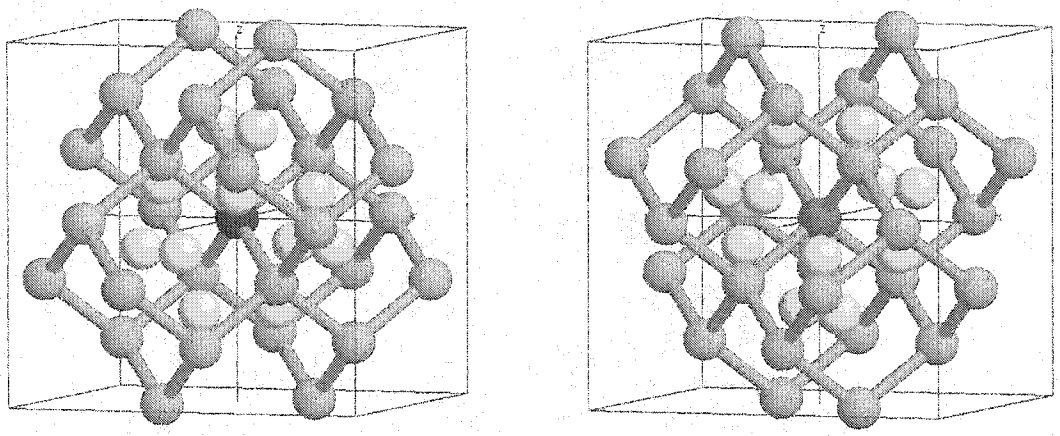

Figure 6.15: Hexagonal interstitial sites (white atoms) surrounding initial I_{split} located on the different fcc sub-lattices of the Si diamond crystal structure (Left: Sub-lattice with origin at $(0,0,0)\,b$. Right: Sub-lattice with origin at $(1/4,1/4,1/4)\,b$). b is the lattice constant of Si.

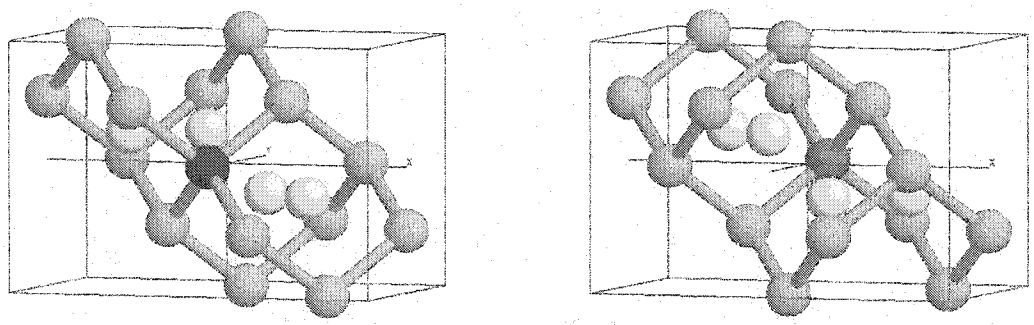

Figure 6.16: Left: Unique hexagonal sites (white atoms) surrounding an I_{split} (red atom) on the fcc sub-lattice of Si with origin at $(0,0,0)\,b$. Right: Unique hexagonal sites (white atoms) surrounding an I_{split} (green atom) on the fcc sub-lattice of Si with origin at $(1/4,1/4,1/4)\,b$. b is the lattice constant of Si.

the four unique hexagonal interstitial sites. Each arrow indicates a set of transition vectors (listed in Appendix F). Analogous to the analysis in the previous section,

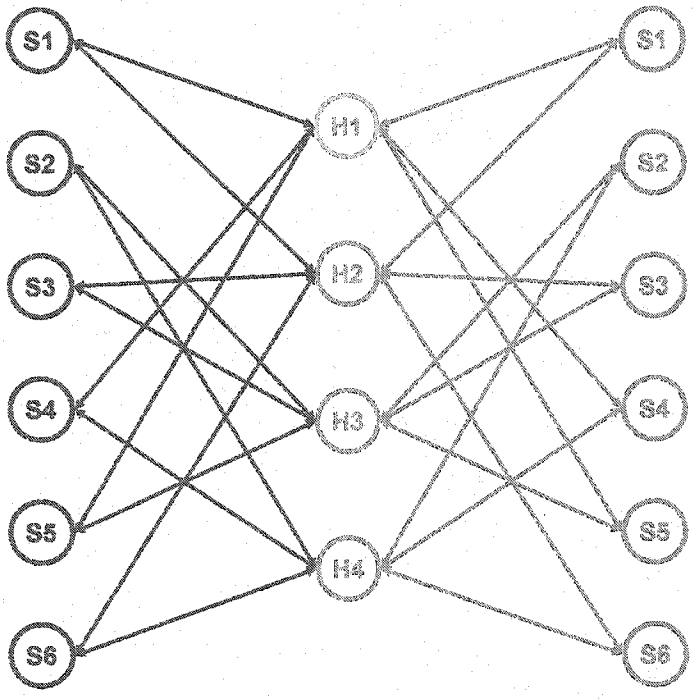

Figure 6.17: KLMC network for interstitial diffusion $I_{split} \rightarrow I_{hex} \rightarrow I_{split}$. S1-S6 (red symbols) are the 6 I_{split} configuration on the sub-lattice with origin at $(0,0,0)\,b$, S1-S6 (green symbols) are the 6 I_{split} configuration on the sub-lattice with origin at $(1/4,1/4,1/4)\,b$, and H1-H4 are the 4 unique hexagonal interstitial sites connecting the various I_{split} configurations. The arrows indicate the transition vectors of the possible transitions. Appendix F lists the individual transition vectors of the network.

we assume that the transition vectors indicate the orientation of the transition states. Once the orientation of a given transition state is known, the associated induced strain $\Delta\vec{\epsilon}^{I_{trans}}$ is determined. The transition rate for arbitrary stress/strain states follows (analog to Eq. 6.7):

$$\Gamma(\vec{\epsilon}) = \Gamma_0 \exp\left(-\frac{\Delta E_f^{I_{trans}}(\vec{\epsilon})}{kT}\right). \tag{6.13}$$

We neglect possible changes in entropy of the transition state I_{trans} due the presence of stress. Like in the analytic analysis we also assume transitions in the <311> direction, which implies the induced strain for I_{trans} in the y- and z-direction to be equal. Therefore the average value from Table 6.1 was used ($\Delta\vec{\epsilon} = (\Delta\epsilon_x, \Delta\bar{\epsilon}_y, \Delta\bar{\epsilon}_y)$).

Using the standard KLMC technique described in Chapter 2, the different entries of the diffusivity tensor can be determined by using the relation between average displacement and diffusivity in a random walk process:

$$D_{ij} = \frac{1}{2t}\langle \Delta\vec{x}_i \Delta\vec{x}_j \rangle, \tag{6.14}$$

where D_{ij} is a component of the diffusivity tensor $\mathbf{D}$ and $\Delta\vec{x}$ is the displacement vector in the time t. $\Delta\vec{x}_i$ is the i's component of the displacement vector. Besides the effect of stress on the diagonal elements of the diffusivity tensor (D_x,D_y, and D_z), we also computed the off-diagonal elements (D_{xy},D_{xz}, and D_{yz}). For biaxial stress these terms vanish as they do in the unstrained case.

The results of the KLMC calculations for biaxial strain in comparison to the analytic model are shown in Fig. 6.18. Both methods result in very similar predictions, which validates the assumptions made in the analytic model.

6.3 Stress effect on B diffusion

The effect of stress on B diffusion under different stress conditions has been investigated experimentally by various researchers [75, 13, 25, 14, 27, 76]. In the experiments, either hydrostatic pressure or biaxial strain (epitaxially grown SiGe bilayers) was applied. Since experiments are difficult, so far there is no consensus of the results for biaxial strain. Here we use *ab-initio* calculations to determine the stress effect.

There is broad agreement that B diffusion is dominated by the migration of an uncharged BI pair. Windl *et al.* [77] investigated various charged and uncharged BI diffusion paths using the NEB method and found the lowest migration barrier for the uncharged BI transition $\mathrm{B}_s + \mathrm{I}_{tet} \rightarrow \mathrm{BI}_{hex} \rightarrow \mathrm{B}_s + \mathrm{I}_{tet}$. BI_{hex} is a interstitial B atom in a hexagonal site. In the following, $\mathrm{B}_s + \mathrm{I}_{tet}$ is written as BI_{tet}. Figure 6.19 shows the migration path for this transition in unstrained Si calculated using the NEB method.

B diffusion, similar to the interstitial case, also involves a two-step process. In fact, the analysis in the previous sections for I diffusion can be directly applied to

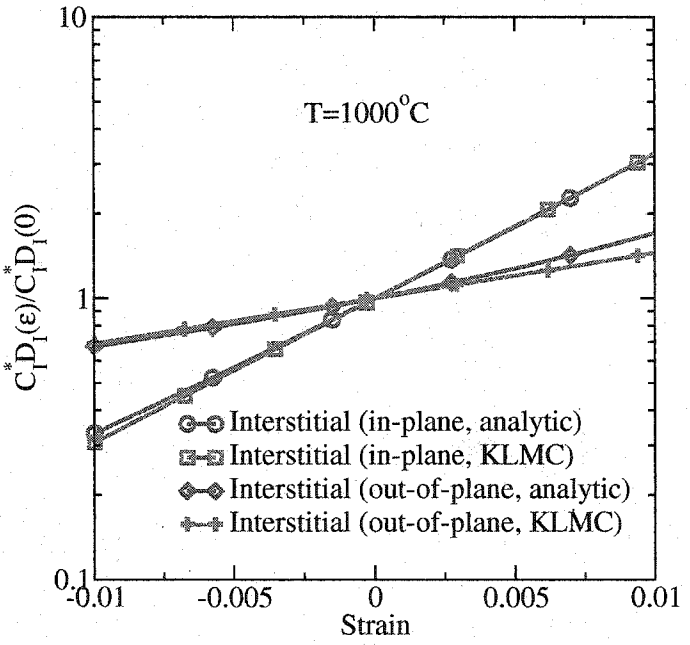

Figure 6.18: Comparison of stress effect on I diffusion under biaxial strain determined by the analytic model described in Section 6.2.1 with the KLMC analysis of this section.

B diffusion. Both transitions happen along the <311>-direction with an interstitial atom in a hexagonal site for the final atom configuration. To determine the stress effect on B diffusion, the elastic properties of the transition states T_1 and T_2, shown in Fig. 6.19, need to be determined. However since the transition is symmetric, it is sufficient to calculate the properties of only one transition state. Similar to the calculations for I in the previous section, we only consider half of the two-step transition ($BI_{tet} \rightarrow BI_{hex}$) shown in Figure 6.20 to determine the induced strain vector $\Delta\vec{\epsilon}^{B_{trans}}$ and modified elastic tensor $\Delta\mathbf{C}^{B_{trans}}$ of the transition state B_{trans}.

The formation energy of the transition state is defined as:

$$E_f^{\mathrm{B_{trans}}} = \lim_{N\to\infty} E_{\mathrm{B_{trans}}}(N) - E_{\mathrm{B}_s}(N) - \frac{1}{N}E_{\mathrm{Si}}(N), \tag{6.15}$$

where N is the number of Si lattice sites in a super-cell. $E_{\mathrm{B_{trans}}}$, E_{B_s}, and E_{Si} are the

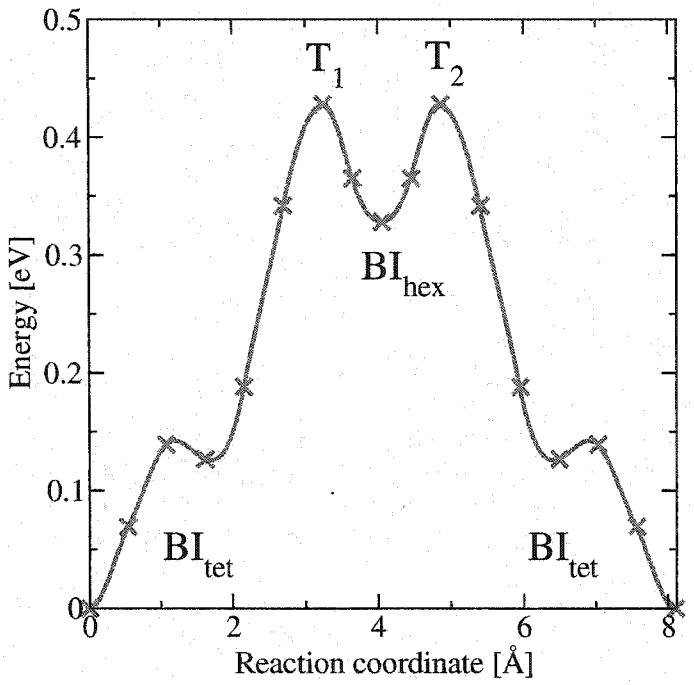

Figure 6.19: $BI_{tet} \rightarrow BI_{hex} \rightarrow BI_{tet}$ transition calculated using the NEB method [10, 11, 12] in unstrained Si (GGA Si equilibrium lattice parameter $b_0 = 5.4578\,\text{Å}$).

total energies of a super-cell containing B_{trans}, a substitutional B (B_s), and defect-free Si respectively. Again we are only interested in the variation of the formation energy of B_{trans} with respect to unstrained Si.

$$\Delta E_f^{\mathrm{B_{trans}}}(\vec{\epsilon}) = E_f^{\mathrm{B_{trans}}}(\vec{\epsilon}) - E_f^{\mathrm{B_{trans}}}(0) \tag{6.16}$$

By using Eq. 5.7, Eq. 6.16 turns into:

$$\Delta E_f^{\mathrm{B}trans}(\vec{\epsilon}) = -\Omega_0 \left(\Delta\vec{\epsilon}^{\mathrm{B}trans} - \Delta\vec{\epsilon}^{\mathrm{B}_s}\right) \cdot \mathbf{C}^{\mathrm{Si}} \cdot \vec{\epsilon} + \frac{\Omega_0}{2}\vec{\epsilon} \cdot \left(\Delta\mathbf{C}^{\mathrm{B}trans} - \Delta\mathbf{C}^{\mathrm{B}_s} - \mathbf{C}^{\mathrm{Si}}\right) \cdot \vec{\epsilon}. \tag{6.17}$$

This indicates that besides determining the elastic properties of B_{trans}, the induced strain and modified elasticity tensor of substitutional B also need to be calculated. The effective induced strain in the linear strain term of Eq. 6.17 is $\Delta\vec{\epsilon}^{\mathrm{B}trans} - \Delta\vec{\epsilon}^{\mathrm{B}_s}$. Similarly the quadratic strain term involves $\Delta\mathbf{C}^{\mathrm{B}trans} - \Delta\mathbf{C}^{\mathrm{B}_s} - \mathbf{C}^{\mathrm{Si}}$.

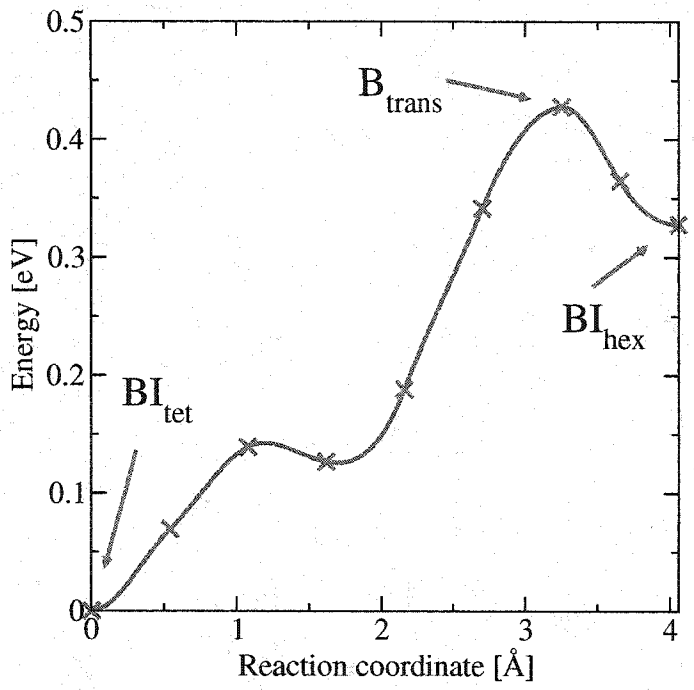

Figure 6.20: $BI_{tet} \rightarrow BI_{hex}$ transition calculated using the NEB method [10, 11, 12] in unstrained Si (GGA Si equilibrium lattice parameter $b_0 = 5.4578$ Å).

Figure 6.21 shows the energy dependence as a function of hydrostatic strain of a system with B_{trans}, B_s, and perfect Si (for reference). B_s exhibits a large negative induced strain, whereas B_{trans} shows a moderate positive induced strain under hydrostatic strain. Due to the high symmetry of B_s ($x \leftrightarrow y \leftrightarrow z$) the induced strain under hydrostatic strain is $\Delta\epsilon_x$ (see Appendix E). In Chapter 7, this induced strain determined from hydrostatic calculations is compared to x-ray diffraction data and shows excellent agreement with the experimental observations (see Fig. 7.9). Since B_{trans} does not have the high spatial symmetry of B_s additional energy versus strain relations were calculated to determine the induced strain vector $\Delta\vec{\epsilon}_{B_{trans}}$.

Figure 6.22 shows the results for different uniaxial strain. Very similar to I_{trans}, B_{trans} shows different induced strains in the x-direction (dominant direction of motion) in comparison to the y and z-directions. This is a clear indication of an anisotropic

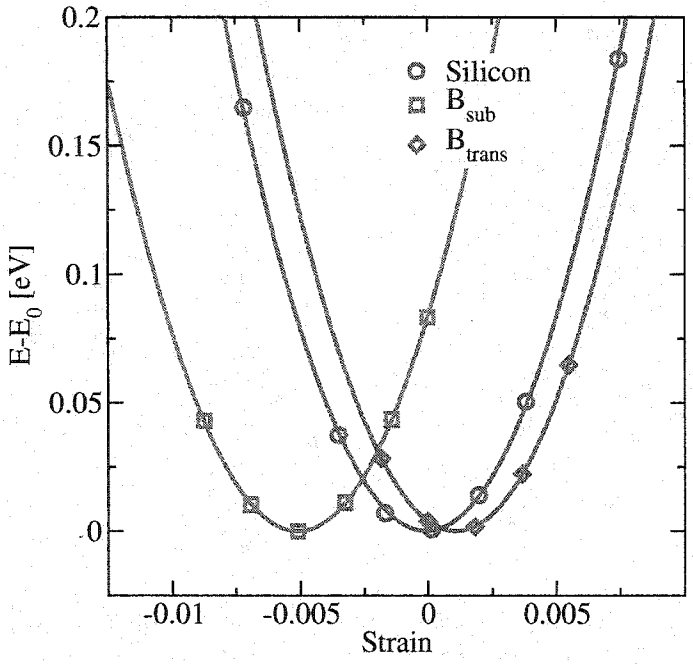

Figure 6.21: Energy vs. hydrostatic strain for system with $2 \times 2 \times 2 = 8$ cells (64 Si atoms in defect-free system). The reference energy E_0 is defined as the minimum energy as function of unit cell size for a given configuration. The graph shows the behavior of the Si, substitutional B, and BI transition state (B_{trans}) under hydrostatic strain. Strains are reported in reference to the GGA Si equilibrium lattice parameter of 5.4578 Å.

B diffusion analog to I diffusion. Figure 6.22 shows another interesting feature, the energy vs. strain relations for y- and z-strain are identical. In the case of I_{trans} we saw only an approximate symmetry and we had to use an averaging scheme in order to use the analytic and KLMC analysis. In the case of B_{trans} this is not necessary, since the assumed symmetry between y and z is present. Table 6.2 lists the induced strains for B_s and B_{trans} which were determined by fitting to the equation-of-state Eq. 5.6.

Once the induced strains for B_s and B_{trans} are known, the analysis for I diffusion can be repeated exactly. Figure 6.23 shows the change in B diffusivity as a function of biaxial strain. The graph shows anisotropic behavior between in-plane (lateral) and out-of-plane (vertical) diffusion similar to interstitials. However in the case of B

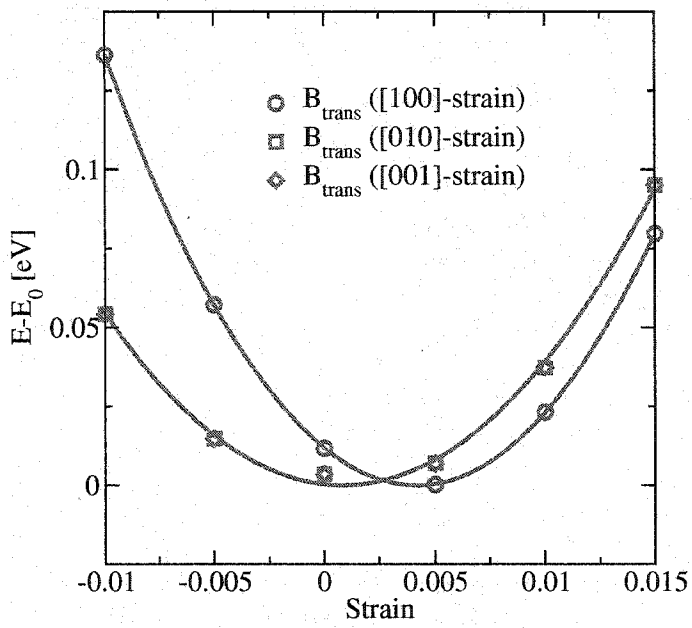

Figure 6.22: Energy vs. uniaxial strain in different directions for the transition state of $BI_{tet} \rightarrow BI_{hex}$ with hop vector $(3,1,1)b/8$, where b is the Si lattice constant. Note that the strain effect is largest in the dominant direction of motion.

Table 6.2: Induced strains for B_s and B transition state extracted from Figs. 6.21 and 6.22. Strains are reported in reference to the GGA Si equilibrium lattice parameter of 5.457 Å.

		$\Delta\epsilon_\alpha$
B_s	$\Delta\epsilon_x = \Delta\epsilon_y = \Delta\epsilon_z$	-0.327
B_{trans}	$\Delta\epsilon_x$	$+0.288$
	$\Delta\epsilon_y$	-0.036
	$\Delta\epsilon_z$	-0.036

the strain effect on diffusion is stronger than for I due to the rather large negative induced strain of B_s. Like in the I diffusion case, the off-diagonal elements of the B diffusion tensor vanish.

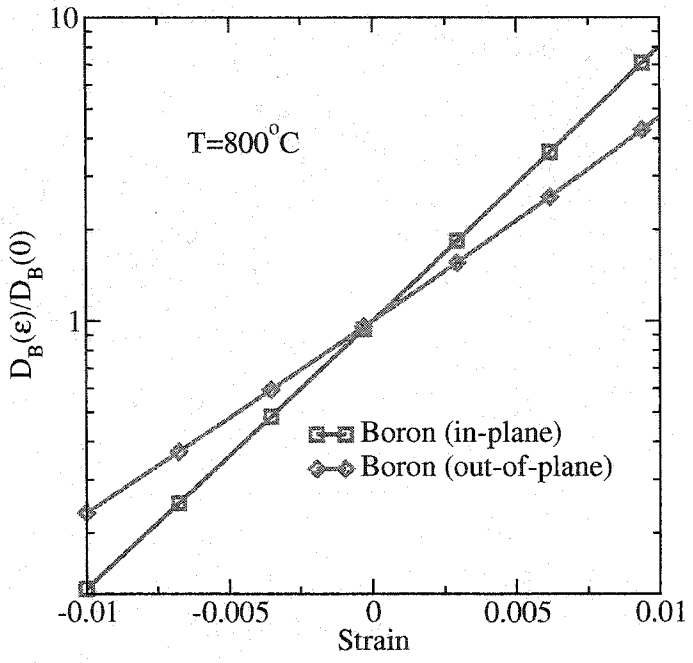

Figure 6.23: B diffusion enhancement as a function of biaxial strain at 800 °C predicted by Eq. 6.11.

The predictions in Fig. 6.23 for vertical diffusion enhancement under biaxial strain can be directly compared to experimental data by Kuo *et al.* [13] shown in Fig. 6.24. Experimentally the B diffusivity was determined in epitaxially grown SiGe bilayers with different Ge content to create a well defined biaxial strain state. In the experiment only the out-of-plane (vertical) B diffusivity was measured (blue lines). The B diffusivity enhancement was determined at different Ge concentrations and showed similar strain dependence. Combining these measurements with hydrostatic strain data by Aziz *et al.* [14], enables the determination of the in-plane (lateral) B diffusivity (black line). This analysis is done based on the relations between the hydrostatic and biaxial activation volumes. The details can be found in Ref. [25, 27].

Comparing the theoretical predictions shown in Fig. 6.23 with the experimental data shows general good agreement, however our theoretical calculations predict a

slightly stronger effect for both vertical and lateral B diffusion enhancement. Since there is still debate about the quality of the experimental measurements [13, 76], further measurements are necessary to confirm the experimental values.

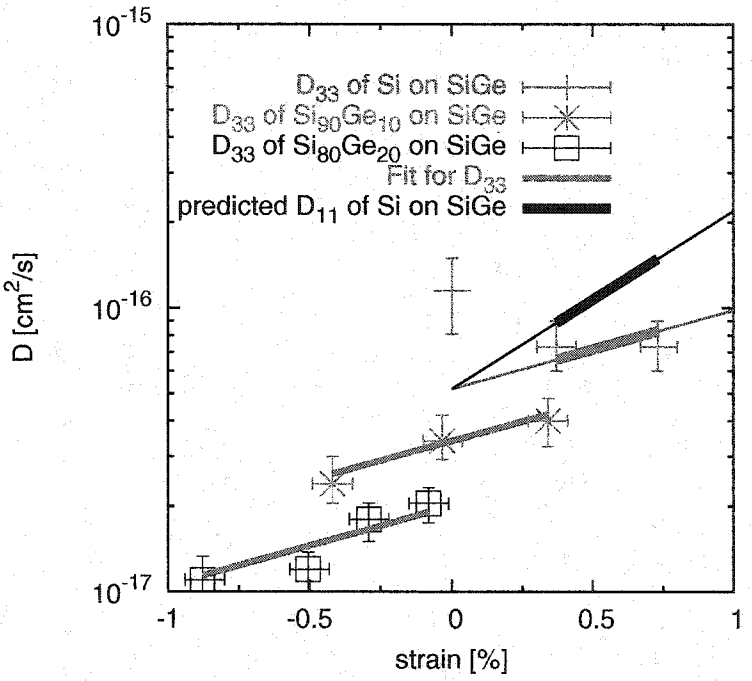

Figure 6.24: Experimental data by Kuo *et al.* [13]. The vertical B diffusion enhancement was measured under biaxial strain using SiGe bilayers with different Ge content (blue lines). The data was combined with hydrostatic B diffusion data from Aziz *et al.* [14] to determine the lateral B diffusion enhancement (black line).

6.4 Stress effect on B TED

In the previous sections, the effect of stress on point-defect diffusion and B diffusion were determined. These parameters are of high interest since they are closely related to transient enhanced diffusion (TED) of boron and also have strong impact on the activation dynamics of dopants. Boron activation under stress will be discussed in the next chapter. Here we develop a very simple model to estimate the stress effect on

boron TED. Since I and B showed anisotropic diffusion in the presence of anisotropic stress states, it is of major interest to see how the anisotropic behavior of I and B translates into TED effects.

High dose implants lead to a supersaturation of interstitials during the early stages of dopant anneals. Since B diffuses dominantly via an interstitial mechanism (formation of a mobile BI pair), B equilibrium diffusivity D_{B}^{*} gets enhanced by orders of magnitude in the presence of I supersaturation. The B diffusivity is enhanced until C_{I} reaches C_{I}^{*} again. This one to one correspondence between I supersaturation and enhanced B diffusivity can be expressed in terms of:

$$\int \frac{C_{\mathrm{I}}(t) - C_{\mathrm{I}}^{*}}{C_{\mathrm{I}}^{*}} dt = \int \frac{D_{\mathrm{B}}(t) - D_{\mathrm{B}}^{*}}{D_{\mathrm{B}}^{*}} dt. \tag{6.18}$$

The left hand side of Eq. 6.18 can be approximated by [78]:

$$\int \frac{C_{\mathrm{I}} - C_{\mathrm{I}}^{*}}{C_{\mathrm{I}}^{*}} dt \approx \frac{R_p Q}{D_{\mathrm{I}} C_{\mathrm{I}}^{*}}, \tag{6.19}$$

where R_p is the projected range of the implant and Q is the dose of interstitials due to the implant (assuming a +1 model this is equivalently to the boron dose). D_{I} and C_{I}^{*} are the equilibrium I diffusivity and I concentration respectively. The idea is to estimate the TED time as the time it takes for the dose Q of interstitials located at a depth R_p to diffuse to the surface in order to reestablish C_{I}^{*}. The right hand side of Eq. 6.18 is directly related to $(Dt)_{\mathrm{TED}}$, which is often used as a measure of TED:

$$(Dt)_{\mathrm{TED}} = \int (D_{\mathrm{B}}(t) - D_{\mathrm{B}}^{*}) dt. \tag{6.20}$$

Combining these relations leads to:

$$(Dt)_{\mathrm{TED}} = R_p Q \frac{D_{\mathrm{B}}^{*}}{D_{\mathrm{I}} C_{\mathrm{I}}^{*}}. \tag{6.21}$$

Since we determined the stress effects of D_{B}^{*} and $D_{\mathrm{I}} C_{\mathrm{I}}^{*}$, we now can also determine the relative change of TED in the presence of stress using Eq. 6.21. The ratio of $D_{\mathrm{B}}^{*}/D_{\mathrm{I}} C_{\mathrm{I}}^{*}$ determines the stress effect on TED. In the case of biaxial strain, there

are both in-plane (lateral) and out-of-plane (vertical) diffusion directions. In both cases we assume that the total TED time is determined by the vertical diffusion of interstitials to the surface.

$$\begin{aligned} \mathrm{TED}_{\mathrm{lateral}} &= \left(\frac{D_{\mathrm{B}}^{*}(\epsilon)_{\mathrm{lateral}}}{D_{\mathrm{I}}C_{\mathrm{I}}^{*}(\epsilon)_{\mathrm{vertical}}}\right) / \left(\frac{D_{\mathrm{B}}^{*}(0)_{\mathrm{lateral}}}{D_{\mathrm{I}}C_{\mathrm{I}}^{*}(0)_{\mathrm{vertical}}}\right) \\ \mathrm{TED}_{\mathrm{vertical}} &= \left(\frac{D_{\mathrm{B}}^{*}(\epsilon)_{\mathrm{vertical}}}{D_{\mathrm{I}}C_{\mathrm{I}}^{*}(\epsilon)_{\mathrm{vertical}}}\right) / \left(\frac{D_{\mathrm{B}}^{*}(0)_{\mathrm{vertical}}}{D_{\mathrm{I}}C_{\mathrm{I}}^{*}(0)_{\mathrm{vertical}}}\right) \end{aligned} \tag{6.22}$$

$\mathrm{TED}_{\mathrm{lateral}}$ and $\mathrm{TED}_{\mathrm{vertical}}$ are the TED enhancement factors in respect to unstrained Si for the two different directions. In the case of 1 % biaxial strain at 1000 °C the results for the individual components are determined using the relations in Eq. 6.11. Combining the results leads to an enhancement of lateral TED by a factor of 3.39, whereas vertical TED is predicted to be enhanced by a factor of 2.15.

6.5 Summary and conclusion

We used *ab-initio* calculations to investigate the effect of stress on point-defect and dopant diffusivities. The methodology introduced in Chapter 5 was extended to also treat stress effects on diffusivities under arbitrary strain states. Vacancy diffusion showed enhancement under compressive strain, whereas interstitials showed the opposite behavior. Tensile strain enhanced I diffusion. The calculations also showed a strong anisotropy in the case of I diffusion under biaxial strain. The enhancement for in-plane (lateral) diffusion is larger than for out-of-plane (vertical) diffusion. Similar effects were also seen in the case of B diffusion, with significant implications for controlling channel length and lateral abruptness. Stress appears to have a stronger effect on B diffusion than on interstitials. In addition, we determined the full diffusivity tensor of I and B migration for arbitrary strain conditions. The off-diagonal terms of the I and B diffusivity tensors vanish. The full knowledge of these tensors enables the implementation of local stress effects in 2D and 3D TCAD process simulators.

Chapter 7

STRESS EFFECT ON DOPANT ACTIVATION

When increasing the local dopant concentration, not all dopant atoms are electrically active. Only a fraction of the dopant atoms contribute to the conduction at room temperature. As an example, group III or V dopants located at substitutional lattice sites accept or donate one electron to the Si crystal. Thus every dopant atom ideally contributes one electron or hole to the conduction. However, since dopant atoms usually interact with point-defects forming e.g., charge neutral dopant/defect clusters, not every dopant atom can be considered electrically active. Increasing dopant activation plays a crucial role in meeting the future targets set by the *International Technology Roadmap for Semiconductors* (ITRS) [16] and therefore the continuation of *Moore's* law [1]. The demand for ultra-shallow and highly active junctions in current and future semiconductor devices requires in depth understanding of the dopant activation process under different process conditions, in order to further increase activation at higher doping concentrations. One open question is the effect of stress on the dopant activation behavior. As mentioned earlier, steep doping gradients and hetero-interfaces induce large stresses. On top of this, sometimes stress is induced purposefully to enhance carrier mobility [69, 70, 71]. The effects of stress on both dopant diffusivity and dopant activation are therefore of major importance. In this chapter we develop a model to predict the stress effects on dopant activation. Since boron (B) is currently the most widely used p-type dopant, we focus here on this element. However the effects of stress on the activation behavior of other dopants can be treated in a very similar fashion.

Experiments on stress effects are very difficult and in the case of B diffusion

even lead to contradictory results [29]. We utilize *ab-initio* calculations to predict B solubility under arbitrary strains, which is an extension of our previous work on stress effects on formation and migration of point-defects and B diffusion (Chapters 5 and 6). Our analysis extends beyond simple hydrostatic activation volumes [25] in order to predict anisotropies associated with more complex stress states.

There exists broad agreement that the boron activation process is controlled by the following three mechanisms:

(a) intrinsic boron diffusion,

(b) boron transient enhanced diffusion (TED),

(c) boron-interstitial cluster (BIC) kinetics.

The effect of stress on the intrinsic B diffusivity and boron TED have been discussed in Chapter 6. This chapter focuses on developing a boron solubility model based on BIC energetics. This is the simplest way to predict the effect of stress on B activation without treating all the details of the BIC time evolution during the activation process. Similar to TED, which involves the modeling of interstitial clustering, BIC models are very complicated and involve a large number of B_nI_m clusters. Our goal is to gain insight on the effects of stress on B activation without treating the highly complex dynamics of the activation process, which involve I_n as well as B_nI_m clusters.

In the following section, a boron solubility model for unstrained silicon based on BIC energetics is developed, which gets extended to capture the effects of arbitrary stress states in Section 7.2. Furthermore, the most important parameter of the model, the induced strain due to substitutional boron, is compared to experimental x-ray diffraction data. The chapter is concluded with a summary and conclusion in Section 7.3.

7.1 *Boron activation and solubility*

The diffusion and clustering behavior of B in unstrained silicon has been studied extensively in the past. There exists broad agreement that B-I clusters (BICs) play an important role in the diffusion and activation behavior of B. The key to understand B behavior is to determine the energetics of these clusters. In addition to inverse modeling studies, *ab-initio* calculations have been conducted to determine the structure and formation energies of B_nI_m clusters [79, 80, 81]. Multiple *ab-initio* calculations and inverse modeling results conclude that B_3I is a key cluster, which controls BIC kinetics [79], while $B_{12}I_7$ is reported experimentally to be the building block of the SiB_3 phase [82] and most stable cluster identified [79]. Thus, we use these clusters to model the boron solubility in unstrained silicon and further on extend the analysis including stress dependence. Figures 7.1, 7.2, and 7.3 show the structure of the individual B complexes used in this model. The high symmetry of these clusters ($x \leftrightarrow y \leftrightarrow z$) dramatically simplifies the analysis under stress (see Appendix E).

Earlier work by Sadigh *et al.* [83] reports large B solubility enhancements under compressive biaxial stress primarily attributed to changes of the intrinsic Si carrier concentration n_i. However their analysis implicitly assumes non-degenerate Si, which is not a valid assumption in the B solubility limit. Under such high doping conditions an impurity band gets formed and Si becomes a degenerate semiconductor. In our analysis, we assume the Fermi level to be at the valence band edge, which is a valid assumption for heavily-doped Si.

Figures 7.4, 7.5, and 7.6 show the density of states (DOS) of B_s, B_3I, and $B_{12}I_7$. Although the calculations were performed using neutral super-cells, summing the occupation of the states below the valence band edge shows that the valence band is not completely filled for B_s, B_3I, and $B_{12}I_7$. This in an indication of the charge states of the complexes. In the case of B_s there is one unoccupied state in the valence band. This is the signature of a delocalized hole. Assuming a localized negative charge

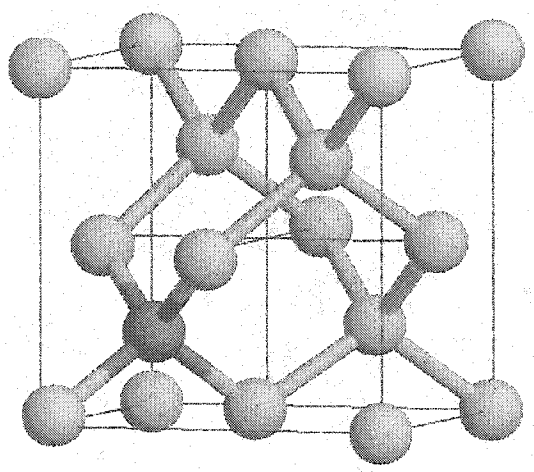

Figure 7.1: Structure of a substitutional B atom in a Si diamond lattice. The B atom is shown in green, whereas the Si atoms are illustrated in yellow.

around the B atom, the neutral super-cell calculation refers to $B_s^- + h^+$ rather than a neutral B_s^0. This analysis is identical to the method discussed in Chapter 3. Summing the DOS for B_3I and $B_{12}I_7$ determines the charge states of these complexes to be B_3I^- and $B_{12}I_7^=$ for a Fermi level at the valence band edge. This is an appropriate assumption near the solubility limit. These results suggest that B_3I and $B_{12}I_7$ are not completely inactive. In the case of B_3I 33 % of the incorporated B is active. The double negatively charged $B_{12}I_7$ includes 17 % active boron. This fact does not impact the B solubility, but need to be considered when calculating the actual active B concentration.

The calculated formation energies of B_3I^- and $B_{12}I_7^=$ in unstrained Si are $-0.10\,\mathrm{eV}$ and $-3.31\,\mathrm{eV}$ respectively (see Tab. 7.1). These energies are in reference to B_s^- and perfect Si. We assume $E_\mathrm{F} = E_\mathrm{V}$ as appropriate for heavily B-doped Si. More details on the convergence of these numbers is included in Appendix G. The formation energy

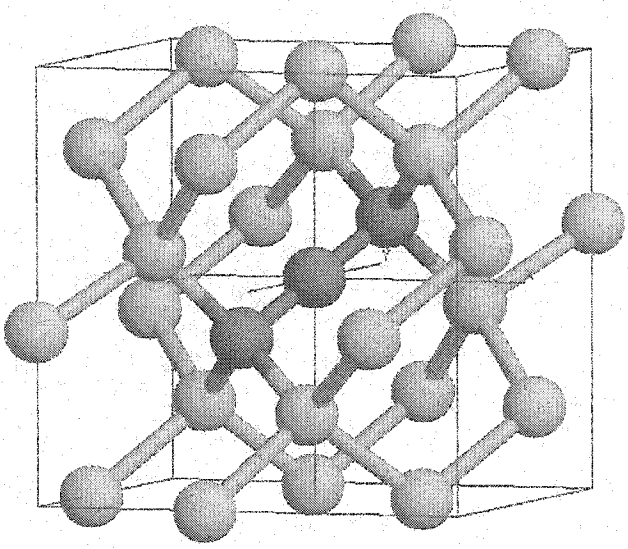

Figure 7.2: Structure of a B_3I cluster in a Si diamond lattice. B atoms are illustrated in green, whereas Si atoms are yellow. The three B atoms are arranged along the <111> direction. Two B atoms reside close to substitutional sites, whereas the third B atom occupies the connecting bond-centered site.

of B_nI_m clusters are defined as:

$$E_f^{B_nI_m} = E_{B_nI_m} - nE_B - \left((n-1) - \frac{m}{N}\right) E_{Si}, \tag{7.1}$$

where $E_{B_nI_m}$, E_B, and E_{Si} are the total energies for the respective super-cells. Si and B have N atoms, whereas B_nI_m has $N+m$ atoms in the super-cell.

In local equilibrium, the formation energies of the different clusters determine the concentration of the clusters B_nI_m for a given boron concentration C_B (see Appendix A):

$$C_{B_nI_m} = \frac{\theta_{B_nI_m}}{\theta_B^n} C_s \left(\frac{C_B}{C_s}\right)^n \exp\left(-\frac{E_f^{B_nI_m}}{kT}\right). \tag{7.2}$$

Adding up the boron concentrations of the different complexes results in the total boron concentration C_B^{tot}, which is just a function of C_B once E_f and θ are known for

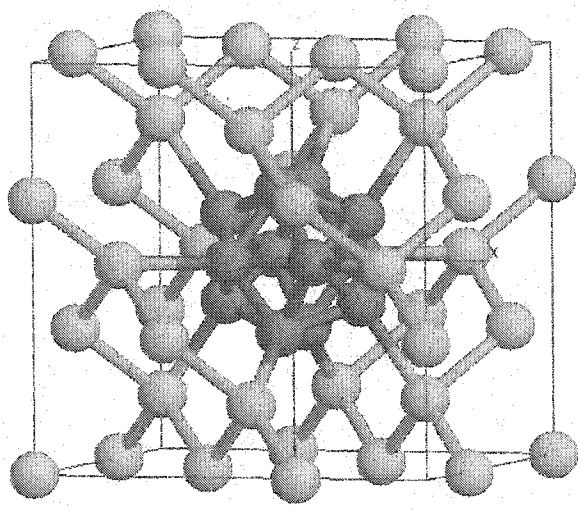

Figure 7.3: Structure of a $B_{12}I_7$ cluster in a Si diamond lattice. B atoms are illustrated in green, whereas Si atoms are yellow. The twelve B atoms are arranged as an icosahedron. $B_{12}I_7$ is the building block of the SiB_3 phase.

Table 7.1: Formation energy for B_s, B_3I and $B_{12}I_7$ in unstrained silicon. The reference configurations are substitutional B and perfect Si. $E_f^{B_nI_m} = E_{B_nI_m} - nE_B - ((n-1) - m/N)\,E_{Si}$, where Si has N atoms, and B_nI_m has $N+m$ atoms in the super-cell. We assume $E_F = E_V$ as appropriate for heavily B-doped Si. The reported numbers include a correction due to the finite **k**-point sampling, which is discussed in Appendix D.

Complex	E_f [eV]
B_s^-	+0.00
B_3I^-	−0.10
$B_{12}I_7^=$	−3.31

the different clusters:

$$C_B^{tot}(C_B) = C_B + \sum_{n=2}^{\infty} n\, C_{B_nI_m}(C_B). \tag{7.3}$$

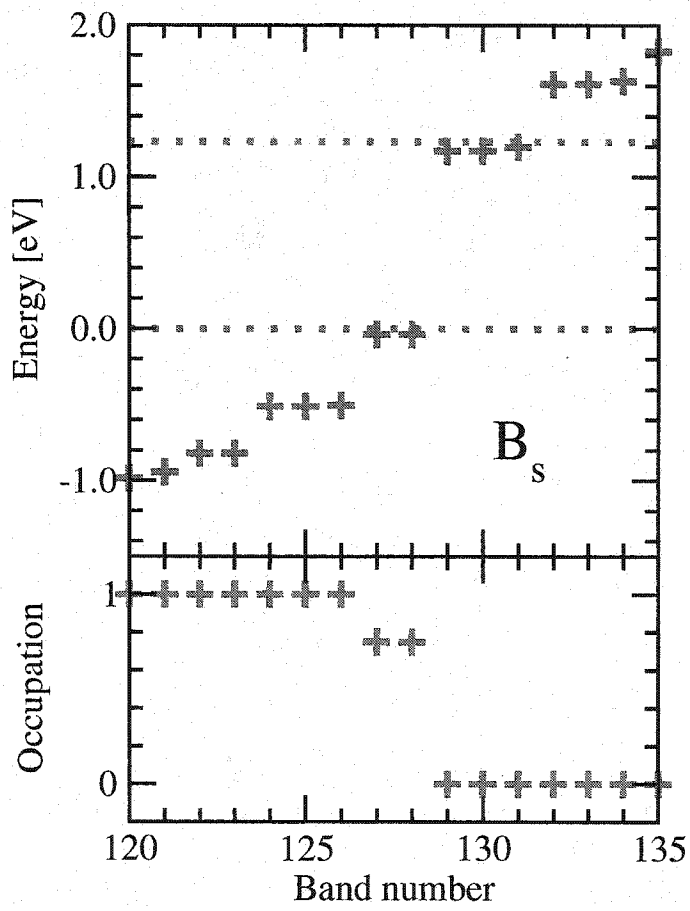

Figure 7.4: DOS of B_s and 63 Si atoms in a neutral super-cell (255 electrons). The green (dashed) lines indicate the locations of the valence and conduction band of Si at $\pi/(4\,b)\,(1,1,1)$ in the first Brillouin zone (BZ) respectively. $b = 5.4578\,\text{Å}$ is the GGA lattice constant of unstrained Si. Since the calculation was performed using 2^3 Monkhorst-Pack **k**-point sampling (4 irreducible **k**-points) including spin, every state is 8-fold degenerate. The total number of electrons N is determined by $N = \sum_i (1/4 \sum_{j=1}^{8} n_{ij})$. 1/4 is the weighting factor due to the **k**-point sampling and n_{ij} is the occupation. i runs over all bands. All energies are reported with respect to the valence band edge of Si.

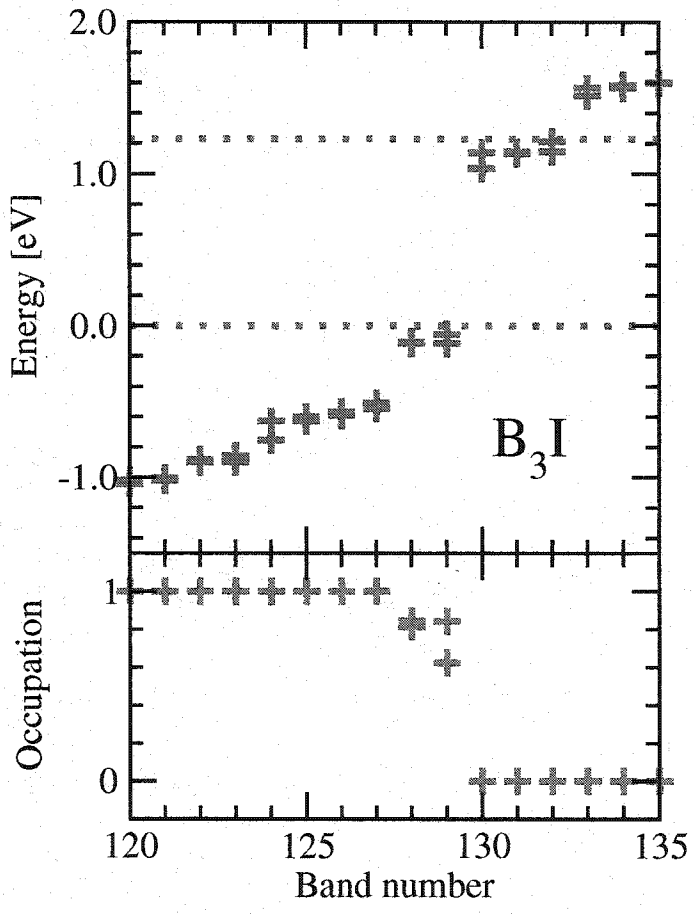

Figure 7.5: DOS of B_3I and 62 Si atoms in a neutral super-cell (257 electrons). The green (dashed) lines indicate the locations of the valence and conduction band of Si at $\pi/(4\,b)\,(1,1,1)$ in the first Brillouin zone (BZ) respectively. $b = 5.4578\,\text{Å}$ is the GGA lattice constant of unstrained Si. Since the calculation was performed using 2^3 Monkhorst-Pack **k**-point sampling (4 irreducible **k**-points) including spin, every state is 8-fold degenerate with the exception of the states in band 128 and 129. Each of these have a 4-fold degeneracy. The total number of electrons N is determined by $N = \sum_i (1/4 \sum_{j=1}^{8} n_{ij})$. 1/4 is the weighting factor due to the **k**-point sampling and n_{ij} is the occupation. i runs over all bands. All energies are reported with respect to the valence band of Si.

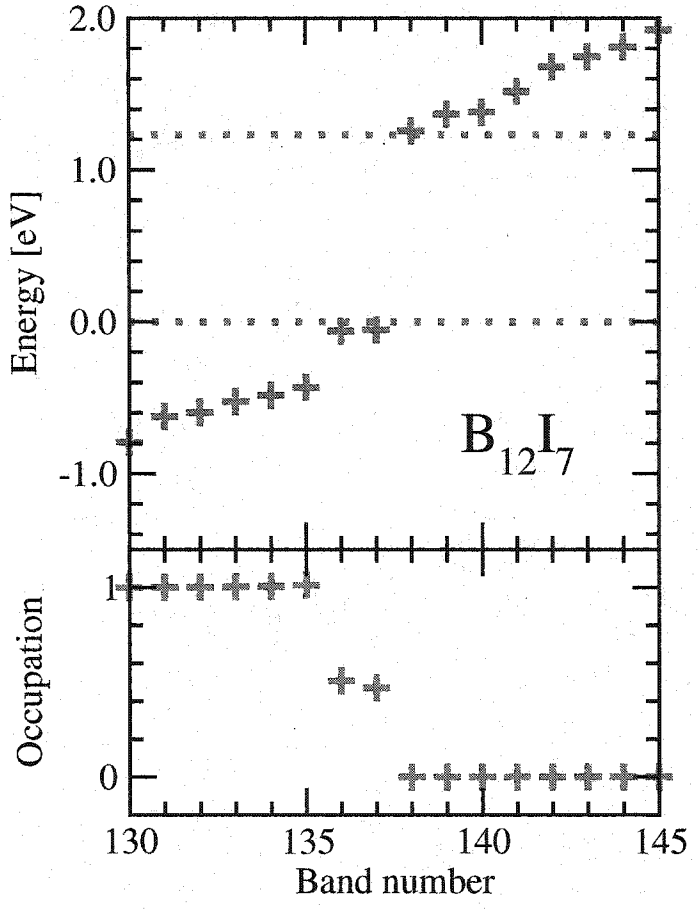

Figure 7.6: DOS of a icosahedron $B_{12}I_7$ cluster and 59 Si atoms in a neutral super-cell (272 electrons). The green (dashed) lines indicate the locations of the valence and conduction band of Si at $\pi/(4\,b)\,(1,1,1)$ in the first Brillouin zone (BZ) respectively. $b = 5.4578\,\text{Å}$ is the GGA lattice constant of unstrained Si. Since the calculation was performed using 2^3 Monkhorst-Pack **k**-point sampling (4 irreducible **k**-points) including spin, every state is 8-fold degenerate. The total number of electrons N is determined by $N = \sum_i (1/4 \sum_{j=1}^{8} n_{ij})$. 1/4 is the weighting factor due to the **k**-point sampling and n_{ij} is the occupation. i runs over all bands. All energies are reported with respect to the valence band of Si.

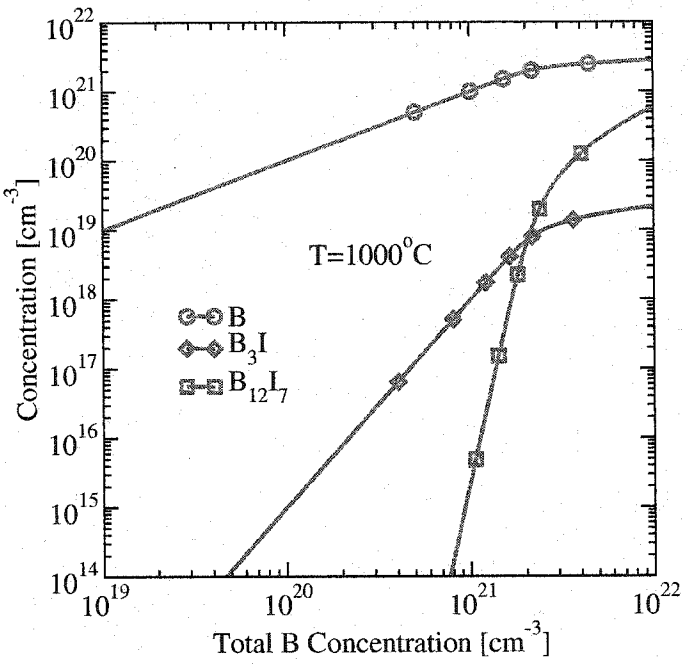

Figure 7.7: Local equilibrium concentration of B, B_3I, and $B_{12}I_7$ as a function of total B concentration in unstrained Si at $T = 1000\,°C$

Here we only consider three clusters B, B_3I, and $B_{12}I_7$, hence:

$$C_B^{tot}(C_B) = C_B + 3\,C_{B_3I}(C_B) + 12\,C_{B_{12}I_7}(C_B). \tag{7.4}$$

θ_B, θ_{B_3I}, and $\theta_{B_{12}I_7}$ are the configurational entropy factor $S = k \ln\theta$ for B_s, B_3I, and $B_{12}I_7$. For a fixed total boron concentration C_B^{tot}, Eq. 7.4 can be solved for C_B. Figure 7.7 illustrates the result at $T = 1000\,°C$. The graph shows that for $C_B^{tot} > 10^{21}\,cm^{-3}$, C_B is a very weak function of C_B^{tot}. This is an indication that the B solubility is reached. Adding additional B to the system leads primarily to an increase in the $B_{12}I_7$ concentration. Since $B_{12}I_7$ is the building block of the SiB_3 phase, this behavior can be viewed as approximating the formation of boron precipitates. Therefore the solubility can be predicted as $C_{ss} \approx C_B$ for large enough C_B^{tot}. The effect of B_3I on C_{ss} is rather weak in comparison to $B_{12}I_7$.

7.2 *Stress effect on boron solubility*

The solubility model introduced in the previous section depends only on the formation energies of the different B_nI_m clusters and can be extended to arbitrary stress states once the stress effect on the formation energy is known. Following the methodology of Chapter 5, the energy of a B_nI_m clusters in an arbitrary strain state can be written as a function of the elasticity tensor and induced strain:

$$E_{B_nI_m}(\vec{\epsilon}) = E_0^{B_nI_m} + \frac{\Omega}{2}\left(\vec{\epsilon} - x\Delta\vec{\epsilon}^{B_nI_m}\right)\left(\mathbf{C}^{Si} + x\Delta\mathbf{C}^{B_nI_m}\right)\left(\vec{\epsilon} - x\Delta\vec{\epsilon}^{B_nI_m}\right), \quad (7.5)$$

where Ω is the volume of the super-cell, $x = C_{B_nI_m}/C_S$ denotes the relative complex concentration, $\Delta\vec{\epsilon}^{B_nI_m}$ is the induced strain, and $\mathbf{C}^{Si}+x\Delta\mathbf{C}^{B_nI_m}$ is the elasticity tensor of the super-cell. In this work, $x = 1/64$ since our super-cell contains 64 Si lattice sites. Thus, once the elastic constants and induced strains for a given equilibrium structure are known, the change in formation E_f can be calculated, which leads directly to modified equilibrium concentrations. To account for the change in formation energy due to stress, the elasticity tensors $\mathbf{C}$ and induced strains $\Delta\vec{\epsilon}$ are calculated for B_s, B_3I, and $B_{12}I_7$. Figure 7.8 shows the energy vs. hydrostatic and uniaxial strain for the complexes of interest. The high symmetry of these clusters ($x \leftrightarrow y \leftrightarrow z$) dramatically simplifies the analysis under stress (see Appendix E). Table 7.2 lists the extracted parameters.

Substitutional B exhibits a rather large induced strain of -0.327, or a total induced volume change of $0.981\,\Omega_0$ (almost a full atomic volume). Due to this large induced strain, the Si lattice parameter is expected to be a strong function of the B concentration. Figure 7.9 shows a comparison of various experimental data with this work. Our calculated value agrees well with the experimental measurements.

In the dilute limit, the change in formation energy of the various clusters can be derived using Eq. 7.5 as:

$$\Delta E_f^{B_nI_m} = -\Omega_0\left(\Delta\vec{\epsilon}^{B_nI_m} - n\Delta\vec{\epsilon}^{B_s}\right)\mathbf{C}^{Si}\vec{\epsilon} + \frac{\Omega_0}{2}\vec{\epsilon}\left(\Delta\mathbf{C}^{B_nI_m} - n\Delta\mathbf{C}^{B_s} - m\mathbf{C}^{Si}\right)\vec{\epsilon}. \quad (7.6)$$

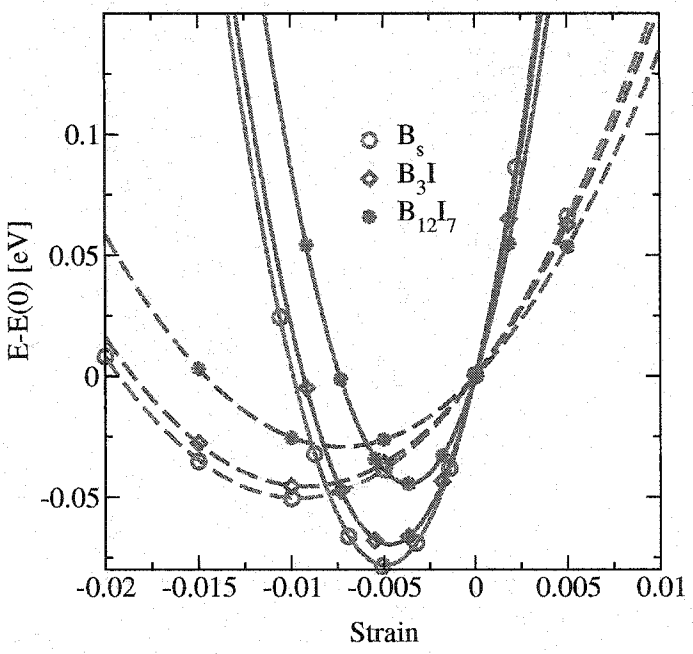

Figure 7.8: Energy vs. hydrostatic (solid lines) and uniaxial strain (dashed lines) for B_s, B_3I, and $B_{12}I_7$. All energies are reported with respect to their values in unstrained Si. Due to the symmetry of the complexes ($x \leftrightarrow y \leftrightarrow z$) the induced strain $\Delta\epsilon$ is the shift of the minimum from $\epsilon = 0$ (unstrained Si) under hydrostatic strain. ΔC_{11} and ΔC_{12} are determined from the curvatures. The data shown corresponds to a 64 atom super-cell calculation. $\epsilon = 0$ response to the GGA Si lattice constant $b_{\mathrm{Si}} = 5.4578\,\text{Å}$. The extracted values are listed in Table 7.2.

Table 7.2: Induced strain $\Delta\epsilon$ and ΔC_{ij} for B_s, B_3I, and $B_{12}I_7$ extracted from Fig. 7.8, assuming $C_{11}^{\mathrm{Si}} = 155\,\text{GPa}$ and $C_{12}^{\mathrm{Si}} = 54\,\text{GPa}$ for pure Si. Strains are reported with respect to the GGA lattice parameter $b_{\mathrm{Si}} = 5.4578\,\text{Å}$. Appendix G discusses the convergence of these parameters.

Complex	$\Delta\epsilon$	ΔC_{11} [GPa]	ΔC_{12} [GPa]
B_s	-0.327	-260	129
B_3I	-0.299	-465	220
$B_{12}I_7$	-0.236	-614	510

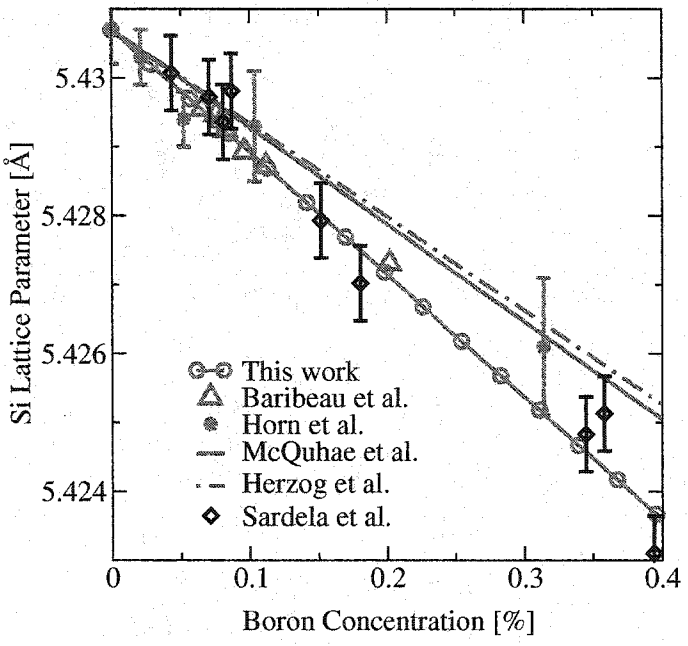

Figure 7.9: Comparison of experimental data [15] with our *ab-initio* results for the Si lattice parameter as a function of B concentration. Theoretically the Si lattice constant can be expressed in terms of the induced strain $\Delta\epsilon$ (see Table 7.2) of substitutional B and the fractional B concentration $x = C_B/C_S$ as $b = (1 + x\Delta\epsilon)b_{Si}$, where a_{Si} is the lattice parameter of bulk Si. $\Delta\epsilon = -0.327$ corresponds to a lattice contraction coefficient $\beta = 6.54 \times 10^{-24}\,\mathrm{cm}^3$. Sardela *et al.* report $\beta = (6.3 \pm 0.1) \times 10^{-24}\,\mathrm{cm}^3$ based on active B concentration. For other experiments, cluster formation at high B concentration may lead to lower strain levels.

Ω_0 is the volume of a single Si atom. For small strains, the linear strain term is dominant; even at 1 % strain the quadratic term gives rise to only moderate contributions for large clusters like $B_{12}I_7$. Equation 7.6 also indicates that large strain effects are expected for B rich clusters due to the relative induced strain $\Delta\vec{\epsilon}^{B_nI_m} - n\Delta\vec{\epsilon}^{B_s}$. A similar effect also exists for the quadratic term due to $\Delta\mathbf{C}^{B_nI_m} - n\Delta\mathbf{C}^{B_s} - m\mathbf{C}^{Si}$.

Due to the symmetry of the B_s, B_3I, and $B_{12}I_7$, the induced strains can be directly extracted from hydrostatic strain calculations (see Appendix E). Furthermore, the respective elasticity tensors can be expressed in terms of only two independent pa-

rameters: C_{11} and C_{12}. Since the bulk modulus $K = 1/3(C_{11} + 2C_{12})$, calculations of only the hydrostatic and uniaxial strain case are required to fully describe the elastic behavior of the system. For biaxial strain $\vec{\epsilon} = (\epsilon, \epsilon, -\tilde{\nu}\epsilon)$ (see Appendix E) Eq. 7.6 becomes:

$$\begin{aligned} \Delta E(\epsilon)_f^{B_3I} &= -29.65\epsilon + 36.25\epsilon^2, \\ \Delta E(\epsilon)_f^{B_{12}I_7} &= -160.33\epsilon + 294.67\epsilon^2. \end{aligned} \tag{7.7}$$

Figure 7.10 shows the enhancement of the boron solubility as a function of biaxial strain for different temperatures. Our calculations predict strongly enhanced activation for compressive biaxial stress, while tensile biaxial stress reduces the B solubility and this increases sheet resistance.

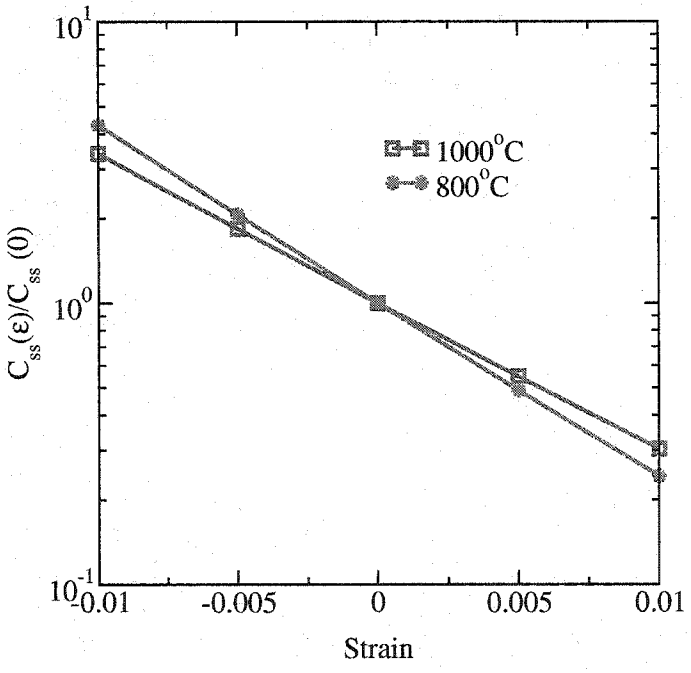

Figure 7.10: Predicted boron solubility enhancement as a function of biaxial strain for various temperatures. Positive strains are tensile.

The rather moderate induced strain of B_3I and $B_{12}I_7$ indicates that enhancement

of B solubility under stress is mainly due to the large induced strain of B_s. If one assumes that in the solubility limit only one large B_nI_m cluster dominates Eq. 7.3, the total B concentration can be approximated by:

$$C_{\mathrm{B}}^{tot} \approx n\, C_s \left(\frac{C_{\mathrm{B}}}{C_s}\right)^n \exp\left(-\frac{E_f^{\mathrm{B}_n\mathrm{I}_m}}{kT}\right). \tag{7.8}$$

Entropy difference are neglected here. Assuming $C_{ss} \approx C_B$, Eq. 7.8 determines C_{ss}:

$$C_{ss} \approx C_s \left(\frac{C_{\mathrm{B}}^{tot}}{n\, C_s}\right)^{1/n} \exp\left(\frac{E_f^{\mathrm{B}_n\mathrm{I}_m}}{n\, kT}\right). \tag{7.9}$$

The solubility enhancement under strain takes on a very simple form:

$$\frac{C_{ss}(\vec{\epsilon})}{C_{ss}(0)} = \exp\left(\frac{\Delta E_f^{\mathrm{B}_n\mathrm{I}_m}(\vec{\epsilon})}{n\, kT}\right). \tag{7.10}$$

$\Delta E_f^{\mathrm{B}_n\mathrm{I}_m}$ is given by Eq. 7.6. Dropping the quadratic strain term in Eq. 7.6 leads to:

$$\frac{C_{ss}(\vec{\epsilon})}{C_{ss}(0)} = \exp\left(\frac{-\Omega_0(\Delta E_f^{\mathrm{B}_n\mathrm{I}_m}/n - \Delta E_f^{\mathrm{B}_s})\mathbf{C}^{\mathrm{Si}}\vec{\epsilon}}{kT}\right) \approx \exp\left(\frac{\Omega_0 \Delta E_f^{\mathrm{B}_s}\mathbf{C}^{\mathrm{Si}}\vec{\epsilon}}{kT}\right), \tag{7.11}$$

where we dropped the term $\Delta E_f^{\mathrm{B}_n\mathrm{I}_m}/n$ for large n. The solubility enhancement now depends only on the induced strain of B_s. Figure 7.11 shows a comparison of this simplified model with the prediction using B_s, B_3I, and $B_{12}I_7$ (see Fig. 7.10). There is almost no difference between the predictions of the two models, which confirms that the dominant stress effect on B solubility is the large induced strain of B_s.

7.3 Summary and conclusion

Stress effects on dopant diffusion and activation are of critical interest in current and future CMOS devices. Since experiments are very difficult to perform, we utilized *ab-initio* calculations to predict the effect of stress on B solubility. We find strongly enhanced solubility under compressive biaxial stress, whereas tensile biaxial stress leads to a reduction. In contrast to other work [83], the enhancement/reduction is primarily due to the size effect of substitutional B which is confirmed by the excellent

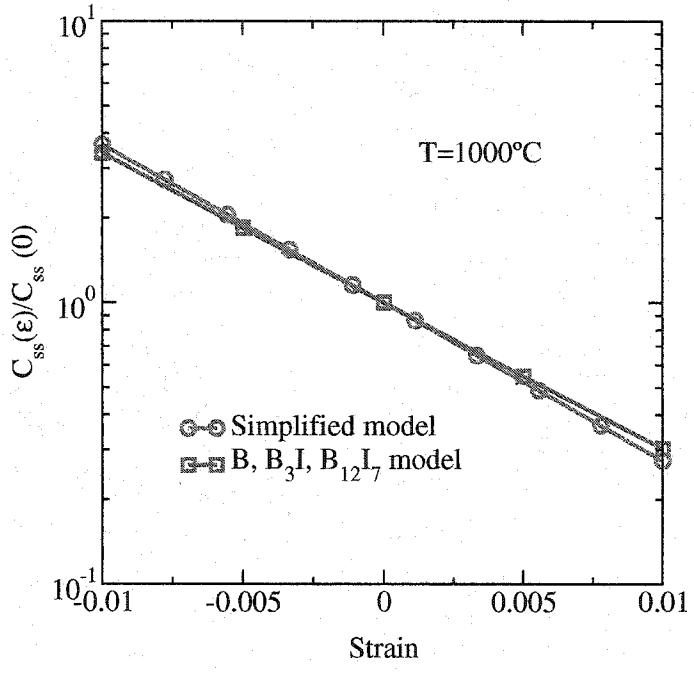

Figure 7.11: Comparison of stress effect on B solubility under biaxial strain using the simplified solubility model of Eq. 7.11 with the more extended model including B_s, B_3I, and $B_{12}I_7$ shown in Fig. 7.10.

agreement of calculated B strain relaxation effect with various x-ray diffraction data. Measurements in different SiGe alloys also support our predictions, as there is experimental evidence that B solubility is enhanced in compressively strained SiGe on Si films with increasing Ge content [84]. This work suggests that stress effects play a major role in modifying B solubility/segregation in SiGe versus Si.

Chapter 8

SUMMARY AND SUGGESTIONS FOR FUTURE WORK

In this dissertation, we described how *ab-initio* calculations can be used to develop physical models of diffusion and activation in silicon. A hierarchy of approaches (*ab-initio*, kinetic lattice Monte Carlo, continuum) was used to bridge the gaps in time scale and system size between atomistic calculations and nanoscale devices. The *ab-initio* modeling approach introduced in Chapter 2 was applied to two very different challenges in process technology: F co-implantation and stress effects on dopant diffusion and activation.

The following sections give short lists of the main accomplishments of this dissertation, followed by more details regarding individual contributions. This chapter closes with suggestions for future work and a final conclusion.

8.1 Main contributions of fluorine study

(a) Found strong interaction of F with vacancies which leads to F decoration of dangling bonds associated with vacancies and vacancy clusters.

(b) Explained anomalous F redistribution behavior based on F vacancy interactions.

(c) Explained interactions of F with other dopants (B and P) with respect to dopant diffusion and activation (F interacts indirectly by modifying local point-defect concentrations).

In Chapters 3 and 4, *ab-initio* calculations were used to understand anomalous F

diffusion behavior (Chapter 3), which has been a mystery for a decade. Strongly bound F_nV_m clusters are the key to understanding the anomalous redistribution behavior reported by Jeng *et al.* [3]. Fast diffusing F_i decorate V_n forming immobile F_nV_m clusters. At higher temperatures, these clusters are annihilated by I. This leads to the surface driven uphill diffusion phenomenon: F decoration of V leads to F dissolving from deeper regions (I excess) and accumulation near surface (V excess).

The revealed interaction of F with point-defects also explains the benefits of F co-implantation for B and P activation and diffusion. Based on the insight gained from first-principles, a simplified F diffusion model at the continuum level was extracted (Chapter 4), that accounts for co-implantation effects on B and P for various implant energies and doses. The analysis predicts the F effect on B and P to be entirely due to interactions of F with point-defects. Fluorine alters the local point-defect concentration due to the formation and dissolution of energetically favored F_nV_m clusters and therefore indirectly impacts the point-defect mediated diffusion behavior of B and P. The depth of the amorphous-crystalline interface and the implant depth of fluorine are the key parameters to understanding the effects on dopant redistribution. Under sub-amorphizing conditions, B and P diffusion are enhanced due to increased I concentrations, in contrast to amorphized regions where the model correctly predicts retarded diffusion due to the additional vacancies grown in originally as F_nV_m clusters. This model has been implemented in the commercially available TCAD process simulators TSUPREM4 [43] and ISE-FLOOPS [44].

8.2 Main contributions of stress effect study

(a) Developed new methodology to treat stress effects on formation and migration energies of point-defects/dopants.

(b) Calculated stress effects on equilibrium concentration and diffusion of point-defects.

(c) Found strong anisotropic diffusion for interstitials and boron.

(d) Found large enhancement of B solubility under compressive strain.

Chapters 5, 6, and 7 addressed the effect of stress on point-defect/dopant equilibrium concentration, diffusion, and activation. After developing a general methodology to treat stress effects from first-principles (Chapter 5), *ab-initio* techniques were used to extract induced strains and elasticity tensor for various defects and impurities in order to predict the impact of arbitrary stress tensors (i.e., not just hydrostatic case). The results from first-principles calculations were used to quantify both analytically as well as using kinetic lattice Monte Carlo simulations the full diffusivity tensor of I and B (Chapter 6). The result is a prediction of strong anisotropic diffusion of B (as well as I) under biaxial strain. In Chapter 7, the effects of stress on B activation were investigated. Following the methodology in Chapter 5, a stress dependent B solubility model was developed that predicts large enhancements of B solubility under compressive stress conditions with corresponding solubility reduction for tensile stress.

8.3 Suggestions for future work

The incorporation of biaxial strain in order to improve mobility has become a central part of the strategy for CMOS device scaling. In this work, we developed a methodology in Chapters 5, 6, and 7 to treat stress effects on dopant diffusion and activation and applied it to single intrinsic point-defects as well as B systems. With this methodology in place, it is straightforward to extend this work to other dopants such as P, As, and Sb and investigate the stress effects on diffusion and activation. Preliminary work on As found symmetric transition states for both migration mechanisms (vacancy-assisted and interstitial-assisted) which suggests isotropic diffusion under arbitrary strain conditions. For As activation, As_4V is believed to be responsible for As deactivation [85]. Thus, stress effects on As activation can be investigated by de-

termining the stress dependence of the As_4V formation energy. Since single/extended intrinsic point-defects are the key to understanding the dynamic processes like TED and activation, a similar approach can be used to calculate the stress/strain dependence of extended point-defect formation. Of particular interest are dopant/defect clusters which limit dopant activation (e.g., B/I and As/V clusters) and point-defect clusters which control TED (I, V clusters, {311} defects, loops).

As shown in Chapters 3 and 4 fluorine co-implantation is an effective tool to reduce B and P diffusion and enhance activation. This approach can be extended to incorporation of other impurities via implantation or growth. Of particular interest are group IV elements such as C, Ge, Sn, and Pb, since they are compatibility with the Si electronic and lattice structure. However due to their size mismatch, large induced strains can be anticipated. Since it has been shown in the previous chapters that the large stress effects for B diffusion and activation arose from the large negative induced strain of substitutional B, it is interesting to look into strain compensation effects of for example group IV elements with dopants in order to identify the most promising species for co-implantation and/or co-doping. Furthermore, using *ab-initio* calculations cluster binding energies across a wide range of impurities (e.g., F, Cl, N, O, C, Sn, Pb) with dopants and defects (I and V) can be explored. The aim is to explore activity enhancement and diffusion reduction via two mechanisms: formation of stable active complexes and point-defect engineering.

8.4 Final conclusion

In conclusion, we have demonstrated in this thesis that the *ab-initio* modeling approach is an extremely powerful tool to identify diffusion/reaction mechanisms (e.g., F study) and that it can be used to address phenomena which are experimentally difficult to access (e.g., stress effects on point-defect/dopant diffusion and activation). Overall, *ab-initio* calculations have a special role as the foundation in the modeling

hierarchy. However, future challenges in VLSI technology will require utilization of all tools of the modeling hierarchy in addition to experiments.

BIBLIOGRAPHY

[1] G. E. Moore, Electronics **38** (1965).

[2] G. E. Moore, in *International Solid State Circuits Conference (ISSCC)* (2003).

[3] S.-P. Jeng, T.-P. Ma, R. Canteri, M. Anderle, and G. W. Rubloff, Appl. Phys. Lett. **61**, 1310 (1992).

[4] R. Hull, *Properties of crystalline silicon* (IEEE, 1999), p. 383.

[5] A. L. Smith, S. T. Dunham, and L. C. Kimerling, Physica B **273-274**, 358 (1999).

[6] P. Fastenko, S. T. Dunham, and S. Chakravarthi, presented at 2002 MRS Spring Meeting, San Francisco, CA (2002).

[7] *UT-Marlowe 5.1*, University of Texas at Austin (2001).

[8] S. Chakravarthi *et al.*, Texas Instruments Inc. (2002), personal communication.

[9] *VASP the GUIDE*, Institut für Materialphysik. Universität Wien (2001), URL `http://cms.mpi.univie.ac.at/vasp/`.

[10] H. Jónsson, G. Mills, and K. W. Jacobsen, *Classical and Quantum Dynamics in Condensed Phase Simulations* (World Scientific, Singapore, 1998), p. 385.

[11] G. Henkelman and H. Jónsson, J. Chem. Phys. **113**, 9978 (2000).

[12] G. Henkelman, B. P. Uberuaga, and H. Jónsson, J. Chem. Phys. **113**, 9901 (2000).

[13] P. Kuo, J. L. Hoyt, J. F. Gibbons, J. E. Turner, and D. Lefforge, Appl. Phys. Lett. **66**, 580 (1995).

[14] Y. Zhao, M. J. Aziz, H.-J. Gossmann, S. Mitha, and D. Schiferl, Appl. Physics Lett. **74**, 31 (1999).

[15] M. R. Sardela, H. H. Radamson, J. O. Ekberg, J.-E. Sundgren, and G. V. Hansson, Semicond. Sci. Technol. **9**, 1272 (1994).

[16] *International Technology Roadmap of Semiconductors*, SEMATECH (2004), URL `http://www.sematech.org`.

[17] J. D. Plummer, M. D. Deal, and P. B. Griffin, *Silicon VLSI Technology: Fundamentals, Practice, and Modeling* (Prentice Hall, Upper Saddle River, NJ, 2000).

[18] P. M. Fahey, P. B. Griffin, and J. D. Plummer, Rev. Mod. Phys. **61**, 289 (1989).

[19] J. P. Perdew, K. Burke, and M. Ernzerhof, Phys. Rev. Lett. **77**, 3865 (1996).

[20] M. Navi and S. T. Dunham, J. Electrochem. Soc. **145**, 2545 (1998).

[21] Texas Instruments Inc. (2004), URL `http://www.ti.com`.

[22] C. G. Van de Walle, F. R. McFeely, and S. T. Pantelides, Phys. Rev. Lett. **61**, 1867 (1988).

[23] A. Taguchi and Y. Hirayama, Solid State Commun. **116**, 595 (2000).

[24] N. E. B. Cowern, P. C. Zalm, P. van der Sluis, D. J. Gravesteijn, and W. B. de Boer, Phys. Rev. Lett. **72**, 2585 (1994).

[25] M. J. Aziz, Appl. Phys. Lett. **70**, 2810 (1997).

[26] B. Sadigh, T. J. Lenosky, S. K. Theiss, M.-J. Caturla, T. Diaz de la Rubia, and M. A. Foad, Phys. Rev. Lett. **83**, 4341 (1999).

[27] M. J. Aziz, Materials Science in Semiconductor Processing **4**, 397 (2001).

[28] M. Laudon, N. N. Carlson, M. P. Masquelier, M. S. Daw, and W. Windl, Appl. Phys. Lett. **78**, 201 (2001).

[29] M. S. Daw, W. Windl, N. N. Carlson, M. Laudon, and M. P. Masquelier, Phys. Rev. B **64**, 045205 (2001).

[30] N. W. Ashcroft and N. D. Mermin, *Solid State Physics* (Harcourt College, 1976).

[31] Y. Taur and T. H. Ning, *Fundamentals of modern VLSI devices* (Cambridge University Press, Cambrige, UK, 1998).

[32] M. E. Glicksman, *Diffusion in solids: Field theory, solid-state principles, and applications* (John Wiley, 2000).

[33] F. H. Stillinger and T. A. Weber, Phys. Rev. B **31**, 5262 (1985).

[34] J. Tersoff, Phys. Rev. B **39**, 5566 (1989).

[35] A. B. Bortz, M. H. Kalos, and J. L. Lebowitz, J. Comput. Phys. **17**, 10 (1975).

[36] A. Voter, Phys. Rev. B **34**, 6819 (1986).

[37] A. Voter, Phys. Rev. Lett. **78**, 3908 (1997).

[38] A. F. Voter, Phys. Rev. B **57**, R13985 (1998).

[39] M. R. Sorensen and A. F. Voter, J. Chem. Phys. **112**, 9599 (2000).

[40] G. Henkelman and H. Jónsson, J. Chem. Phys. **115**, 9657 (2001).

[41] G. Henkelman and H. Jonsson, Phys. Rev. Lett. **90**, 116101 (2003).

[42] S. C. Jain, W. Schoenmaker, R. Lindsay, P. A. Stolk, S. Decoutere, M. Willander, and H. E. Maes, J. Appl. Phys. **91**, 8919 (2002).

[43] *TSUPREM-4 User's Manual Version 2001.4*, Synopsis (2001).

[44] *ISE-FLOOPS*, Integrated System Engineering (ISE) (2003), URL `http://www.ise.com`.

[45] Z. Qin, Ph.D. thesis, University of Washington, Seattle, WA (in preparation) (2004).

[46] B. P. Uberuaga, Ph.D. thesis, University of Washington, Seattle, WA (2000).

[47] F. Aryasetiawan and O. Gunnarsson, Rep. Prog. Phys. **61**, 237 (1998).

[48] P. Hohenberg and W. Kohn, Phys. Rev. **136**, B864 (1964).

[49] M. Levy, Proc. Natl. Acad. Sci. (USA) **76**, 6062 (1979).

[50] W. Kohn and L. J. Sham, Phys. Rev. **140**, A1133 (1965).

[51] J. P. Perdew, J. A. Chevary, S. H. Vosko, K. A. Jackson, M. R. Pederson, D. J. Singh, and C. Fiolhais, Phys. Rev. B **46**, 6671 (1992).

[52] G. F. Bertsch, *Introduction to density functional theory* (2001), URL `http://www.phys.washington.edu/bertsch/`.

[53] R. O. Jones and O. Gunnarsson, Rev. Mod. Phys. **61**, 689 (1989).

[54] R. G. Parr and W. Yang, *Density Functional Theory ot Atoms and Molecules* (Oxford University Press, New York, 1989).

[55] G. Henkelman and H. Jónsson, J. Chem. Phys. **111**, 7010 (1999).

[56] T. H. Huang, H. Kinoshita, and D. L. Kwong, Appl. Phys. Lett. **65**, 1829 (1994).

[57] J. Park and H. Hwang, in *Mater. Res. Soc. Symp. Proc.* (MRS, Warrendale, PA, 1999), vol. 568, p. 71.

[58] D. F. Downey, J. W. Chow, E. Ishida, and K. S. Jones, Appl. Phys. Lett. **73**, 1263 (1998).

[59] L. S. Robertson, P. N. Warnes, K. S. Jones, S. K. Earles, M. E. Law, D. F. Downey, S. Falk, and J. Liu, in *Mater. Res. Soc. Symp. Proc.* (MRS, Warrendale, PA, 2000), vol. 610, p. B4.2.1.

[60] H. W. Kennel, S. M. Cea, A. D. Lilak, P. H. Keys, M. D. Giles, J. Hwang, J. S. Sandford, and S. Corcoran, in *2002. IEDM '02 Digest. International Electron Devices Meeting, 8-11 Dec. 2002* (IEEE, Piscataway, NY, 2002), p. 875.

[61] G. Kresse and J. Hafner, Phys. Rev. B **47**, 558 (1993).

[62] G. Kresse and J. Furthmüller, Phys. Rev. B **54**, 11169 (1996).

[63] D. Vanderbilt, Phys. Rev. B **41**, 7892 (1990).

[64] G. Kresse and J. Hafner, J. Phys. Condens. Matter **6**, 8245 (1994).

[65] B. R. Weinberger, H. W. Deckman, E. Yablonovitch, T. Gmitter, W. Kobasz, and S. Garoff, J. Vac. Sci. Technol. A **3**, 887 (1985).

[66] X. D. Pi, C. P. Burrows, and P. G. Coleman, Phys. Rev. Lett. **90**, 155901 (2003).

[67] S. K. Estreicher, M. Gharaibeh, P. A. Fedders, and P. Ordejón, Phys. Rev. Lett. **86**, 1247 (2001).

[68] M. Diebel, S. Chakravarthi, S. T. Dunham, C. F. Machala, S. Ekbote, and A. Jain, in *Mater. Res. Soc. Symp. Proc.* (MRS, Warrendale, PA, 2003), vol. 765, p. D6.15.1.

[69] J. L. Hoyt, H. M. Nayfeh, S. Eguchi, I. Aberg, G. Xia, T. Drake, E. A. Fitzgerald, and D. A. Antoniadis, in *IEDM '02. Digest. International Electron Devices Meeting, 8-11 Dec. 2002,* (IEEE, Piscataway, NY, 2002), p. 23.

[70] K. Rim, J. L. Hoyt, and J. F. Gibbons, IEEE Trans. Electron Devices **47**, 1406 (2000).

[71] J. Welser, J. L. Hoyt, and J. F. Gibbons, IEEE Electron Device Letters **15**, 100 (1994).

[72] W. Windl, M. Laudon, N. N. Carlson, and M. S. Daw, IEEE Comp. Sci. Eng. **3**, 92 (2001).

[73] G. E. Dieter, *Mechanical metallurgy* (McGraw-Hill, 1988).

[74] R. Hull, *Properties of crystalline silicon* (IEEE, 1999), p. 98.

[75] P. Kuo, J. L. Hoyt, J. F. Gibbons, J. E. Turner, R. D. Jacowitz, and T. I. Kamins, Appl. Phys. Lett. **62**, 612 (1993).

[76] N. R. Zangenberg, J. Fage-Pedersen, J. Lundsgaard Hansen, and A. Nylandsted Larsen, J. Appl. Phys. **94**, 3883 (2003).

[77] W. Windl, M. M. Bunea, R. Stumpf, S. T. Dunham, and M. P. Masquelier, Phys. Rev. Lett. **83** (1999).

[78] H. Meyer and S. T. Dunham, in *Mater. Res. Soc. Symp. Proc.* (MRS, Warrendale, PA, 2002), vol. 717, p. C4.8.1.

[79] X.-Y. Liu, W. Windl, and M. P. Masquelier, Appl. Phys. Lett. **77**, 2018 (2000).

[80] T. J. Lenosky, B. Sadigh, S. K. Theiss, M. J. Caturla, and T. Diaz de la Rubia, Appl. Phys. Lett. **77**, 1834 (2000).

[81] J. Yamauchi, N. Aoki, and I. Mizushima, Phys. Rev. B **55**, R10245 (1997).

[82] T. L. Aselage, J. Mater. Res. **13**, 1786 (1998).

[83] B. Sadigh, T. J. Lenosky, M.-J. Caturla, A. A. Quong, L. X. Benedict, T. Diaz de la Rubia, M. M. Giles, M. Foad, C. D. Spataru, and S. G. Louie, Appl. Phys. Lett. **80**, 4738 (2002).

[84] N. Moriya, L. C. Feldman, H. S. Luftman, and C. A. King, J. Vac. Sci. Technol. B **12**, 383 (1994).

[85] P. Fastenko, Ph.D. thesis, University of Washington, Seattle, WA (2002).

[86] A. Baldereschi, Phys. Rev. B **7**, 5212 (1973).

[87] D. J. Chadi and M. L. Cohen, Phys. Rev. B **8**, 5747 (1973).

[88] H. J. Monkhorst and J. D. Pack, Phys. Rev. B **13**, 5188 (1976).

Appendix A

LOCAL EQUILIBRIUM OF DEFECTS/IMPURITIES IN SOLIDS

In the dilute limit ($C_{\mathrm{X}}^{*} \ll C_s$), the equilibrium concentration C_{X}^{*} of a defect/impurity X in a solid can be written as (see Ref. [30]):

$$C_{\mathrm{X}}^{*} = \theta_{\mathrm{X}} C_s \exp\left(-\frac{\tilde{G}_f^{\mathrm{X}}}{kT}\right). \tag{A.1}$$

This relationship is derived by minimizing the Gibbs free energy of the system with respect to the defect/impurity concentration C_{X}. $S = k \ln \theta_{\mathrm{X}}$ is the configurational entropy of the defect/impurity, whereas C_s is the lattice site density of the solid (in silicon $C_s = 5 \times 10^{22}\,\mathrm{cm}^{-3}$). $\tilde{G}_f^{\mathrm{X}}$ is the formation energy of the defect/impurity with respect to some well defined external reservoir. It is the energy, which is necessary to take a defect/impurity X from its reservoir and form the defect X in the solid. Assuming such an infinite reservoir, the defect/impurity concentration will interact with the reservoir until it reaches global equilibrium. The equilibrium concentration in the solid at a given temperature T is entirely determined by the configurational entropy factor θ_{X} and the formation energy $\tilde{G}_f^{\mathrm{X}}$.

In the case of point-defects, such as interstitials and vacancies, the surface of the solid serves as such a reservoir. The basic assumption is that due to the many kinks of the surface of the solid (surface roughness) the surface energy is unaltered when removing or adding an atom from the surface of the solid. This assumption breaks down under large hydrostatic pressure, since removing or adding an atom to the surface changes the volume of the solid and therefore changes the system energy. However in most practical cases the external pressure is relatively modest. In the

case of other impurities, such as dopant atoms, an outside gas phase or dopant-rich film could serve as an appropriate reservoir. However since a finite number of dopant atoms are usually introduced to the solid via ion-implantation in VLSI technology the concept of local equilibrium is very convenient in order to study clustering behavior of defects/impurities. The idea is to define an equilibrium, which is both independent of external reservoirs and the implant procedure.

In the case of compound defects/impurities, which consist of different individual defects/impurities (e.g., a boron interstitial cluster B_nI_m), the formation energy is defined by taking the individual compounds (n boron atoms and m interstitial atoms) from their external reservoirs, introducing them into the solid and then assembling them to form the compound defect/impurity B_nI_m inside of the solid. As mentioned earlier, dopant atoms are usually introduced via ion-implantation into the solid. Therefore, the first step of moving the individual building blocks from an external reservoir into the solid is done via the implantation process which is not an equilibrium process. Thus, it is desirable to change the reference energy of dopants such that to make it independent of external reservoirs and the implant process. Equation A.1 is valid in global equilibrium only. Implicitly, it is assumed that there is an infinite or at least very large reservoir of defects/impurities X, such that the reservoir does not change during the equilibration process. Only the formation energy of the defect/impurity determines the final equilibrium concentration C_X^* in the solid. In contrast, for ion-implantation, a fixed finite amount of defects/impurities C_B is introduced into the solid. Shortly after the implantation process, the system is far out of global equilibrium. Since the global equilibration process is rather slow, Eq. A.1 is no longer valid. However it is a good assumption that locally the system equilibrates very rapidly among the different defects/impurities. This means that in the neighborhood of a given spatial coordinate $\vec{x}$ in the solid, equilibrium is established among all species. This is referred to as local equilibrium. Due to the global equilibration process, local equilibrium is a function of time. Equation A.1 can be modified

to account for the new conditions. Since the individual atomic species are already present in the solid and do not need to be introduced from an outside reservoir, only an adjustment of the reference is needed. The new reference must be independent of the implant process, e.g. for a B_nI_m cluster a possible reference is the implanted B concentration C_B and not C_B^*. Introducing a factor of $(C_B/C_B^*)^n$ accounts for the change of reference. In local equilibrium:

$$\begin{aligned} C_{B_nI_m} &= \theta_{B_nI_m} C_s \left(\frac{C_B}{C_B^*}\right)^n \exp\left(-\frac{\tilde{G}_f^{B_nI_m}}{kT}\right), \\ &= \frac{\theta_{B_nI_m}}{\theta_B{}^n} C_s \left(\frac{C_B}{C_s}\right)^n \exp\left(-\frac{\tilde{G}_f^{B_nI_m} - n\,\tilde{G}_f^B}{kT}\right). \end{aligned} \tag{A.2}$$

$C_{B_nI_m}$ is expressed independently of an external infinite reservoir of B atoms and is a function of C_B. If there are only two B configurations present: B and B_nI_m, the total B concentration is $C_B^{tot} = C_B + n\,C_{B_nI_m}$. $C_B(C_B^{tot})$ and $C_{B_nI_m}(C_B^{tot})$ can be determined by solving previous equation using Eq. A.2. Figure A.1 shows a typical result for a system with three B clusters: B, B_3I, and $B_{12}I_7$.

All formation energies in this dissertation are referenced in the following way:

$$G_f^{B_nI_m} \equiv \tilde{G}_f^{B_nI_m} - n\,\tilde{G}_f^B. \tag{A.3}$$

For every atomic species the lowest energy configuration of a single atom in silicon is taken as the reference. In most cases a substitutional lattice site minimizes the energy of a single impurity atom, however there are exceptions like F (see Chapter 3). Interstitials and vacancies need to be treated in a special way, since they are not impurities. The surface of the solid provides a natural reservoir and therefore $G_f^{I,V} = \tilde{G}_f^{I,V}$. In the next section I and V are discussed in more detail.

Using this reference scheme, the concentration of a general defect A_nB_m can be written as (note the absence of the tilde):

$$C_{A_nB_m} = \frac{\theta_{A_nB_m}}{\theta_A{}^n \theta_B{}^m} C_s \left(\frac{C_A}{C_s}\right)^n \left(\frac{C_B}{C_s}\right)^m \exp\left(-\frac{G_f^{A_nB_m}}{kT}\right). \tag{A.4}$$

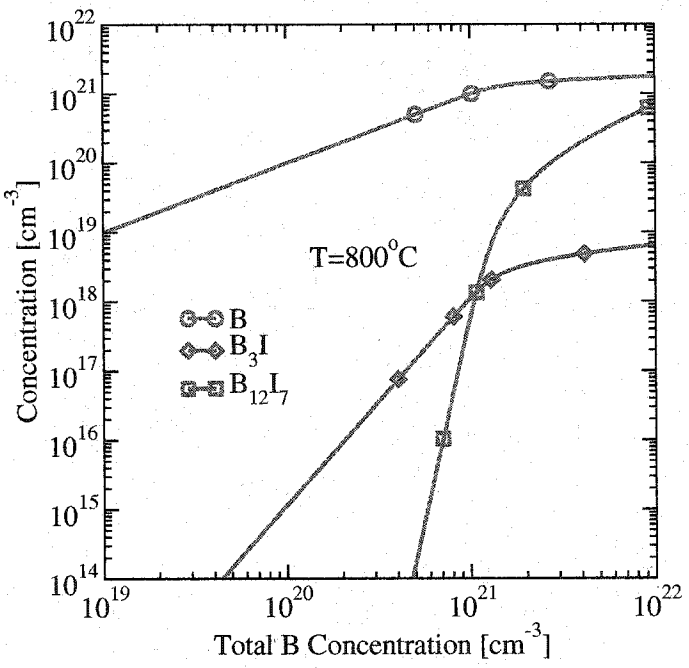

Figure A.1: Local equilibrium concentration of B, $B_{12}I$, and $B_{12}I_7$ as a function of total B concentration at $T = 800\,^{\circ}\mathrm{C}$ at $(C_\mathrm{I}/C_\mathrm{I}^*) = 1$ (see Chapter 7).

A.1 I and V supersaturation

Since point-defects (e.g., I and V) are created during the ion-implantation process, a supersaturation of these defects is present after the implantation process. Similar to the treatment of dopant atoms, the I and V references can be redefined in a similar fashion. In the following equations, the configurational entropies are dropped for simplicity, but can be added easily:

$$\begin{aligned} C_{\mathrm{B}_n\mathrm{I}_m} &= C_s \left(\frac{C_\mathrm{B}}{C_s}\right)^n \left(\frac{C_\mathrm{I}}{C_\mathrm{I}^*}\right)^m \exp\left(-\frac{G_f^{\mathrm{B}_n\mathrm{I}_m}}{kT}\right), \\ &= C_s \left(\frac{C_\mathrm{B}}{C_s}\right)^n \left(\frac{C_\mathrm{I}}{C_s}\right)^m \exp\left(-\frac{G_f^{\mathrm{B}_n\mathrm{I}_m} - m\,G_f^\mathrm{I}}{kT}\right). \end{aligned} \tag{A.5}$$

The factor $(C_\mathrm{I}/C_\mathrm{I}^*)^m$ accounts for the changed reference for interstitials. The only difference between the two equations in A.5 is the implicit or explicit inclusion of the

I formation energy. In the first case $(C_{\mathrm{I}}/C_{\mathrm{I}}^{*})^{m}$ accounts implicitly for a I supersaturation; the formation energy $G_f^{\mathrm{B}_n\mathrm{I}_m}$ is unchanged. In contrast, in the second case, G_f^{I} is explicitly included by using $G_f^{\mathrm{B}_n\mathrm{I}_m} - m\,G_f^{\mathrm{I}}$ and $(C_{\mathrm{I}}/C_{\mathrm{I}}^{*})^{m}$ is replaced by $(C_{\mathrm{I}}/C_s^{*})^{m}$. Both ways of reporting formation energies are common in the literature.

Physically including the $(C_{\mathrm{I}}/C_{\mathrm{I}}^{*})^{m}$ factor means referencing all I to a new I reservoir inside of the solid, which is no longer the surface, but some other local reservoir (e.g., {311} defects). Such extended defects will sustain an I supersaturation for a limited time, which is the source of transient enhanced diffusion (TED) of B. This analysis is directly transferable to vacancy clusters by replacing $(C_{\mathrm{I}}/C_{\mathrm{I}}^{*})$ with $(C_{\mathrm{V}}/C_{\mathrm{V}}^{*})$. All arguments work in an equivalent way.

The Gibbs free energies G_f include changes in entropy due to changes of the vibrational lattice modes. Throughout this dissertation we used zero temperature calculations which do not include these entropy changes. To indicate this in the different chapters, G_f is replaced by E_f. E_f is the free energy at zero temperature.

Appendix B

HIGH SYMMETRY SITES IN THE SILICON LATTICE

There are various high symmetry interstitial configurations in the silicon (diamond) lattice. The gray atoms in the following figures illustrate schematically the interstitial sites used in this dissertation. The marked high symmetry locations (gray atoms) can be occupied by either Si atoms, resulting in Si self-interstitials, or other impurities, forming for example interstitial bond-centered fluorine F_{bc} (see Chapter 3).

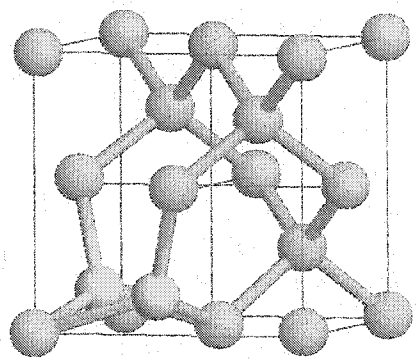

Figure B.1: The gray atoms illustrate the structure of a [110] split/dumbbell interstitialcy (I_{split}). Note that for this structure, the interstitial is not a single atom, but rather two atoms in place of a single atom.

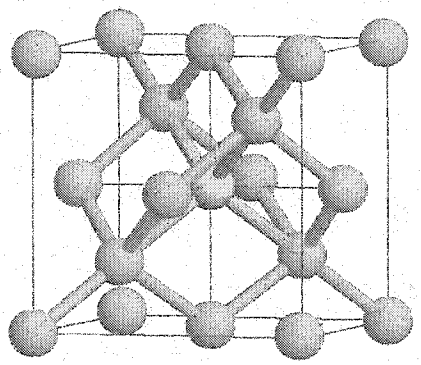

Figure B.2: The gray atom marks a tetrahedral interstitial site (I_{tet}).

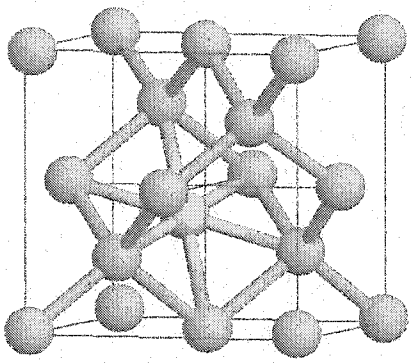

Figure B.3: The gray atom marks a hexagonal interstitial site (I_{hex}).

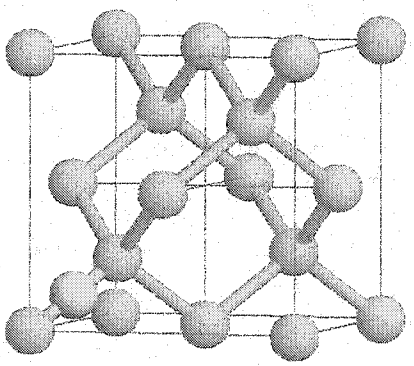

Figure B.4: The gray atom marks a bond-centered interstitial site (I_{bc}).

Appendix C

DENSITY OF STATES FOR $F_N V_M$ COMPLEXES

The density of states (DOS) of various single F and $F_n V_m$ complexes was calculated in a neutral 64 Si atom super-cell. The green (dashed) lines indicate the locations of the valence and conduction band of Si at $\pi/(4\,b)\,(1,1,1)$ in the first Brillouin zone (BZ) respectively. $b = 5.43\,\text{Å}$ is the experimental lattice constant of unstrained Si. The calculation was performed using a cutoff of 320 eV and 2^3 Monkhorst-Pack **k**-point sampling (4 irreducible **k**-points) including spin. Due to the **k**-point sampling and spin, each state in perfect Si is 8-fold degenerate. However, for some defect configurations this degeneracy gets broken, which can be seen in the associated DOS graphs. The total number of electrons N can be determined by:

$$N = \sum_i (1/4 \sum_{j=1}^{8} n_{ij}), \tag{C.1}$$

where 1/4 is the weighting factor due to the **k**-point sampling and n_{ij} is the occupation reported in the graphs (i runs over all bands). All energies are reported with respect to the valence band of Si. The total number of electrons varies depending on the defect structure.

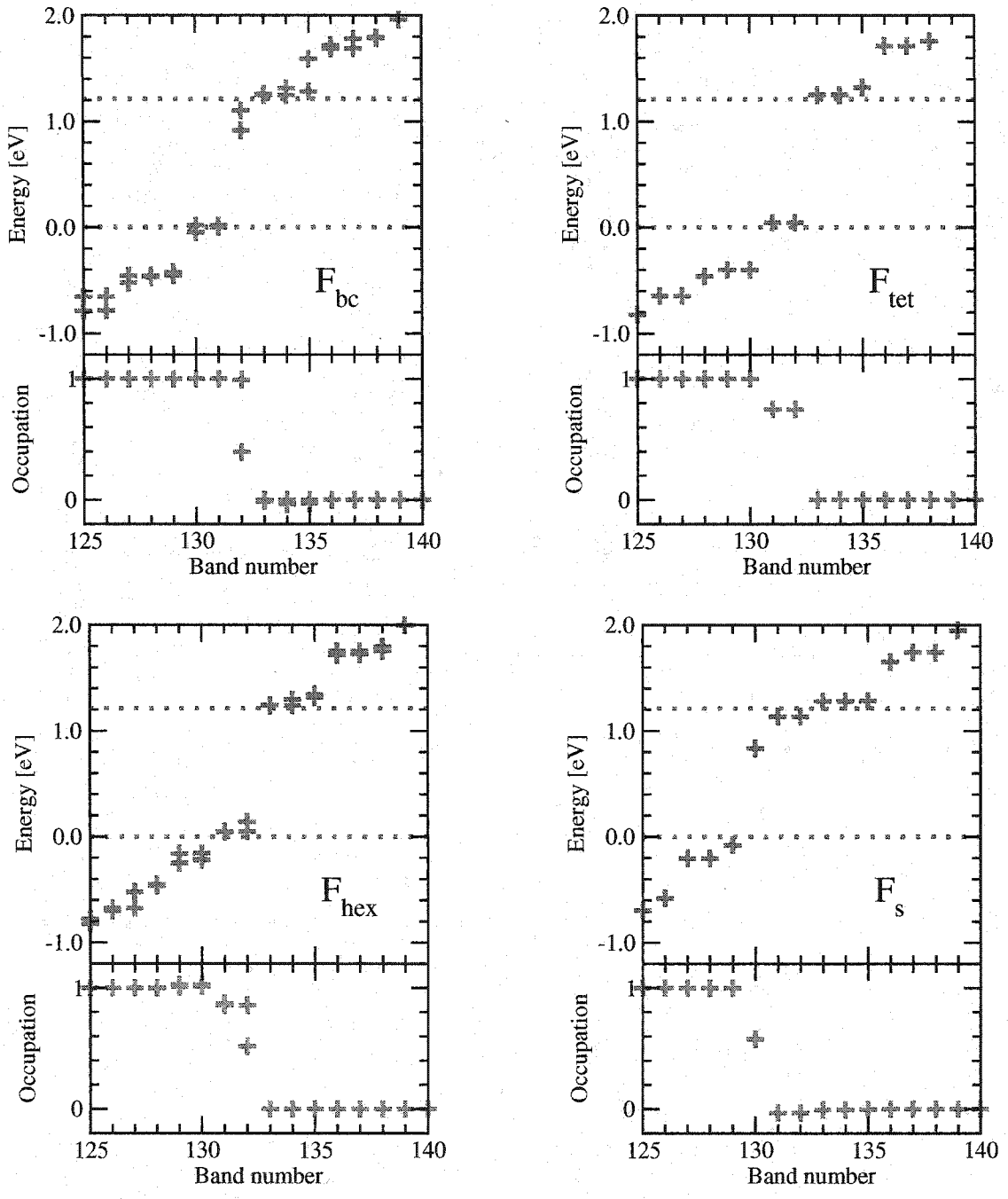

Figure C.1: DOS of interstitial F_{bc}, F_{tet}, F_{hex}, and substitutional F_s were calculated using a neutral 64 Si atom super-cell. Neutral F_{bc} and F_s have partially filled states near the conduction band minimum, so they will be positively charged for most Fermi levels. In contrast, neutral F_{tet} and F_{hex} show partially filled states near the valence band maximum, so they will be negatively charged for most Fermi levels.

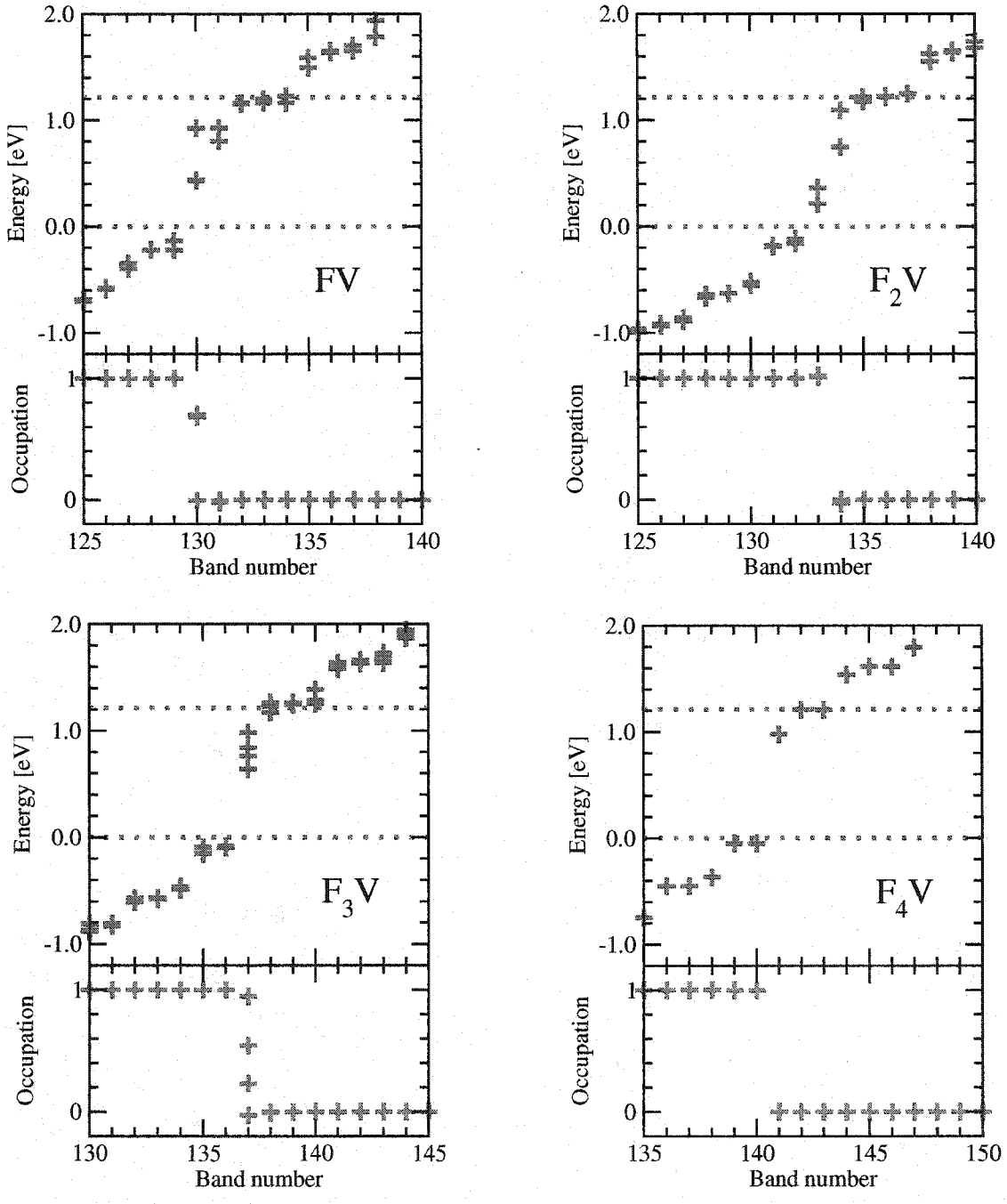

Figure C.2: DOS of FV, F_2V, F_3V, and F_4V were calculated using a neutral 64 Si atom super-cell. Neutral F_4V shows some unoccupied states near the conduction band, so it will be neutral for most Fermi levels. For a Fermi level close to midgap F_3V is neutral.

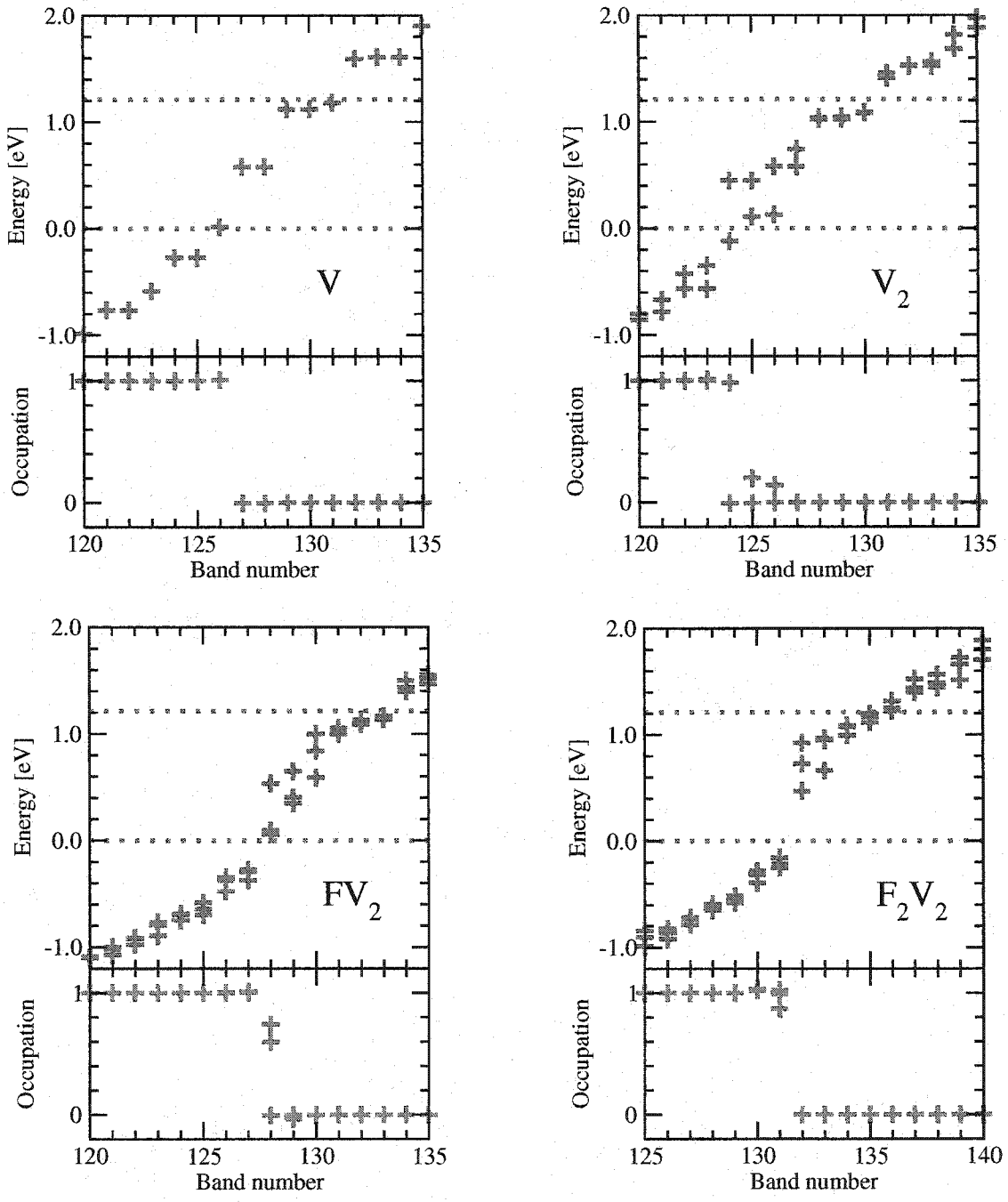

Figure C.3: DOS of V, V_2, FV_2, and F_2V_2 was calculated using a neutral 64 Si atom super-cell. Neutral V shows some unoccupied states near midgap, so for a Fermi level below these gap states V is neutral.

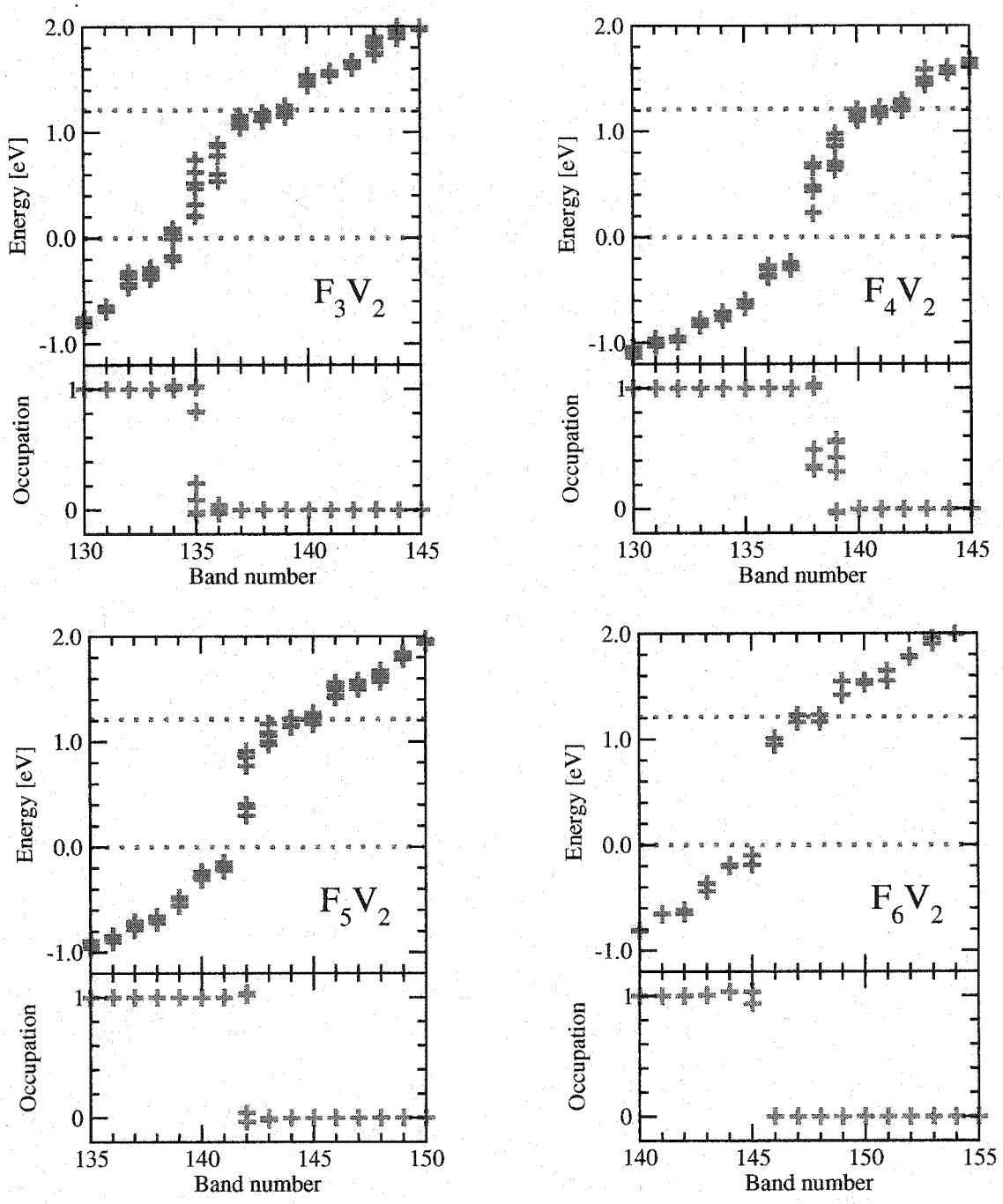

Figure C.4: DOS of F_3V_2, F_4V_2, F_5V_2, and F_6V_2 was calculated using a neutral 64 Si atom super-cell. Neutral F_6V_2 shows some unoccupied states near the conduction band, so it will be neutral for most Fermi levels.

Appendix D

DENSITY OF STATES ANALYSIS TO PREDICT CHARGE EFFECTS

The density of states (DOS) of charge neutral super-cell calculations can be used to predict the total energy of the corresponding charged super-cells. This enables the determination of the Fermi level dependence of formation energies for charged defects. The idea is (assuming that the DOS and total energy E_{X^0} of a defect X^0 is known) to empty/fill the highest/lowest occupied/unoccupied electronic states to predict the total energy of the resulting charged super-cell. The details of the method will be explained by considering two F defects with opposite charge: F_{bc}^{+} and F_{tet}^{-}.

Figure D.1 shows the DOS of an uncharged (left) vs. a positively charged super-cell (right) calculation of interstitial bond-centered F (F_{bc}). In the case of the neutral super-cell (left), there are partially filled states near the conduction band edge (band number 132). This means that for Fermi levels below these states F_{bc} is positively charged, since the system can lower its energy by emptying these states and donating the electron to the Fermi sea.

The total energy of a charged super-cell can be determined by simply minimizing the energy of a super-cell with added/subtracted electrons via an additional DFT calculation. The result for the DOS of such a calculation is shown for F_{bc}^{+} in Fig. D.1 (right). We claim that we can predict the resulting total energy of such F complexes by just subtracting the energy of the partially occupied states. The correction term is determined by simple integration of the DOS for $E > E_F^{\mathrm{X}^+}$:

$$E_{\mathrm{X}^+}(E_F = E_F^{\mathrm{X}^+}) = E_{\mathrm{X}^0} - \Delta E = E_{\mathrm{X}^0} - \int_{E_F^{\mathrm{X}^+}}^{\infty} n(E)g(E)EdE, \qquad \text{(D.1)}$$

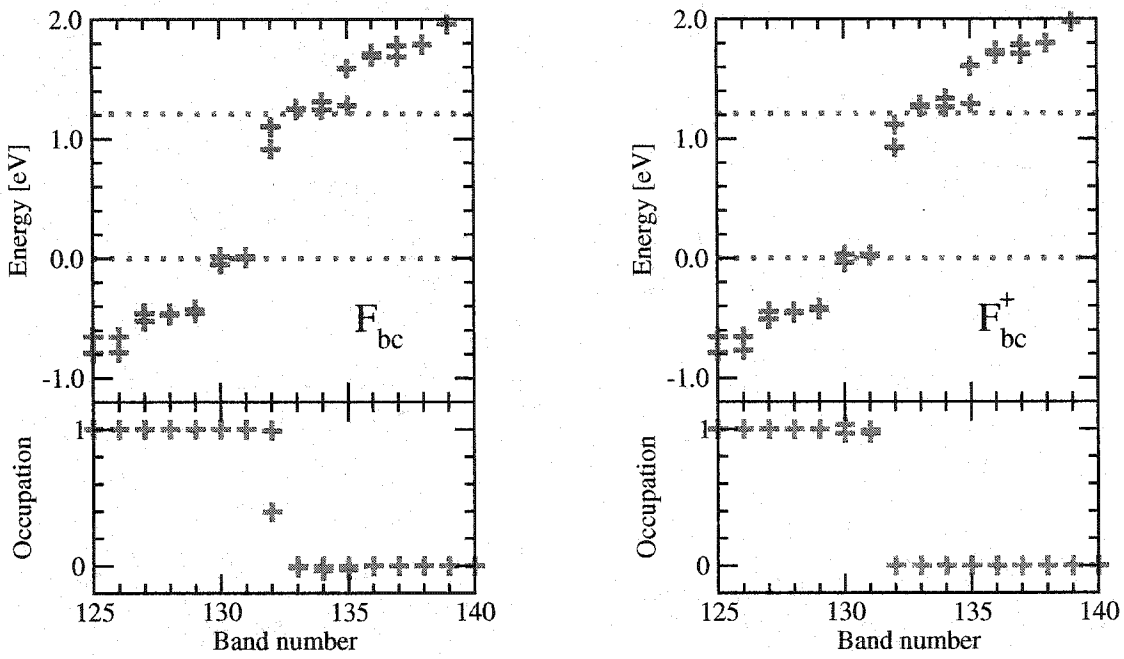

Figure D.1: DOS of interstitial F_{bc} and 64 Si atoms of a neutral (left) and positively charged (right) super-cell calculation (263 electrons/262 electrons). The green (dashed) lines indicate the locations of the valence and conduction band of Si at $\pi/(4\,b)\,(1,1,1)$ in the first Brillouin zone (BZ) respectively. $b = 5.43\,\text{Å}$ is the experimental lattice constant of unstrained Si. Since the calculation was performed using a cutoff of 320 eV and 2^3 Monkhorst-Pack **k**-point sampling (4 irreducible **k**-points) including spin, every state is 8-fold degenerate. The total number of electrons N is determined by $N = \sum_i (1/4 \sum_{j=1}^{8} n_{ij})$. 1/4 is the weighting factor due to the **k**-point sampling and n_{ij} is the occupation. i runs over all bands. All energies are reported with respect to the valence band of Si.

where $n(E)$ is the electron occupation and $g(E)$ is the DOS of electrons. $E_F^{X^+}$ is determined from $\int_{E_F^{X^+}}^{\infty} n(E)g(E)dE = 1$. Note that there is a range of energy values that satisfy this requirement, but they all give the same correction. E_{X^+} and E_{X^0} are the total energies of the charged and uncharged super-cell respectively. Figure D.1 (right) shows, that indeed the only significant difference between the uncharged and charged DOS are the reduced occupations in band 132. In the case of F_{bc} the prediction is accurate up to -0.00344 eV, which is smaller than the overall convergence error of

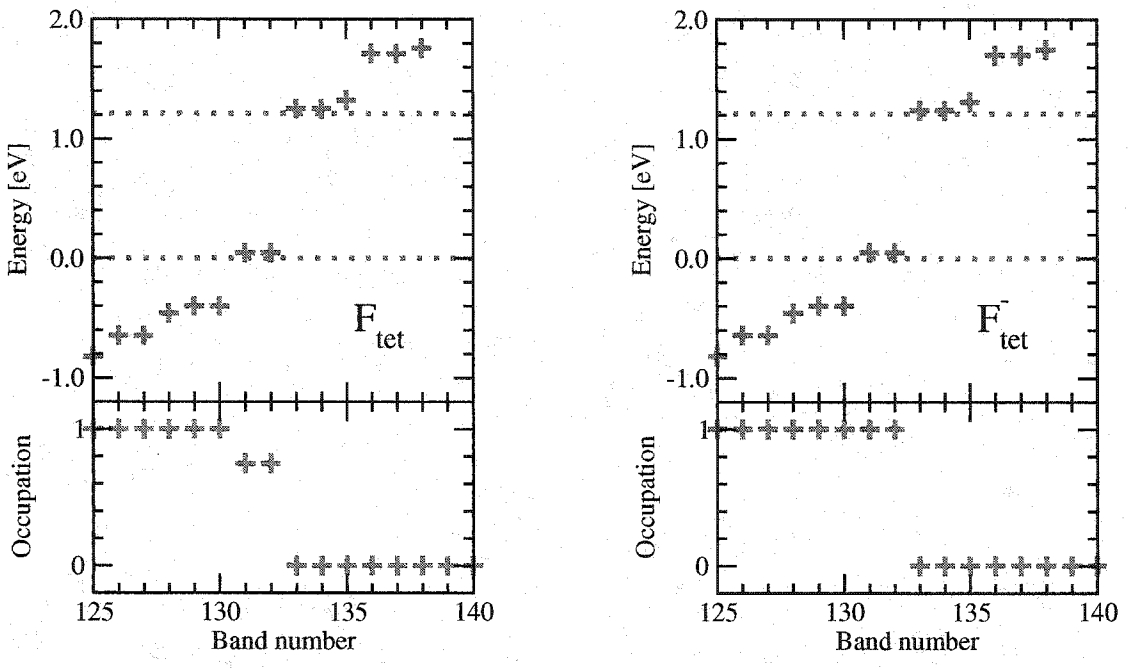

Figure D.2: DOS of interstitial F_{tet} and 64 Si atoms of a neutral (left) and negatively charged (right) super-cell calculation (263 electrons/264 electrons). The green (dashed) lines indicate the locations of the valence and conduction band of Si at $\pi/(4\,b)\,(1,1,1)$ in the first Brillouin zone (BZ) respectively. $b = 5.43\,\text{Å}$ is the experimental lattice constant of unstrained Si. Since the calculation was performed using a cutoff of 320 eV and 2^3 Monkhorst-Pack **k**-point sampling (4 irreducible **k**-points), including spin every state is 8-fold degenerate. The total number of electrons N is determined by $N = \sum_i (1/4 \sum_{j=1}^{8} n_{ij})$. 1/4 is the weighting factor due to the **k**-point sampling and n_{ij} is the occupation. i runs over all bands. All energies are reported with respect to the valence band of Si.

the calculations of about 0.1 eV.

Theoretically, this approach has to work well as long as the new charge density does not strongly alter the effective one-electron interaction potential. This assumption could be violated if the added/subtracted electron leads to significant ionic relaxations.

In a similar way, the total energy of negatively charged super-cells can be predicted. Figure D.2 shows the DOS of an uncharged (left) vs. a negatively charged super-cell (right) calculation of interstitial tetrahedral F (F_{tet}). In the case of the neutral super-

cell (left), there are partially filled states close to the Si valence band edge (bands number 131 and 132). These are hole states. This indicates that the neutral super-cell calculation actually corresponds to $F_{tet}^{-} + h^{+}$. Indeed, the charge density of F_{tet} shows such a localized negative charge around F_{tet}. Figure D.2 (right) shows the DOS for a negatively charged super-cell. The only significant difference between the two DOS is the occupation of the former partially filled states in bands number 131 and 132. The total energy of the resulting charged super-cell can be calculated similar to Eq. D.1 by just integrating the hole DOS for $E < E_F^{X^-}$:

$$E_{X^-}(E_F = E_F^{X^-}) = E_{X^0} + \Delta E = E_{X^0} + \int_{-\infty}^{E_F^{X^-}} (1 - n(E))g(E)EdE, \qquad (D.2)$$

where $(1 - n(E))$ is hole occupation, whereas E_{X^-} and E_{X^0} are the total energies of the charged and uncharged super-cells respectively. $E_F^{X^-}$ is chosen to give a change of one electron in system and for F_{tet} can be anywhere in the band gap.

The above described method was compared to actual charged super-cell calculations for the following F and Si configurations: F_{bc}, F_{tet}, F_{hex}, F_{sub}, FV, F_3V, and I_{split}. The results are summarized in Table D.1. ΔE is the actual energy difference between the charged and uncharged super-cells, whereas ΔE_{pred} is the predicted difference based on Eqs. D.1 and D.2. In all cases, the predictions are in excellent agreement with the calculated results.

Analyzing the DOS of uncharged supercell calculations provides tool for investigating possible charged states. However, since in general the exact location of the physical gap states can not be determined by DFT in a trustable way, one need to be cautious. There are also possible corrections to the gap states locations due to relaxation effects. Such a behavior is only expected for significant changes to the charge density. However, termination of dangling bonds, as in the case of fluorine/vacancy complexes (see Chapter 3), simplifies the charge density and therefore should be a less sensitive case.

To determine the Fermi level dependence of the formation energies of charged

Table D.1: Comparison of the difference in energy between uncharged and charged super-cell calculations ΔE for various defect configuration with the predicted difference ΔE_{pred} based on the discussed DOS analysis.

	ΔE [eV]	ΔE_{pred} [eV]	$\Delta E - \Delta E_{pred}$ [eV]
F_{bc} / F_{bc}^{+}	5.6637	5.6672	−0.0034
F_{tet} / F_{tet}^{-}	−4.7910	−4.7221	−0.0689
F_{hex} / F_{hex}^{-}	−4.8460	−4.8037	−0.0423
F_{sub} / F_{sub}^{+}	5.3977	5.4569	−0.0592
FV / FV^{+}	5.0657	5.0944	−0.0288
F_3V / F_3V^{+}	5.3610	5.3574	0.0036
I_{split} / I_{split}^{+}	5.0580	5.0353	0.0227

defects (see Fig. 3.2) using the above correction scheme, the location of the valence band edge (location of Γ point in the case of Si) needs to be known to provide a well defined reference. In our DFT calculations, we used finite sampling of the first Brillouin zone (BZ). Depending on the **k**-point sampling the Γ point is not always included. Thus, we need to correct for this effect when reporting formation energies. Figure D.3 illustrates the need for such a correction. Shown is the standard Si band structure determined based on a two atom Si primitive cell using a GGA calculation. The energy difference between Γ and L of the top valence band is 1.19 eV, which agrees very well with various other theoretical, (1.05-1.28) eV, and experimental, (1.2± 0.2) eV, results [4]. DFT predicts the valence band structure of silicon very reliable, however due to well know underestimation of the band gap, predicting the energies of conduction band states is problematic.

For 2^3 Monkhorst-Pack **k**-point sampling, the **k**-points used for different super-cells are indicated. The 3D shapes of the 1st BZ for the different super-cells are shown in Fig. D.4. In case of a 64 Si atom super-cell and 2^3 Monkhorst-Pack **k**-point sampling,

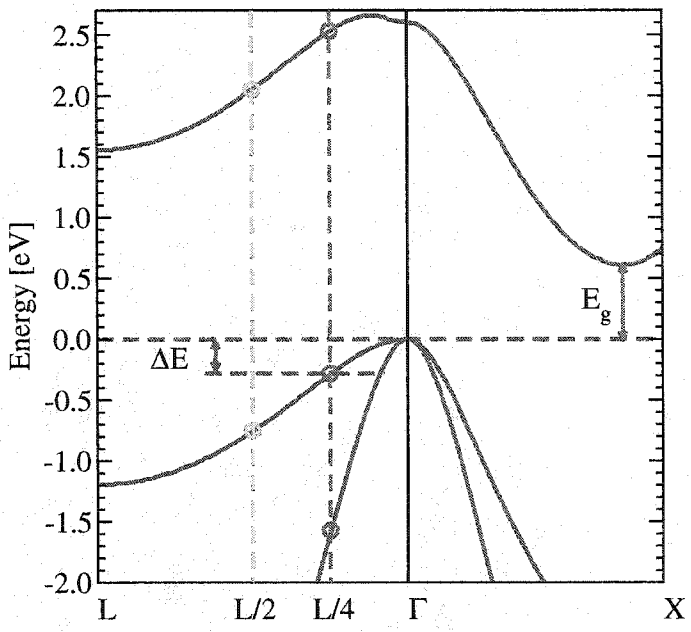

Figure D.3: DFT calculation of the silicon band structure near the valence band maximum and conduction band minimum for a two atom cell. $L = \pi/b\,(1,1,1)$, $\Gamma = 2\pi/b\,(0,0,0)$, and $X = 2\pi/b\,(1,0,0)$ with $b = 5.43\,\text{Å}$ are the high symmetry points of the first Brillouin zone (BZ). The green (dashed) line indicates the valence band edge, whereas the blue arrow marks the silicon band gap. The orange dashed line indicates the **k**-points used in a 2^3 Monkhorst-Pack **k**-point sampling calculation with a cubic super-cell of size b, whereas the blue dashed line indicates a super-cell of size $2b$. The 3D shapes of the different 1st BZ are shown in Fig. D.4.

the correction term is the energy difference between the valence band energy at the Γ point and $L/4$ of a 2 Si atom super-cell. Figure D.3 predicts $\Delta E = 0.285\,\text{eV}$ based on a 2 Si atom super-cell. This energy difference can be also determined using a 64 Si atom super-cell. The result is $\Delta E = 0.2845\,\text{eV}$ which is consistent with the former value.

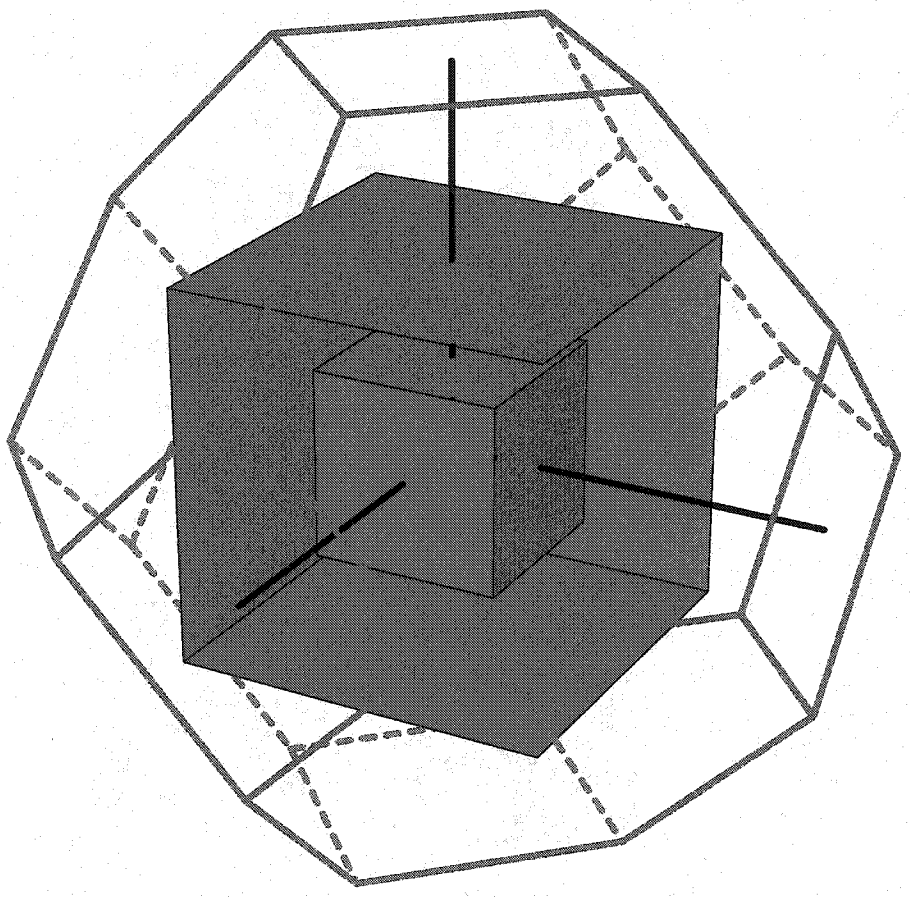

Figure D.4: First Brillouin zone (BZ) of silicon for different super-cell sizes. The wire frame shows the BZ of two silicon atom cell, the open box is BZ for 8 silicon atom cell, and the closed box is for 64 silicon atom cell. The <100> directions are indicated by the black coordinate axes. The figure shows that the location of the L point for a two and 8 silicon atom super-cell is identical, whereas the L point in the case of a 64 silicon atom super-cell is located at $L/2$ of the two/8 silicon atom super-cell. Figure 3.3 shows the corresponding Si band structure along the Λ-direction (Γ to L) and Δ-direction (Γ to X).

Appendix E

GENERAL STRESS/STRAIN RELATIONS

In the linear elastic limit, the strain dependence of the formation energy of a defect/impurity in a solid can be derived from Hooke's law. The relationship is given by:

$$E(\vec{\epsilon}) = E_0 + \frac{\Omega}{2}\left(\vec{\epsilon} - \Delta\vec{\epsilon}\right)\mathbf{C}\left(\vec{\epsilon} - \Delta\vec{\epsilon}\right), \tag{E.1}$$

where

$$\mathbf{C} = \begin{pmatrix} C_{11} & C_{12} & C_{13} \\ C_{12} & C_{22} & C_{23} \\ C_{13} & C_{23} & C_{33} \end{pmatrix} \quad \text{and} \quad \Delta\vec{\epsilon} = \begin{pmatrix} \Delta\epsilon_1 \\ \Delta\epsilon_3 \\ \Delta\epsilon_3 \end{pmatrix}. \tag{E.2}$$

$\mathbf{C}$ is the elasticity tensor of the material, $\Delta\vec{\epsilon}$ is the induced strain relative to a reference lattice spacing, and Ω is the volume of the system. In our notation $\vec{\epsilon}$ is defined relative to the equilibrium lattice vector of silicon, that is $\vec{\epsilon} = \vec{b}/b_{\mathrm{Si}} - 1$. If only normal strains/stresses are considered, there are nine unknowns; six elastic constants C_{11}, C_{22}, C_{33}, C_{12}, C_{13}, and C_{23} and three induced strains $\Delta\epsilon_1$, $\Delta\epsilon_2$, and $\Delta\epsilon_3$. The spatial symmetries of a defect/cluster often reduce the number of unknowns. By straining the material in different directions all unknowns can be determined, since they are related by Eq. E.1. The most consistent method is to fit a large set of energy vs. strain data (strain applied in different directions) to an equation-of-state such as Eq. E.1. In the linear elastic limit, energy-strain curves have a parabolic shape. To analyze the behavior of different defects/impurities under stress/strain it is instructional to know the value of the strain which minimizes the energy of the system and curvature of the energy-strain curve for different simple strain cases as a function of the elastic constants and induced strains. In the following sections, the

results of several strain cases are listed. As mentioned earlier, spatial symmetries of a defect/impurity often further simplify the relations. For example, the location of the minimum for a completely symmetric structure ($x \leftrightarrow y \leftrightarrow z$) under hydrostatic strain reduces to $\epsilon_{min} = \Delta\epsilon_1 = \Delta\epsilon_2 = \Delta\epsilon_3$.

E.1 Hydrostatic strain

The following strain vector $\vec{\epsilon}$ minimizes Eq. E.1 for $\epsilon = \epsilon_{min}$. The curvature of $E(\vec{\epsilon})$ for this strain vector is given by $\partial^2 E/\partial\epsilon^2$:

$$\vec{\epsilon} = (\epsilon, \epsilon, \epsilon)\,, \tag{E.3}$$

$$\epsilon_{min} = \frac{(C_{11}+C_{12}+C_{13})\Delta\epsilon_1 + (C_{22}+C_{12}+C_{23})\Delta\epsilon_2 + (C_{33}+C_{13}+C_{23})\Delta\epsilon_3}{C_{11}+C_{22}+C_{33}+2C_{12}+2C_{13}+2C_{23}}, \tag{E.4}$$

$$\frac{\partial^2 E}{\partial\epsilon^2} = \Omega\,(C_{11}+C_{22}+C_{33}+2C_{12}+2C_{13}+2C_{23}). \tag{E.5}$$

For a completely symmetric defect/impurity ($x \leftrightarrow y \leftrightarrow z$) $C_{11} = C_{22} = C_{33}$, $C_{12} = C_{13} = C_{23}$ and $\Delta\epsilon_1 = \Delta\epsilon_2 = \Delta\epsilon_3$, so above equations can be simplified to:

$$\epsilon_{min} = \Delta\epsilon_1, \tag{E.6}$$

$$\frac{\partial^2 E}{\partial\epsilon^2} = 3\,\Omega\,(C_{11}+2C_{12}). \tag{E.7}$$

In the hydrostatic case, the curvature $\partial^2 E/\partial\epsilon^2$ is related directly to the bulk modulus K. The basic definition of K is:

$$K = \Omega_0 \left.\frac{\partial^2 E(\Omega)}{\partial\Omega^2}\right|_{\Omega=\Omega_0}, \tag{E.8}$$

where Ω_0 is the volume of the unstrained system. Combining Eq. E.5 and E.8 results in:

$$\begin{aligned} K \;=\; & \frac{1}{9}\Big(C_{11}+C_{22}+C_{33}+2C_{12}+2C_{13}+2C_{23} \\ & + 2\Delta\epsilon_1(C_{11}+C_{12}+C_{13}) + 2\Delta\epsilon_2(C_{12}+C_{22}+C_{23}) \\ & + 2\Delta\epsilon_3(C_{13}+C_{23}+C_{33})\Big). \end{aligned} \tag{E.9}$$

In the fully symmetric case without any induced strains (e.g. pure silicon), this relation reduces to:

$$K = \frac{1}{3}\left(C_{11} + 2C_{12}\right). \tag{E.10}$$

E.2 Uniaxial strain

The following strain vector $\vec{\epsilon}$ (x-direction) minimizes Eq. E.1 for $\epsilon = \epsilon_{min}$. The curvature of $E(\vec{\epsilon})$ for this strain vector is given by $\partial^2 E/\partial\epsilon^2$:

$$\vec{\epsilon} = (\epsilon, 0, 0), \tag{E.11}$$

$$\epsilon_{min} = \frac{C_{11}\Delta\epsilon_1 + C_{12}\Delta\epsilon_2 + C_{13}\Delta\epsilon_3}{C_{11}}, \tag{E.12}$$

$$\frac{\partial^2 E}{\partial\epsilon^2} = \Omega\, C_{11}. \tag{E.13}$$

For a completely symmetric defect/impurity ($x \leftrightarrow y \leftrightarrow z$), above equations can be simplified to:

$$\epsilon_{min} = \Delta\epsilon_1\left(\frac{C_{11} + 2C_{12}}{C_{11}}\right) = \Delta\epsilon_1\left(1 + \frac{2C_{12}}{C_{11}}\right), \tag{E.14}$$

$$\frac{\partial^2 E}{\partial\epsilon^2} = \Omega\, C_{11}. \tag{E.15}$$

Similarly, for uniaxial strain in the y-direction:

$$\vec{\epsilon} = (0, \epsilon, 0), \tag{E.16}$$

$$\epsilon_{min} = \frac{C_{12}\Delta\epsilon_1 + C_{22}\Delta\epsilon_2 + C_{23}\Delta\epsilon_3}{C_{22}}, \tag{E.17}$$

$$\frac{\partial^2 E}{\partial\epsilon^2} = \Omega\, C_{22}, \tag{E.18}$$

and in the z-direction:

$$\vec{\epsilon} = (0, 0, \epsilon), \tag{E.19}$$

$$\epsilon_{min} = \frac{C_{13}\Delta\epsilon_1 + C_{23}\Delta\epsilon_2 + C_{33}\Delta\epsilon_3}{C_{33}}, \tag{E.20}$$

$$\frac{\partial^2 E}{\partial\epsilon^2} = \Omega\, C_{33}. \tag{E.21}$$

E.3 Biaxial strain

For biaxial strain in xy-plane, the following strain vector minimizes Eq. E.1 for $\epsilon = \epsilon_{min}$. The curvature of $E(\vec{\epsilon})$ for this strain vector is given by $\partial^2 E/\partial\epsilon^2$:

$$\vec{\epsilon} = (\epsilon, \epsilon, 0)\,, \tag{E.22}$$

$$\epsilon_{min} = \frac{(C_{11}+C_{12})\Delta\epsilon_1 + (C_{22}+C_{12})\Delta\epsilon_2 + (C_{13}+C_{23})\Delta\epsilon_3}{C_{11}+C_{22}+2C_{12}}, \tag{E.23}$$

$$\frac{\partial^2 E}{\partial\epsilon^2} = \Omega\,(C_{11}+C_{22}+2C_{12}). \tag{E.24}$$

For a completely symmetric defect/impurity ($x \leftrightarrow y \leftrightarrow z$), above equations can be simplified to:

$$\epsilon_{min} = \Delta\epsilon_1 \left(\frac{C_{11}+2C_{12}}{C_{11}+C_{12}}\right), \tag{E.25}$$

$$\frac{\partial^2 E}{\partial\epsilon^2} = 2\,\Omega\,(C_{11}+C_{12}). \tag{E.26}$$

Similarly for biaxial xz-strain:

$$\vec{\epsilon} = (\epsilon, 0, \epsilon)\,, \tag{E.27}$$

$$\epsilon_{min} = \frac{(C_{11}+C_{13})\Delta\epsilon_1 + (C_{12}+C_{23})\Delta\epsilon_2 + (C_{33}+C_{13})\Delta\epsilon_3}{C_{11}+C_{33}+2C_{13}}, \tag{E.28}$$

$$\frac{\partial^2 E}{\partial\epsilon^2} = \Omega\,(C_{11}+C_{33}+2C_{13}), \tag{E.29}$$

and for biaxial yz-strain:

$$\vec{\epsilon} = (0, \epsilon, \epsilon)\,, \tag{E.30}$$

$$\epsilon_{min} = \frac{(C_{12}+C_{13})\Delta\epsilon_1 + (C_{22}+C_{23})\Delta\epsilon_2 + (C_{33}+C_{23})\Delta\epsilon_3}{C_{22}+C_{33}+2C_{23}}, \tag{E.31}$$

$$\frac{\partial^2 E}{\partial\epsilon^2} = \Omega\,(C_{22}+C_{33}+2C_{23}). \tag{E.32}$$

E.4 Poisson's ratio

The relationships in the previous sections are true for very specific strain conditions. They are very useful for purely theoretical analysis, but not really suitable for experimental conditions. It is usually much easier to apply a well controlled stress to a

solid in an experiment instead of a strain. Therefore the boundary conditions for real experiments are often stress and not strain conditions or else some combination of the two. Figure E.1 shows a solid under tensile uniaxial stress. Once the stress is applied in one direction the solid will modify its shape in order to minimize its energy. This is equivalent of saying that the solid will deform such that all surfaces perpendicular to the applied stress direction are stress free. The boundary condition for uniaxial stress is therefore:

$$\vec{\sigma} = \begin{pmatrix} \sigma \\ 0 \\ 0 \end{pmatrix}. \tag{E.33}$$

Due to symmetry the resulting strain vector has to have the following form $\vec{\epsilon} = (\epsilon, \tilde{\epsilon}, \tilde{\epsilon})$. In the linear elastic regime, $\tilde{\epsilon}$ is related by Poisson's ratio to ϵ:

$$\tilde{\epsilon} = -\nu\epsilon, \tag{E.34}$$

where Poisson's ratio ν accounts for the compression in the perpendicular directions. By using Hooke's law, $\vec{\sigma} = \mathbf{C}\vec{\epsilon}$, and Eq. E.33, ν can be expressed in terms of the elasticity constants C_{ij}. For an isotropic material this results in:

$$\nu = \frac{C_{12}}{C_{11} + C_{12}}. \tag{E.35}$$

Similarly for biaxial stress the boundary condition is:

$$\vec{\sigma} = \begin{pmatrix} \sigma \\ \sigma \\ 0 \end{pmatrix}, \tag{E.36}$$

since a fixed stress σ is applied in two directions. Accordingly the solid will modify its shape to make the surfaces in the third direction stress free. The applied strain vector is respectively $\vec{\epsilon} = (\epsilon, \epsilon, -\tilde{\nu}\epsilon)$. Using Hooke's law and the stress constraint of Eq. E.36 results in:

$$\tilde{\nu} = \frac{2C_{12}}{C_{11}}. \tag{E.37}$$

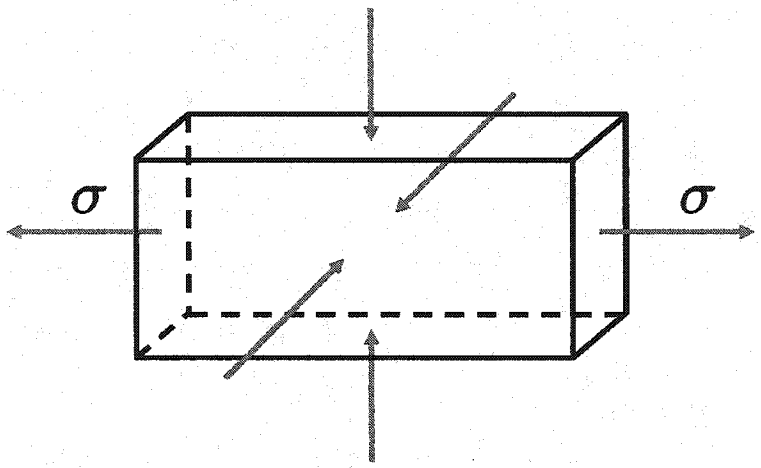

Figure E.1: Application of a tensile uniaxial stress $\vec{\sigma}$ leads to a compressive strain in the perpendicular directions until the surfaces in the perpendicular directions are stress free.

This is the equivalent of Poisson's ratio for biaxial stress. A more thorough discussion of stresses and strains can be found in Ref. [73].

Appendix F

TWO-STEP TRANSITION VECTORS

F.1 Transition vectors of analytic two-step model

Figure F.1 shows schematically the two-step process used to calculate analytically I and B diffusivity in Chapter 6. Each arrow in the graph corresponds to a transition vector $\vec{t}_i$ (first transition) and $\vec{t}_j$ (second transition). The following Tables F.1-F.8 lists the transition vectors and displacement vectors $\Delta\vec{x}_{ij}$ used to determine the analytic expressions in Eq. 6.11. Since the Si diamond lattice consists of two fcc sub-lattices, the transition vectors and displacement vectors for initial lattice sites located on the two different sub-lattices are reported. Tables F.1-F.4 lists the transition vectors and displacement vectors for the initial point $(0, 0, 0)$, whereas Tables F.5-F.8 show the results for $(1/4, 1/4, 1/4)$. All coordinates are reported in units of the Si lattice parameter $b = 5.43$ Å.

It turns out that the analytic expressions in Eq. 6.11 are independent of the choice of the initial lattice site. Both sets of transition and displacement vectors are just reported for completeness.

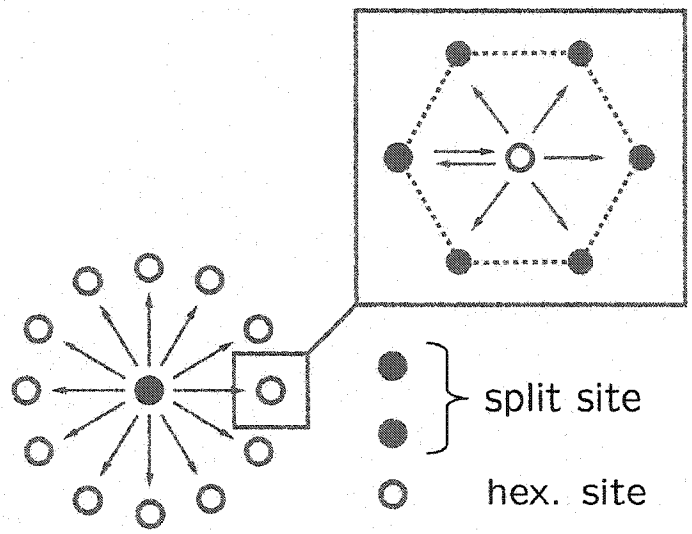

Figure F.1: Schematic illustration of the two-step process for I and B migration. In the case of an interstitial, originating from the I split site shown in red, there are 72 possible two-step transitions ($I_{split} \rightarrow I_{hex} \rightarrow I_{split}$), 12 different initial $I_{split} \rightarrow I_{hex}$ transitions followed by 6 possible $I_{hex} \rightarrow I_{split}$ transitions for each initial transition.

Table F.1: Transitions 1-18 out of 72 two-step transitions originating from $(0,0,0)$. b is the Si lattice parameter.

$\vec{t}_i$ $[b/8]$	I_{hex} $[b/8]$	$\vec{t}_j$ $[b/8]$	I_{split} $[b]$	$\Delta\vec{x}_{ij}$ $[b]$
(3 ,1,−1)	(3 ,1,−1)	(−1, 1 , 3)	(1/4 , 1/4 , 1/4)	(1/4 , 1/4 , 1/4)
(3 ,1,−1)	(3 ,1,−1)	(1 , 3 , 1)	(1/2 , 1/2 , 0)	(1/2 , 1/2 , 0)
(3 ,1,−1)	(3 ,1,−1)	(3 , 1 ,−1)	(3/4 , 1/4 ,−1/4)	(3/4 , 1/4 ,−1/4)
(3 ,1,−1)	(3 ,1,−1)	(1 ,−1,−3)	(1/2 , 0 ,−1/2)	(1/2 , 0 ,−1/2)
(3 ,1,−1)	(3 ,1,−1)	(−1,−3,−1)	(1/4 ,−1/4,−1/4)	(1/4 ,−1/4,−1/4)
(3 ,1,−1)	(3 ,1,−1)	(−3,−1, 1)	(0 , 0 , 0)	(0 , 0 , 0)
(1 ,3,−1)	(1 ,3,−1)	(1 ,−1, 3)	(1/4 , 1/4 , 1/4)	(1/4 , 1/4 , 1/4)
(1 ,3,−1)	(1 ,3,−1)	(3 , 1 , 1)	(1/2 , 1/2 , 0)	(1/2 , 1/2 , 0)
(1 ,3,−1)	(1 ,3,−1)	(1 , 3 ,−1)	(1/4 , 3/4 ,−1/4)	(1/4 , 3/4 ,−1/4)
(1 ,3,−1)	(1 ,3,−1)	(−1, 1 ,−3)	(0 , 1/2 ,−1/2)	(0 , 1/2 ,−1/2)
(1 ,3,−1)	(1 ,3,−1)	(−3,−1,−1)	(−1/4, 1/4 ,−1/4)	(−1/4, 1/4 ,−1/4)
(1 ,3,−1)	(1 ,3,−1)	(−1,−3, 1)	(0 , 0 , 0)	(0 , 0 , 0)
(−1,1, 3)	(−1,1, 3)	(3 , 1 ,−1)	(1/4 , 1/4 , 1/4)	(1/4 , 1/4 , 1/4)
(−1,1, 3)	(−1,1, 3)	(1 , 3 , 1)	(0 , 1/2 , 1/2)	(0 , 1/2 , 1/2)
(−1,1, 3)	(−1,1, 3)	(−1, 1 , 3)	(−1/4, 1/4 , 3/4)	(−1/4, 1/4 , 3/4)
(−1,1, 3)	(−1,1, 3)	(−3,−1, 1)	(−1/2, 0 , 1/2)	(−1/2, 0 , 1/2)
(−1,1, 3)	(−1,1, 3)	(−1,−3,−1)	(−1/4,−1/4, 1/4)	(−1/4,−1/4, 1/4)
(−1,1, 3)	(−1,1, 3)	(1 ,−1,−3)	(0 , 0 , 0)	(0 , 0 , 0)

Table F.2: Transitions 19-36 out of 72 two-step transitions originating from $(0,0,0)$. b is the Si lattice parameter.

$\vec{t}_i$ $[b/8]$	I_{hex} $[b/8]$	$\vec{t}_j$ $[b/8]$	I_{split} $[b]$	$\Delta\vec{x}_{ij}$ $[b]$
(−1, 3 ,1)	(−1, 3 ,1)	(3 ,−1, 1)	(1/4 , 1/4 , 1/4)	(1/4 , 1/4 , 1/4)
(−1, 3 ,1)	(−1, 3 ,1)	(1 , 1 , 3)	(0 , 1/2 , 1/2)	(0 , 1/2 , 1/2)
(−1, 3 ,1)	(−1, 3 ,1)	(−1, 3 , 1)	(−1/4, 3/4 , 1/4)	(−1/4, 3/4 , 1/4)
(−1, 3 ,1)	(−1, 3 ,1)	(−3, 1 ,−1)	(−1/2, 1/2 , 0)	(−1/2, 1/2 , 0)
(−1, 3 ,1)	(−1, 3 ,1)	(−1,−1,−3)	(−1/4, 1/4 ,−1/4)	(−1/4, 1/4 ,−1/4)
(−1, 3 ,1)	(−1, 3 ,1)	(1 ,−3,−1)	(0 , 0 , 0)	(0 , 0 , 0)
(1 ,−1,3)	(1 ,−1,3)	(1 , 3 ,−1)	(1/4 , 1/4 , 1/4)	(1/4 , 1/4 , 1/4)
(1 ,−1,3)	(1 ,−1,3)	(3 , 1 , 1)	(1/2 , 0 , 1/2)	(1/2 , 0 , 1/2)
(1 ,−1,3)	(1 ,−1,3)	(1 ,−1, 3)	(1/4 ,−1/4, 3/4)	(1/4 ,−1/4, 3/4)
(1 ,−1,3)	(1 ,−1,3)	(−1,−3, 1)	(0 ,−1/2, 1/2)	(0 ,−1/2, 1/2)
(1 ,−1,3)	(1 ,−1,3)	(−3,−1,−1)	(−1/4,−1/4, 1/4)	(−1/4,−1/4, 1/4)
(1 ,−1,3)	(1 ,−1,3)	(−1, 1 ,−3)	(0 , 0 , 0)	(0 , 0 , 0)
(3 ,−1,1)	(3 ,−1,1)	(−1, 3 , 1)	(1/4 , 1/4 , 1/4)	(1/4 , 1/4 , 1/4)
(3 ,−1,1)	(3 ,−1,1)	(1 , 1 , 3)	(1/2 , 0 , 1/2)	(1/2 , 0 , 1/2)
(3 ,−1,1)	(3 ,−1,1)	(3 ,−1, 1)	(3/4 ,−1/4, 1/4)	(3/4 ,−1/4, 1/4)
(3 ,−1,1)	(3 ,−1,1)	(1 ,−3,−1)	(1/2 ,−1/2, 0)	(1/2 ,−1/2, 0)
(3 ,−1,1)	(3 ,−1,1)	(−1,−1,−3)	(1/4 ,−1/4,−1/4)	(1/4 ,−1/4,−1/4)
(3 ,−1,1)	(3 ,−1,1)	(−3, 1 ,−1)	(0 , 0 , 0)	(0 , 0 , 0)

Table F.3: Transitions 37-54 out of 72 two-step transitions originating from $(0,0,0)$. b is the Si lattice parameter.

$\vec{t}_i$ $[b/8]$	I_{hex} $[b/8]$	$\vec{t}_j$ $[b/8]$	I_{split} $[b]$	$\Delta\vec{x}_{ij}$ $[b]$
(−1,−3,−1)	(−1,−3,−1)	(−1, 1 , 3)	(−1/4,−1/4, 1/4)	(−1/4,−1/4, 1/4)
(−1,−3,−1)	(−1,−3,−1)	(−3,−1, 1)	(−1/2,−1/2, 0)	(−1/2,−1/2, 0)
(−1,−3,−1)	(−1,−3,−1)	(−1,−3,−1)	(−1/4,−3/4,−1/4)	(−1/4,−3/4,−1/4)
(−1,−3,−1)	(−1,−3,−1)	(1 ,−1,−3)	(0 ,−1/2,−1/2)	(0 ,−1/2,−1/2)
(−1,−3,−1)	(−1,−3,−1)	(3 , 1 ,−1)	(1/4 ,−1/4,−1/4)	(1/4 ,−1/4,−1/4)
(−1,−3,−1)	(−1,−3,−1)	(1 , 3 , 1)	(0 , 0 , 0)	(0 , 0 , 0)
(−3,−1,−1)	(−3,−1,−1)	(1 ,−1, 3)	(−1/4,−1/4, 1/4)	(−1/4,−1/4, 1/4)
(−3,−1,−1)	(−3,−1,−1)	(−1,−3, 1)	(−1/2,−1/2, 0)	(−1/2,−1/2, 0)
(−3,−1,−1)	(−3,−1,−1)	(−3,−1,−1)	(−3/4,−1/4,−1/4)	(−3/4,−1/4,−1/4)
(−3,−1,−1)	(−3,−1,−1)	(−1, 1 ,−3)	(−1/2, 0 ,−1/2)	(−1/2, 0 ,−1/2)
(−3,−1,−1)	(−3,−1,−1)	(1 , 3 ,−1)	(−1/4, 1/4 ,−1/4)	(−1/4, 1/4 ,−1/4)
(−3,−1,−1)	(−3,−1,−1)	(3 , 1 , 1)	(0 , 0 , 0)	(0 , 0 , 0)
(−3, 1 , 1)	(−3, 1 , 1)	(1 ,−3, 1)	(−1/4,−1/4, 1/4)	(−1/4,−1/4, 1/4)
(−3, 1 , 1)	(−3, 1 , 1)	(−1,−1, 3)	(−1/2, 0 , 1/2)	(−1/2, 0 , 1/2)
(−3, 1 , 1)	(−3, 1 , 1)	(−3, 1 , 1)	(−3/4, 1/4 , 1/4)	(−3/4, 1/4 , 1/4)
(−3, 1 , 1)	(−3, 1 , 1)	(−1, 3 ,−1)	(−1/2, 1/2 , 0)	(−1/2, 1/2 , 0)
(−3, 1 , 1)	(−3, 1 , 1)	(1 , 1 ,−3)	(−1/4, 1/4 ,−1/4)	(−1/4, 1/4 ,−1/4)
(−3, 1 , 1)	(−3, 1 , 1)	(3 ,−1,−1)	(0 , 0 , 0)	(0 , 0 , 0)

Table F.4: Transitions 55-72 out of 72 two-step transitions originating from $(0,0,0)$. b is the Si lattice parameter.

$\vec{t}_i$ $[b/8]$	I_{hex} $[b/8]$	$\vec{t}_j$ $[b/8]$	I_{split} $[b]$	$\Delta\vec{x}_{ij}$ $[b]$
(1 ,−3, 1)	(1 ,−3, 1)	(−3, 1 , 1)	(−1/4,−1/4, 1/4)	(−1/4,−1/4, 1/4)
(1 ,−3, 1)	(1 ,−3, 1)	(−1,−1, 3)	(0 ,−1/2, 1/2)	(0 ,−1/2, 1/2)
(1 ,−3, 1)	(1 ,−3, 1)	(1 ,−3, 1)	(1/4 ,−3/4, 1/4)	(1/4 ,−3/4, 1/4)
(1 ,−3, 1)	(1 ,−3, 1)	(3 ,−1,−1)	(1/2 ,−1/2, 0)	(1/2 ,−1/2, 0)
(1 ,−3, 1)	(1 ,−3, 1)	(1 , 1 ,−3)	(1/4 ,−1/4,−1/4)	(1/4 ,−1/4,−1/4)
(1 ,−3, 1)	(1 ,−3, 1)	(−1, 3 ,−1)	(0 , 0 , 0)	(0 , 0 , 0)
(−1,−1,−3)	(−1,−1,−3)	(3 ,−1, 1)	(1/4 ,−1/4,−1/4)	(1/4 ,−1/4,−1/4)
(−1,−1,−3)	(−1,−1,−3)	(1 ,−3,−1)	(0 ,−1/2,−1/2)	(0 ,−1/2,−1/2)
(−1,−1,−3)	(−1,−1,−3)	(−1,−1,−3)	(−1/4,−1/4,−3/4)	(−1/4,−1/4,−3/4)
(−1,−1,−3)	(−1,−1,−3)	(−3, 1 ,−1)	(−1/2, 0 ,−1/2)	(−1/2, 0 ,−1/2)
(−1,−1,−3)	(−1,−1,−3)	(−1, 3 , 1)	(−1/4, 1/4 ,−1/4)	(−1/4, 1/4 ,−1/4)
(−1,−1,−3)	(−1,−1,−3)	(1 , 1 , 3)	(0 , 0 , 0)	(0 , 0 , 0)
(1 , 1 ,−3)	(1 , 1 ,−3)	(1 ,−3, 1)	(1/4 ,−1/4,−1/4)	(1/4 ,−1/4,−1/4)
(1 , 1 ,−3)	(1 , 1 ,−3)	(3 ,−1,−1)	(1/2 , 0 ,−1/2)	(1/2 , 0 ,−1/2)
(1 , 1 ,−3)	(1 , 1 ,−3)	(1 , 1 ,−3)	(1/4 , 1/4 ,−3/4)	(1/4 , 1/4 ,−3/4)
(1 , 1 ,−3)	(1 , 1 ,−3)	(−1, 3 ,−1)	(0 , 1/2 ,−1/2)	(0 , 1/2 ,−1/2)
(1 , 1 ,−3)	(1 , 1 ,−3)	(−3, 1 , 1)	(−1/4, 1/4 ,−1/4)	(−1/4, 1/4 ,−1/4)
(1 , 1 ,−3)	(1 , 1 ,−3)	(−1,−1, 3)	(0 , 0 , 0)	(0 , 0 , 0)

Table F.5: Transitions 1-18 out of 72 two-step transitions originating from $(1/4, 1/4, 1/4)$. b is the Si lattice parameter.

$\vec{t}_i$ $[b/8]$	I_{hex} $[b/8]$	$\vec{t}_j$ $[b/8]$	I_{split} $[b]$	$\Delta\vec{x}_{ij}$ $[b]$
(−3,−1, 1)	(−1, 1 , 3)	(1 ,−1,−3)	(0 , 0 , 0)	(−1/4,−1/4,−1/4)
(−3,−1, 1)	(−1, 1 , 3)	(−1,−3,−1)	(−1/4,−1/4, 1/4)	(−1/2,−1/2, 0)
(−3,−1, 1)	(−1, 1 , 3)	(−3,−1, 1)	(−1/2, 0 , 1/2)	(−3/4,−1/4, 1/4)
(−3,−1, 1)	(−1, 1 , 3)	(−1, 1 , 3)	(−1/4, 1/4 , 3/4)	(−1/2, 0 , 1/2)
(−3,−1, 1)	(−1, 1 , 3)	(1 , 3 , 1)	(0 , 1/2 , 1/2)	(−1/4, 1/4 , 1/4)
(−3,−1, 1)	(−1, 1 , 3)	(3 , 1 ,−1)	(1/4 , 1/4 , 1/4)	(0 , 0 , 0)
(−1,−3, 1)	(1 ,−1, 3)	(−1, 1 ,−3)	(0 , 0 , 0)	(−1/4,−1/4,−1/4)
(−1,−3, 1)	(1 ,−1, 3)	(−3,−1,−1)	(−1/4,−1/4, 1/4)	(−1/2,−1/2, 0)
(−1,−3, 1)	(1 ,−1, 3)	(−1,−3, 1)	(0 ,−1/2, 1/2)	(−1/4,−3/4, 1/4)
(−1,−3, 1)	(1 ,−1, 3)	(1 ,−1, 3)	(1/4 ,−1/4, 3/4)	(0 ,−1/2, 1/2)
(−1,−3, 1)	(1 ,−1, 3)	(3 , 1 , 1)	(1/2 , 0 , 1/2)	(1/4 ,−1/4, 1/4)
(−1,−3, 1)	(1 ,−1, 3)	(1 , 3 ,−1)	(1/4 , 1/4 , 1/4)	(0 , 0 , 0)
(1 ,−1,−3)	(3 , 1 ,−1)	(−3,−1, 1)	(0 , 0 , 0)	(−1/4,−1/4,−1/4)
(1 ,−1,−3)	(3 , 1 ,−1)	(−1,−3,−1)	(1/4 ,−1/4,−1/4)	(0 ,−1/2,−1/2)
(1 ,−1,−3)	(3 , 1 ,−1)	(1 ,−1,−3)	(1/2 , 0 ,−1/2)	(1/4 ,−1/4,−3/4)
(1 ,−1,−3)	(3 , 1 ,−1)	(3 , 1 ,−1)	(3/4 , 1/4 ,−1/4)	(1/2 , 0 ,−1/2)
(1 ,−1,−3)	(3 , 1 ,−1)	(1 , 3 , 1)	(1/2 , 1/2 , 0)	(1/4 , 1/4 ,−1/4)
(1 ,−1,−3)	(3 , 1 ,−1)	(−1, 1 , 3)	(1/4 , 1/4 , 1/4)	(0 , 0 , 0)

Table F.6: Transitions 19-36 out of 72 two-step transitions originating from $(1/4, 1/4, 1/4)$. b is the Si lattice parameter.

$\vec{t}_i$ $[b/8]$	I_{hex} $[b/8]$	$\vec{t}_j$ $[b/8]$	I_{split} $[b]$	$\Delta\vec{x}_{ij}$ $[b]$
(1 ,−3,−1)	(3 ,−1, 1)	(−3, 1 ,−1)	(0 , 0 , 0)	(−1/4,−1/4,−1/4)
(1 ,−3,−1)	(3 ,−1, 1)	(−1,−1,−3)	(1/4 ,−1/4,−1/4)	(0 ,−1/2,−1/2)
(1 ,−3,−1)	(3 ,−1, 1)	(1 ,−3,−1)	(1/2 ,−1/2, 0)	(1/4 ,−3/4,−1/4)
(1 ,−3,−1)	(3 ,−1, 1)	(3 ,−1, 1)	(3/4 ,−1/4, 1/4)	(1/2 ,−1/2, 0)
(1 ,−3,−1)	(3 ,−1, 1)	(1 , 1 , 3)	(1/2 , 0 , 1/2)	(1/4 ,−1/4, 1/4)
(1 ,−3,−1)	(3 ,−1, 1)	(−1, 3 , 1)	(1/4 , 1/4 , 1/4)	(0 , 0 , 0)
(−1, 1 ,−3)	(1 , 3 ,−1)	(−1,−3, 1)	(0 , 0 , 0)	(−1/4,−1/4,−1/4)
(−1, 1 ,−3)	(1 , 3 ,−1)	(−3,−1,−1)	(−1/4, 1/4 ,−1/4)	(−1/2, 0 ,−1/2)
(−1, 1 ,−3)	(1 , 3 ,−1)	(−1, 1 ,−3)	(0 , 1/2 ,−1/2)	(−1/4, 1/4 ,−3/4)
(−1, 1 ,−3)	(1 , 3 ,−1)	(1 , 3 ,−1)	(1/4 , 3/4 ,−1/4)	(0 , 1/2 ,−1/2)
(−1, 1 ,−3)	(1 , 3 ,−1)	(3 , 1 , 1)	(1/2 , 1/2 , 0)	(1/4 , 1/4 ,−1/4)
(−1, 1 ,−3)	(1 , 3 ,−1)	(1 ,−1, 3)	(1/4 , 1/4 , 1/4)	(0 , 0 , 0)
(−3, 1 ,−1)	(−1, 3 , 1)	(1 ,−3,−1)	(0 , 0 , 0)	(−1/4,−1/4,−1/4)
(−3, 1 ,−1)	(−1, 3 , 1)	(−1,−1,−3)	(−1/4, 1/4 ,−1/4)	(−1/2, 0 ,−1/2)
(−3, 1 ,−1)	(−1, 3 , 1)	(−3, 1 ,−1)	(−1/2, 1/2 , 0)	(−3/4, 1/4 ,−1/4)
(−3, 1 ,−1)	(−1, 3 , 1)	(−1, 3 , 1)	(−1/4, 3/4 , 1/4)	(−1/2, 1/2 , 0)
(−3, 1 ,−1)	(−1, 3 , 1)	(1 , 1 , 3)	(0 , 1/2 , 1/2)	(−1/4, 1/4 , 1/4)
(−3, 1 ,−1)	(−1, 3 , 1)	(3 ,−1, 1)	(1/4 , 1/4 , 1/4)	(0 , 0 , 0)

Table F.7: Transitions 37-54 out of 72 two-step transitions originating from $(1/4, 1/4, 1/4)$. b is the Si lattice parameter.

$\vec{t}_i$ $[b/8]$	I_{hex} $[b/8]$	$\vec{t}_j$ $[b/8]$	I_{split} $[b]$	$\Delta\vec{x}_{ij}$ $[b]$
(1, 3 , 1)	(3,5,3)	(1 ,−1,−3)	(1/2, 1/2 , 0)	(1/4 , 1/4 ,−1/4)
(1, 3 , 1)	(3,5,3)	(3 , 1 ,−1)	(3/4, 3/4 , 1/4)	(1/2 , 1/2 , 0)
(1, 3 , 1)	(3,5,3)	(1 , 3 , 1)	(1/2, 2/2 , 1/2)	(1/4 , 3/4 , 1/4)
(1, 3 , 1)	(3,5,3)	(−1, 1 , 3)	(1/4, 3/4 , 3/4)	(0 , 1/2 , 1/2)
(1, 3 , 1)	(3,5,3)	(−3,−1, 1)	(0 , 1/2 , 1/2)	(−1/4, 1/4 , 1/4)
(1, 3 , 1)	(3,5,3)	(−1,−3,−1)	(1/4, 1/4 , 1/4)	(0 , 0 , 0)
(3, 1 , 1)	(5,3,3)	(−1, 1 ,−3)	(1/2, 1/2 , 0)	(1/4 , 1/4 ,−1/4)
(3, 1 , 1)	(5,3,3)	(1 , 3 ,−1)	(3/4, 3/4 , 1/4)	(1/2 , 1/2 , 0)
(3, 1 , 1)	(5,3,3)	(3 , 1 , 1)	(2/2, 1/2 , 1/2)	(3/4 , 1/4 , 1/4)
(3, 1 , 1)	(5,3,3)	(1 ,−1, 3)	(3/4, 1/4 , 3/4)	(1/2 , 0 , 1/2)
(3, 1 , 1)	(5,3,3)	(−1,−3, 1)	(1/2, 0 , 1/2)	(1/4 ,−1/4, 1/4)
(3, 1 , 1)	(5,3,3)	(−3,−1,−1)	(1/4, 1/4 , 1/4)	(0 , 0 , 0)
(3,−1,−1)	(5,1,1)	(−1, 3 ,−1)	(1/2, 1/2 , 0)	(1/4 , 1/4 ,−1/4)
(3,−1,−1)	(5,1,1)	(1 , 1 ,−3)	(3/4, 1/4 ,−1/4)	(1/2 , 0 ,−1/2)
(3,−1,−1)	(5,1,1)	(3 ,−1,−1)	(2/2, 0 , 0)	(3/4 ,−1/4,−1/4)
(3,−1,−1)	(5,1,1)	(1 ,−3, 1)	(3/4,−1/4, 1/4)	(1/2 ,−1/2, 0)
(3,−1,−1)	(5,1,1)	(−1,−1, 3)	(1/2, 0 , 1/2)	(1/4 ,−1/4, 1/4)
(3,−1,−1)	(5,1,1)	(−3, 1 , 1)	(1/4, 1/4 , 1/4)	(0 , 0 , 0)

Table F.8: Transitions 55-72 out of 72 two-step transitions originating from $(1/4, 1/4, 1/4)$. b is the Si lattice parameter.

$\vec{t}_i$ $[b/8]$	I_{hex} $[b/8]$	$\vec{t}_j$ $[b/8]$	I_{split} $[b]$	$\Delta\vec{x}_{ij}$ $[b]$
(−1, 3 ,−1)	(1,5,1)	(3 ,−1,−1)	(1/2 , 1/2 , 0)	(1/4 , 1/4 ,−1/4)
(−1, 3 ,−1)	(1,5,1)	(1 , 1 ,−3)	(1/4 , 3/4 ,−1/4)	(0 , 1/2 ,−1/2)
(−1, 3 ,−1)	(1,5,1)	(−1, 3 ,−1)	(0 , 2/2 , 0)	(−1/4, 3/4 ,−1/4)
(−1, 3 ,−1)	(1,5,1)	(−3, 1 , 1)	(−1/4, 3/4 , 1/4)	(−1/2, 1/2 , 0)
(−1, 3 ,−1)	(1,5,1)	(−1,−1, 3)	(0 , 1/2 , 1/2)	(−1/4, 1/4 , 1/4)
(−1, 3 ,−1)	(1,5,1)	(1 ,−3, 1)	(1/4 , 1/4 , 1/4)	(0 , 0 , 0)
(1 , 1 , 3)	(3,3,5)	(−3, 1 ,−1)	(0 , 1/2 , 1/2)	(−1/4, 1/4 , 1/4)
(1 , 1 , 3)	(3,3,5)	(−1, 3 , 1)	(1/4 , 3/4 , 3/4)	(0 , 1/2 , 1/2)
(1 , 1 , 3)	(3,3,5)	(1 , 1 , 3)	(1/2 , 1/2 , 2/2)	(1/4 , 1/4 , 3/4)
(1 , 1 , 3)	(3,3,5)	(3 ,−1, 1)	(3/4 , 1/4 , 3/4)	(1/2 , 0 , 1/2)
(1 , 1 , 3)	(3,3,5)	(1 ,−3,−1)	(1/2 , 0 , 1/2)	(1/4 ,−1/4, 1/4)
(1 , 1 , 3)	(3,3,5)	(−1,−1,−3)	(1/4 , 1/4 , 1/4)	(0 , 0 , 0)
(−1,−1, 3)	(1,1,5)	(−1, 3 ,−1)	(0 , 1/2 , 1/2)	(−1/4, 1/4 , 1/4)
(−1,−1, 3)	(1,1,5)	(−3, 1 , 1)	(−1/4, 1/4 , 3/4)	(−1/2, 0 , 1/2)
(−1,−1, 3)	(1,1,5)	(−1,−1, 3)	(0 , 0 , 2/2)	(−1/4,−1/4, 3/4)
(−1,−1, 3)	(1,1,5)	(1 ,−3, 1)	(1/4 ,−1/4, 3/4)	(0 ,−1/2, 1/2)
(−1,−1, 3)	(1,1,5)	(3 ,−1,−1)	(1/2 , 0 , 1/2)	(1/4 ,−1/4, 1/4)
(−1,−1, 3)	(1,1,5)	(1 , 1 ,−3)	(1/4 , 1/4 , 1/4)	(0 , 0 , 0)

F.2 Transition vectors of KLMC lattice

Figure F.2 shows schematically the two-step process used to describe the KLMC lattice in Chapter 6. The arrows in the graph correspond to transition vectors between different I_{split} and I_{hex} states. Table F.9 lists the location (fcc sub-lattice) and orientation of the individual I_{split} configurations as well as the transition vectors indicated schematically in Fig. F.2. Each arrow in the graph corresponds to two different transition vectors, which lead to the same unique type of hexagonal state (H1-H4). All coordinates are reported in units of the Si lattice parameter $b = 5.43$ Å.

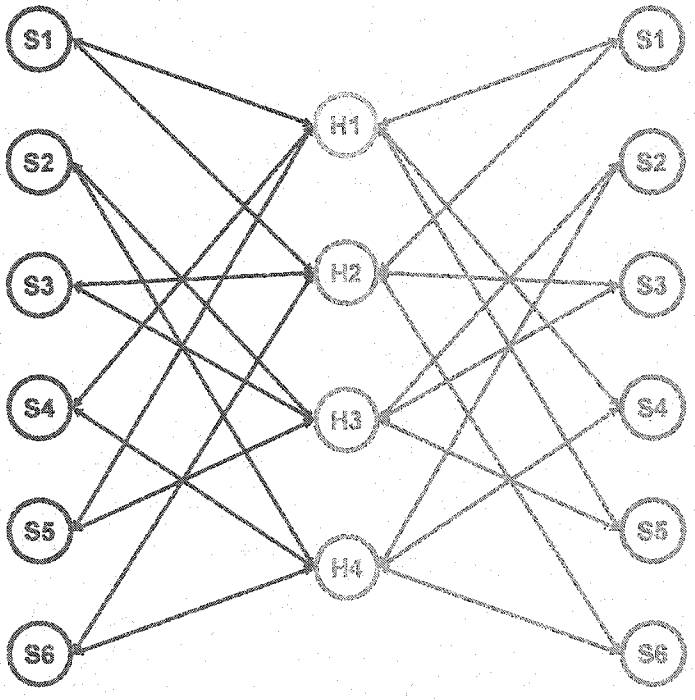

Figure F.2: KLMC lattice for interstitial diffusion $I_{split} \rightarrow I_{hex} \rightarrow I_{split}$. S1-S6 (red symbols) are the 6 I_{split} configuration on the sub-lattice with origin at $(0, 0, 0)$, S1-S6 (green symbols) are the 6 I_{split} configuration on the sub-lattice with origin at $(1/4, 1/4, 1/4)$, and H1-H4 are the 4 unique hexagonal interstitial sites connecting the various I_{split} configurations. The arrows indicate the transition vectors of the possible transitions. Table F.9 lists the individual transition vectors of the KLMC lattice.

Table F.9: Transition vectors of KLMC lattice shown in Fig. F.2. The first column in both tables lists the different I_{split} configurations including their orientations. Left: S1-S6 are located at $(0,0,0)$ (red symbols). Right: S1-S6 are located at $(1/4,1/4,1/4)$ (green symbols). $\vec{t}$ is a transition vector, which connects a I_{split} site with a I_{hex} site.

I_{split}	$\vec{t}\,[b/8]$	I_{hex}
S1: [1 1 0]	(3 , 1 ,−1)	H1
S1: [1 1 0]	(1 , 3 ,−1)	H2
S1: [1 1 0]	(−1,−3,−1)	H1
S1: [1 1 0]	(−3,−1,−1)	H2
S2: [1 $\bar{1}$ 0]	(−1, 3 , 1)	H3
S2: [1 $\bar{1}$ 0]	(3 ,−1, 1)	H3
S2: [1 $\bar{1}$ 0]	(−3, 1 , 1)	H4
S2: [1 $\bar{1}$ 0]	(1 ,−3,−1)	H4
S3: [1 0 1]	(1 ,−1, 3)	H2
S3: [1 0 1]	(3 ,−1, 1)	H3
S3: [1 0 1]	(−3,−1,−1)	H2
S3: [1 0 1]	(−1,−1,−3)	H3
S4: [1 0 $\bar{1}$]	(3 , 1 ,−1)	H1
S4: [1 0 $\bar{1}$]	(−1, 1 , 3)	H1
S4: [1 0 $\bar{1}$]	(−3, 1 , 1)	H4
S4: [1 0 $\bar{1}$]	(1 , 1 ,−3)	H4
S5: [0 1 1]	(−1, 1 , 3)	H1
S5: [0 1 1]	(−1, 3 , 1)	H3
S5: [0 1 1]	(−1,−3,−1)	H1
S5: [0 1 1]	(−1,−1,−3)	H3
S6: [0 1 $\bar{1}$]	(1 , 3 ,−1)	H2
S6: [0 1 $\bar{1}$]	(1 ,−1, 3)	H2
S6: [0 1 $\bar{1}$]	(1 ,−3, 1)	H4
S6: [0 1 $\bar{1}$]	(1 , 1 ,−3)	H4

I_{split}	$\vec{t}\,[b/8]$	I_{hex}
S1: [1 1 0]	(−3,−1, 1)	H1
S1: [1 1 0]	(−1,−3, 1)	H2
S1: [1 1 0]	(1 , 3 , 1)	H1
S1: [1 1 0]	(3 , 1 , 1)	H2
S2: [1 $\bar{1}$ 0]	(1 ,−3,−1)	H3
S2: [1 $\bar{1}$ 0]	(−3, 1 ,−1)	H3
S2: [1 $\bar{1}$ 0]	(3 ,−1,−1)	H4
S2: [1 $\bar{1}$ 0]	(−1, 3 , 1)	H4
S3: [1 0 1]	(−1, 1 ,−3)	H2
S3: [1 0 1]	(−3, 1 ,−1)	H3
S3: [1 0 1]	(3 , 1 , 1)	H2
S3: [1 0 1]	(1 , 1 , 3)	H3
S4: [1 0 $\bar{1}$]	(−3,−1, 1)	H1
S4: [1 0 $\bar{1}$]	(1 ,−1,−3)	H1
S4: [1 0 $\bar{1}$]	(3 ,−1,−1)	H4
S4: [1 0 $\bar{1}$]	(−1,−1, 3)	H4
S5: [0 1 1]	(1 ,−1,−3)	H1
S5: [0 1 1]	(1 ,−3,−1)	H3
S5: [0 1 1]	(1 , 3 , 1)	H1
S5: [0 1 1]	(1 , 1 , 3)	H3
S6: [0 1 $\bar{1}$]	(−1,−3, 1)	H2
S6: [0 1 $\bar{1}$]	(−1, 1 ,−3)	H2
S6: [0 1 $\bar{1}$]	(−1, 3 ,−1)	H4
S6: [0 1 $\bar{1}$]	(−1,−1, 3)	H4

Appendix G

TECHNICAL DETAILS AND CONVERGENCE OF ELASTICITY CALCULATIONS

The following sections summarize the technical details of the elasticity calculations reported in Chapters 5, 6, and 7 and discuss the convergence errors of the extracted elastic constants and induced strains for the different dopant and point-defect configurations. Sections G.1, G.2, and G.3 address the convergence errors of the elasticity parameters of pure Si, vacancy, and interstitials respectively (see Chapter 5). In Section G.4, the convergence of the vacancy and interstitial transition state calculations are discussed (see Chapter 6), whereas Section G.5 summarizes the convergence analysis for B systems (see Chapters 6 and 7).

For all calculations, we used the density functional theory (DFT) code VASP [9, 61, 62] with ultrasoft Vanderbilt type pseudo-potentials [63, 64]. All calculations were performed in generalized gradient approximation (GGA) with the exception of the Si elastic properties which were also calculated in local density approximation (LDA) for comparison. We used consistently a 64 Si atom super-cell. Convergence of the results was tested with respect to the energy cutoff and **k**-point sampling of the 1st BZ as specified in the individual sections. For all calculations, we used Monkhorst-Pack **k**-point sampling [86, 87, 88] and all structures were fully relaxed to a maximal force of less than $0.005\,\mathrm{eV/\AA}$ per atom.

In the following sections convergence of the individual parameters is reported as the percentage difference between the less accurate calculation and the most accurate calculation.

G.1 Silicon

The following two sections summarize the results of the convergence calculations for the elastic properties of Si which are reported in Table 5.1. Sections G.1.1 and G.1.2 report the results for LDA and GGA calculations respectively.

G.1.1 LDA calculation

Convergence of b_0, K, C_{11}, and C_{12} was tested with respect to energy cutoff and **k**-point sampling. Figure G.1 shows the effect of increasing the cutoff from 250 eV to 280 eV using constant 2^3 Monkhorst-Pack **k**-point sampling and a high precision FFT-grids for hydrostatic and x-strain. The extracted parameters are listed in Table G.1. All parameters are converged with an error of less than 0.5 % with respect to the energy cutoff. Similarly Fig. G.2 shows the effect of increasing the Monkhorst-Pack **k**-point sampling from 2^3 to 3^3 with a constant energy cutoff of 250 eV and high precision FFT-grids for hydrostatic and x-strain. The extracted parameters are listed in Table G.2. All parameters are converged with an error of less than 2.3 % with respect to the **k**-point sampling.

In summary, combining both results for 2^3 Monkhorst-Pack **k**-point sampling and an energy cutoff of 250 eV all LDA parameters are converged within an error of less than 2.4 %.

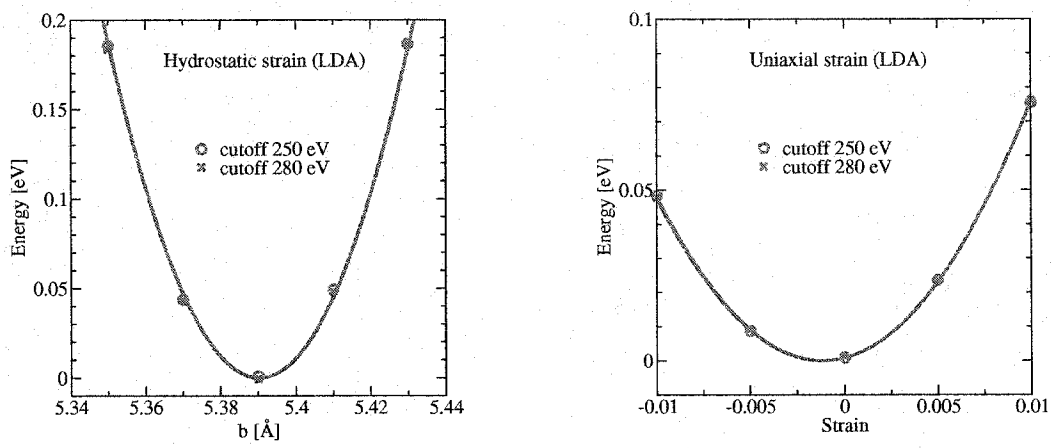

Figure G.1: Energy vs. hydrostatic (left) and uniaxial strain (right) for Si using 2^3 Monkhorst-Pack **k**-point sampling and a high precision FFT-grid (see Ref. [9]), but different cutoff energies. All energies are reported with respect to their minimum energy strain condition. The data shown corresponds to a 64 atom super-cell LDA calculation. $\epsilon = 0$ corresponds to the lattice constant $b = 5.393\,\text{Å}$. The extracted values are listed in Table G.1.

Table G.1: Energy cutoff dependence of Si parameters in LDA calculation using 2^3 Monkhorst-Pack **k**-point sampling. The parameters are extracted from Fig. G.1.

Energy cutoff	b_0 [Å]	K [GPa]	C_{11} [GPa]	C_{12} [GPa]
250 eV	5.3903	95.8	157.5	64.9
280 eV	5.3901	95.7	156.8	65.2

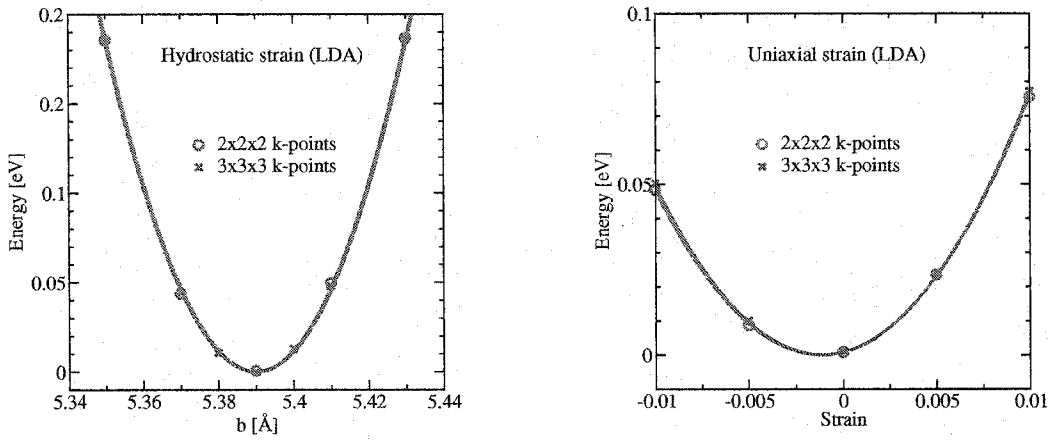

Figure G.2: Energy vs. hydrostatic (left) and uniaxial strain (right) for Si using a 250 eV energy cutoff and a high precision FFT-grid (see Ref. [9]), but different Monkhorst-Pack **k**-point sampling. All energies are reported with respect to their minimum energy strain condition. The data shown corresponds to a 64 atom supercell LDA calculation. $\epsilon = 0$ corresponds to the lattice constant $b = 5.393$ Å. The extracted values are listed in Table G.2.

Table G.2: **k**-point sampling dependence of Si parameters in LDA calculation using an energy cutoff of 250 eV. The parameters are extracted from Fig. G.2.

k-point mesh	b_0 [Å]	K [GPa]	C_{11} [GPa]	C_{12} [GPa]
2^3	5.3903	95.8	157.5	64.9
3^3	5.3898	95.7	160.2	63.4

G.1.2 GGA calculation

Convergence of b_0, K, C_{11}, and C_{12} was tested with respect to energy cutoff and **k**-point sampling. Figure G.3 shows the effect of increasing the cutoff from 250 eV to 280 eV using constant 2^3 Monkhorst-Pack **k**-point sampling and a high precision FFT-grids for hydrostatic and x-strain. The extracted parameters are listed in Table G.3. All parameters are converged with an error of less than 2.2 % with respect to the energy cutoff. Similarly Fig. G.4 shows the effect of increasing the Monkhorst-Pack **k**-point sampling from 2^3 to 3^3 with a constant energy cutoff of 250 eV and high precision FFT-grids for hydrostatic and x-strain. The extracted parameters are listed in Table G.4. All parameters are converged with an error of less than 3.8 % with respect to the **k**-point sampling.

In summary, combining both results for 2^3 Monkhorst-Pack **k**-point sampling and an energy cutoff of 250 eV all GGA parameters are converged within an error of less than 4.4 %.

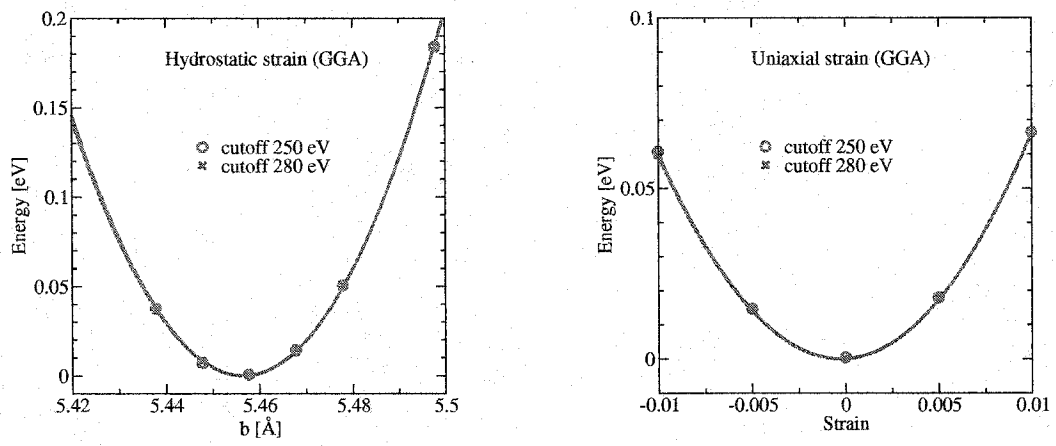

Figure G.3: Energy vs. hydrostatic (left) and uniaxial strain (right) for Si using 2^3 Monkhorst-Pack **k**-point sampling and a high precision FFT-grid (see Ref. [9]), but different cutoff energies. All energies are reported with respect to their minimum energy strain condition. The data shown corresponds to a 64 atom super-cell GGA calculation. $\epsilon = 0$ corresponds to the Si GGA lattice constant $b = 5.457\,\text{Å}$. The extracted values are listed in Table G.3.

Table G.3: Energy cutoff dependence of Si parameters in GGA calculation using 2^3 Monkhorst-Pack **k**-point sampling. The parameters are extracted from Fig. G.3.

Energy cutoff	b_0 [Å]	K [GPa]	C_{11} [GPa]	C_{12} [GPa]
250 eV	5.4566	88.7	156.3	54.9
280 eV	5.4567	89.1	159.8	53.7

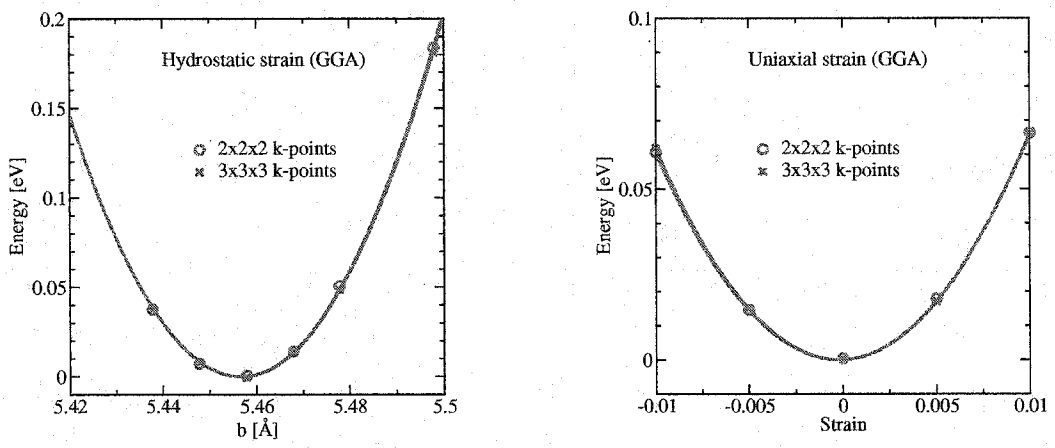

Figure G.4: Energy vs. hydrostatic (left) and uniaxial strain (right) for Si using a 250 eV energy cutoff and a high precision FFT-grid (see Ref. [9]), but different Monkhorst-Pack **k**-point sampling. All energies are reported with respect to their minimum energy strain condition. The data shown corresponds to a 64 atom supercell GGA calculation. $\epsilon = 0$ corresponds to the Si GGA lattice constant $b = 5.457$ Å. The extracted values are listed in Table G.4.

Table G.4: **k**-point sampling dependence of Si parameters in GGA calculation using an energy cutoff of 250 eV. The parameters are extracted from Fig. G.4.

k-point mesh	b_0 [Å]	K [GPa]	C_{11} [GPa]	C_{12} [GPa]
2^3	5.4566	88.7	156.3	54.9
3^3	5.4567	88.1	158.7	52.8

G.2 Vacancy

The convergence of the vacancy elastic constants and induced strain were tested with respect to energy cutoff and **k**-point sampling for hydrostatic as well as uniaxial strain in the x-direction. Increasing the cutoff from 250 eV to 280 eV (Figure G.5) as well as changing the **k**-point sampling from 3^3 to 4^3 (Figure G.6) proofed convergence. The parameters in the Tables G.5 and G.6 are extracted from the Figs. G.5 and G.6 by fitting a complete set of data (hydrostatic and x-strain) to Eq. 5.6. C_{ij} is defined as $C_{ij} = C_{ij}^{\mathrm{Si}} + x\Delta C_{ij}$, where $x = 1/64$. K and C_{ij} are the actual curvatures at the concentration x, whereas $\Delta\epsilon$ is reported in the usual concentration independent way. The induced strain $\Delta\epsilon$ is converged within 3.6 % for 3^3 Monkhorst-Pack **k**-point sampling and an energy cutoff of 250 eV.

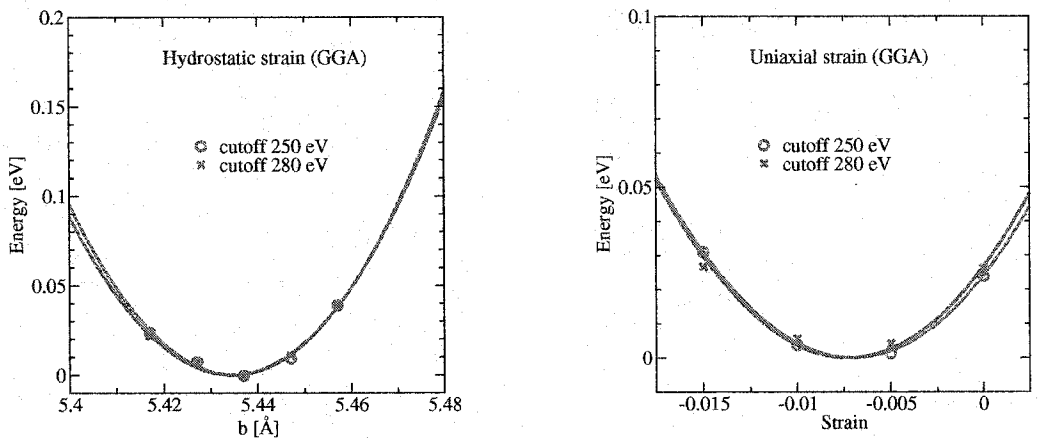

Figure G.5: Energy vs. hydrostatic (left) and uniaxial strain (right) for V using 2^3 Monkhorst-Pack **k**-point sampling and a high precision FFT-grid (see Ref. [9]), but different cutoff energies. All energies are reported with respect to their minimum energy strain condition. The data shown corresponds to a 64 atom super-cell GGA calculation. $\epsilon = 0$ corresponds to the Si GGA lattice constant $b = 5.457\,\text{Å}$. The extracted values are listed in Table G.5.

Table G.5: Energy cutoff dependence of V parameters in GGA calculation using 2^3 Monkhorst-Pack **k**-point sampling. The parameters are extracted from Fig. G.5.

Energy cutoff	K [GPa]	C_{11} [GPa]	C_{12} [GPa]	$\Delta\epsilon$
250 eV	66.6	115.9	42.0	−0.2578
280 eV	67.1	115.0	43.1	−0.2615

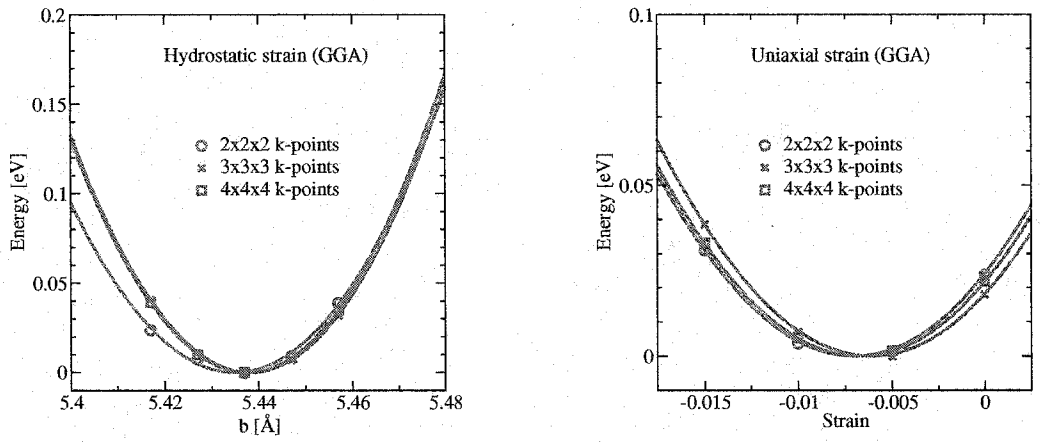

Figure G.6: Energy vs. hydrostatic (left) and uniaxial strain (right) for V using a 250 eV energy cutoff and a high precision FFT-grid (see Ref. [9]), but different Monkhorst-Pack **k**-point sampling. All energies are reported with respect to their minimum energy strain condition. The data shown corresponds to a 64 atom supercell GGA calculation. $\epsilon = 0$ corresponds to the Si GGA lattice constant $b = 5.457$ Å. The extracted values are listed in Table G.6.

Table G.6: **k**-point sampling dependence of V parameters in GGA calculation using an energy cutoff of 250 eV. The parameters are extracted from Fig. G.6.

k-point mesh	K [GPa]	C_{11} [GPa]	C_{12} [GPa]	$\Delta\epsilon$
2^3	66.6	115.9	42.0	−0.2578
3^3	72.6	121.6	48.1	−0.2207
4^3	74.1	117.9	52.2	−0.2280

G.3 Interstitials

The convergence of the interstitial elastic constants and induced strains were tested for I_{split} with respect to energy cutoff and **k**-point sampling. Cutoff convergence is shown in Fig. G.7. Increasing the cutoff from 250 eV to 280 eV with fixed 2^3 **k**-point sampling and a high precision FFT-grid (see Ref. [9], showed good convergence for uniaxial strain. The extracted parameters are listed in Table G.7. Changing the **k**-point sampling from 2^3 to 3^3 (see Figure G.8) also lead to well converged results. Table G.8 lists the extracted parameters. K, C_{ij}, and ϵ_{min} are the parameters for a 64 atom super-cell ($x = 1/64$). ϵ_{min} is the strain of the minimum energy configuration under x-strain.

The parameters of the different interstitial configurations (I_{split}, I_{tet}, and I_{hex}) listed in Table 5.3 of Chapter 5 are based on calculations with a cutoff energy of 280 eV, 2^3 Monkhorst-Pack **k**-point sampling and high precision FFT-grids (see Ref. [9]).

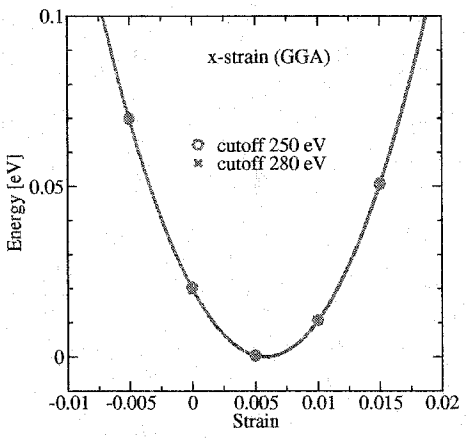

Figure G.7: Energy vs. x-strain for I_{split} using 2^3 Monkhorst-Pack **k**-point sampling and a high precision FFT-grid (see Ref. [9]), but different cutoff energies. All energies are reported with respect to their minimum energy strain condition. The data shown corresponds to a 64 atom super-cell GGA calculation. $\epsilon = 0$ corresponds to the Si GGA lattice constant $b = 5.457\,\text{Å}$. The extracted values are listed in Table G.7.

Table G.7: Energy cutoff dependence of I_{split} parameters in GGA calculation using 2^3 Monkhorst-Pack **k**-point sampling. The parameters are extracted from Fig. G.7.

Energy cutoff	C_{11} [GPa]	ϵ_{min} [%]
250 eV	146.7	0.581
280 eV	147.3	0.579

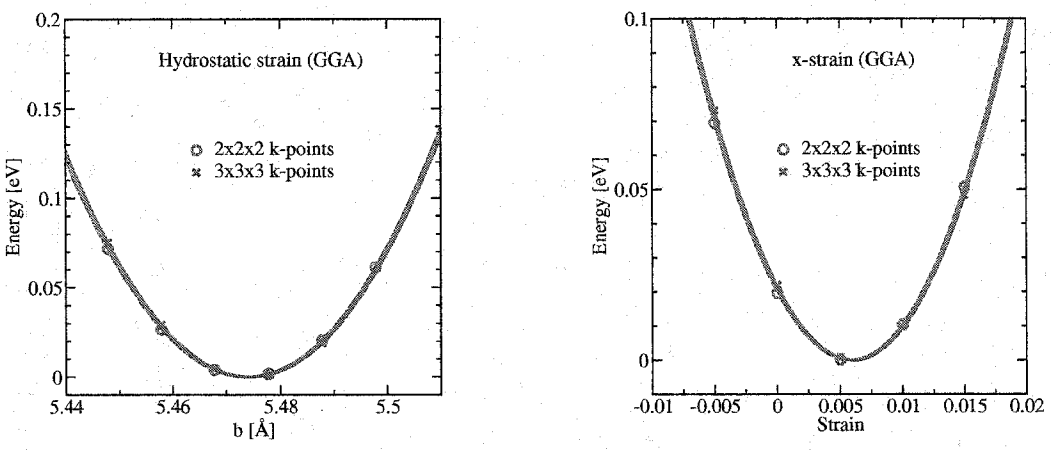

Figure G.8: Energy vs. hydrostatic (left) and x-strain (right) for I_{split} using a 280 eV energy cutoff and a high precision FFT-grid (see Ref. [9]), but different Monkhorst-Pack **k**-point sampling. All energies are reported with respect to their minimum energy strain condition. The data shown corresponds to a 64 atom super-cell GGA calculation. $\epsilon = 0$ corresponds to the Si GGA lattice constant $b = 5.457$ Å. The extracted values are listed in Table G.8.

Table G.8: **k**-point sampling dependence of I_{split} parameters in GGA calculation using an energy cutoff of 280 eV. The parameters are extracted from Fig. G.8.

k-point mesh	b_0 [Å]	K [GPa]	ϵ_{min} [%]	C_{11} [GPa]
2^3	5.4738	86.6	0.579	147.3
3^3	5.4744	86.9	0.603	147.5

G.4 Interstitial and vacancy transition state

The convergence of the vacancy transition state (V_{trans}) elastic constants and induced strains were tested with respect to energy cutoff and **k**-point sampling. The elastic properties of the vacancy transition state are well converged by using an energy cutoff of 250 eV, 2^3 Monkhorst-Pack **k**-point sampling and high precision FFT-grids. The rather large cutoff is necessary to reach convergence for stress calculations. Increasing the **k**-point sampling to 3^3 leads to a 2 % change in $\Delta\epsilon$. Figure G.9 shows a comparison between the results of the 2^3 and 3^3 Monkhorst-Pack **k**-point sampling. The extracted parameters can be found in Table G.9. K and b_0 are the V_{trans} bulk modulus and equilibrium lattice constant in a 64 Si atom super-cell ($x = 1/64$).

The elastic constants and induced strains of the interstitial transition state were determined with the same parameters (250 eV, 2^3 Monkhorst-Pack **k**-point sampling, high precision FFT-grids).

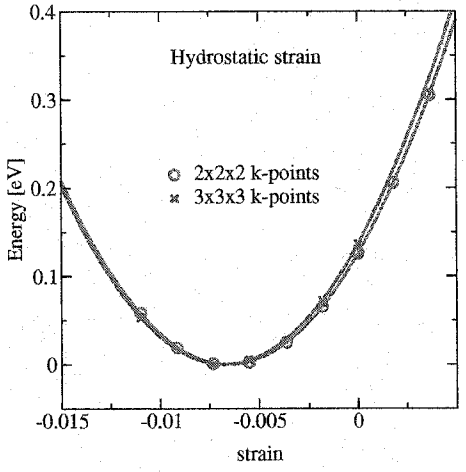

Figure G.9: Energy vs. hydrostatic strain for V_{trans} using a 250 eV energy cutoff, but different Monkhorst-Pack **k**-point sampling. All energies are reported with respect to their minimum energy strain condition. The data shown corresponds to a 64 atom super-cell calculation. $\epsilon = 0$ response to the GGA Si lattice constant $b = 5.457$ Å.

Table G.9: **k**-point sampling dependence of V_{trans} parameters in GGA calculation using an energy cutoff of 250 eV. The parameters are extracted from Fig. G.9.

k-point mesh	b_0 [Å]	K [GPa]
2^3	5.4212	80.1
3^3	5.4201	81.9

G.5 Boron

The elastic properties of B systems are well converged by using an energy cutoff of 340 eV and 2^3 or 3^3 Monkhorst-Pack **k**-point sampling depending on the strain condition (hydrostatic: 2^3, uniaxial: 3^3). The rather large cutoff is necessary to reach convergence for B systems. The convergence with respected to strain was tested for the B_s system. Figures G.10 and G.11 show the effect of increasing the energy cutoff and **k**-point sampling for hydrostatic and uniaxial strain respectively. The extracted elasticity constants and induced strains are reported in Table G.10 and G.11.

The graphs in Fig. G.10 show that for both hydrostatic strain (Fig. G.10 (left)) and uniaxial strain (Fig. G.10 (right)) elasticity constants and induced strains are well converged with respect to the energy cutoff. Further increasing the cutoff to 360 eV lead to a change of the elasticity constants and induced strain of less than 0.5 % (see Table G.10). Figure G.11 shows the **k**-point sampling dependence. In contrast to the uniaxial case (Fig. G.11 (right)), increasing the **k**-point sampling to 3^3 lead to a very moderate effect for hydrostatic strain (Fig. G.11 (left)). $\Delta\epsilon$ is converged within 4 % using 2^3 **k**-point sampling and an energy cutoff of 340 eV. Further increasing the **k**-point sampling to 4^3 lead to very well converged results even for uniaxial strain. Table G.11 summarizes the extracted results. Using 3^3 **k**-point sampling and a cutoff of 340 eV C_{11} and C_{12} are converged within 2 %.

In summary, $\Delta\epsilon$ is converged within 4 % using 2^3 **k**-point sampling and an energy cutoff of 340 eV, whereas C_{11} and C_{12} are converged within 2 % using an increased 3^3 **k**-point sampling, but the same energy cutoff of 340 eV.

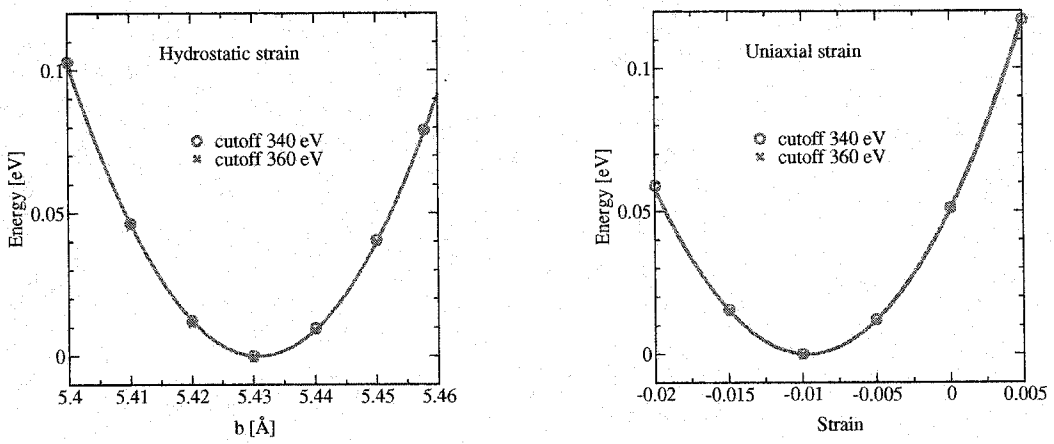

Figure G.10: Energy vs. hydrostatic (left) and uniaxial strain (right) for B_s using 2^3 Monkhorst-Pack **k**-point sampling, but different cutoff energies. All energies are reported with respect to their minimum energy strain condition. The data shown corresponds to a 64 atom super-cell calculation. $\epsilon = 0$ response to the GGA Si lattice constant $b = 5.4578\,\text{Å}$. The extracted values are listed in Table G.10.

Table G.10: Energy cutoff dependence of B_s using 2^3 Monkhorst-Pack **k**-point sampling. The parameters are extracted from Fig. G.10.

Energy cutoff	K [GPa]	C_{11} [GPa]	C_{12} [GPa]	$\Delta\epsilon$
340 eV	87.7	133.6	64.7	−0.004945
360 eV	87.7	134.1	64.5	−0.004948

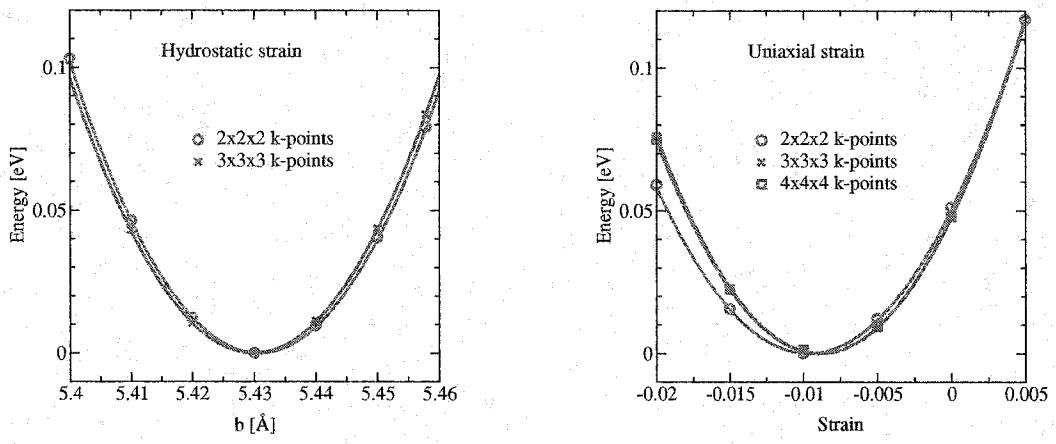

Figure G.11: Energy vs. hydrostatic (left) and uniaxial strain (right) for B_s using a 340 eV energy cutoff, but different Monkhorst-Pack **k**-point sampling. All energies are reported with respect to their minimum energy strain condition. The data shown corresponds to a 64 atom super-cell calculation. $\epsilon = 0$ response to the GGA Si lattice constant $b = 5.4578$ Å. The extracted values are listed in Table G.11.

Table G.11: **k**-point sampling dependence of B_s using an energy cutoff of 340 eV. The parameters are extracted from Fig. G.11.

k-point mesh	K [GPa]	C_{11} [GPa]	C_{12} [GPa]	$\Delta\epsilon$
2^3	87.7	133.6	64.7	−0.004945
3^3	87.6	150.9	56.0	−0.005104
4^3	87.6	148.7	57.1	−0.005104

VITA

Ph.D. Physics and Nanotechnology, University of Washington, Seattle (2004).

M.S. Physics, University of Washington, Seattle (2000).

Diploma in Physics, Justus-Liebig-Universität Giessen, Germany (1999).
Thesis: *Hadronic transition form factors in quark models.*